



## Recent advances on hydrogen production through seawater electrolysis

Item Type	Article
Authors	Mohammed-ibrahim, Jamesh; Moussab, Harb
Citation	Mohammed-Ibrahim, J., & Moussab, H. (2020). Recent advances on hydrogen production through seawater electrolysis. <i>Materials Science for Energy Technologies</i> , 3, 780–807. doi:10.1016/j.mset.2020.09.005
Eprint version	Publisher's Version/PDF
DOI	<a href="https://doi.org/10.1016/j.mset.2020.09.005">10.1016/j.mset.2020.09.005</a>
Publisher	Elsevier BV
Journal	<i>Materials Science for Energy Technologies</i>
Rights	This is an open access article under the CC BY-NC-ND license.
Download date	2024-04-24 00:40:06
Item License	<a href="http://creativecommons.org/licenses/by-nc-nd/4.0/">http://creativecommons.org/licenses/by-nc-nd/4.0/</a>
Link to Item	<a href="http://hdl.handle.net/10754/668618">http://hdl.handle.net/10754/668618</a>



## Recent advances on hydrogen production through seawater electrolysis

Jamesh Mohammed-Ibrahim<sup>a,b,\*</sup>, Harb Moussab<sup>c,\*</sup>

<sup>a</sup> Department of Physics and Materials Science, City University of Hong Kong, Tat Chee Avenue, Kowloon, Hong Kong, China

<sup>b</sup> Applied and Plasma Physics, School of Physics (A28), University of Sydney, Sydney, NSW 2006, Australia

<sup>c</sup> KAUST Catalysis Center (KCC), Physical Sciences and Engineering Division (PSE), King Abdullah University of Science and Technology (KAUST), Thuwal 23955-6900, Saudi Arabia



### ARTICLE INFO

#### Article history:

Received 24 July 2020

Revised 19 September 2020

Accepted 19 September 2020

Available online 1 October 2020

#### Keywords:

Seawater splitting

Electrocatalysis

Hydrogen production

OER selective electrocatalysts

Anticorrosion

### ABSTRACT

Electrolysis of mostly abundant seawater rather than scarce fresh water is not only a promising way to generate clean hydrogen energy, which also alleviates the use of highly demanding fresh water. At first, this review discusses about the challenging issues for seawater electrolysis including competition of chlorine evolution reaction (CIER) with oxygen evolution reaction (OER) on the anode, need for the robust and efficient electrocatalysts to sustain against chloride corrosion, and the formation of precipitates on the electrode surface. Then, the present review provides the recent advancement in terms of synthetic methodologies, chemical properties, density functional theory (DFT) calculations, and catalytic performances of several nanostructured earth-abundant/precious-metal-containing electrocatalysts for hydrogen evolution reaction (HER) and OER in seawater electrolyte, where the discussion includes highly OER selective robust electrocatalysts such as transition-metal-hexacyanomellates based electrocatalyst, transition metal nitride, and layered double hydroxide (LDH) integrated with transition metal sulfide. Finally, this review summarizes the several promising strategies to enhance the HER and OER performance of electrocatalysts in seawater (including  $\eta$  of  $\leq -200$  mV at  $-10$  mA cm<sup>-2</sup> for HER;  $\eta$  of  $\leq 300$  mV at  $\geq 100$  mA cm<sup>-2</sup> for OER; high long term stability for  $\geq 600$  h for overall water splitting).

## 1. Introduction

Producing hydrogen (H<sub>2</sub>), a clean, and ideal energy source with high energy density of 142 MJ kg<sup>-1</sup> through electrochemical water splitting using mostly abundant seawater (~96.5% of the total earth's water resources) rather than highly demanding fresh water could not only address the vital challenging issues such as increasing energy demand and the depletion of fossil fuels (such as petroleum, coal, and natural gas), but it could also alleviate the consumption of scarce fresh water around the world especially from highly demanding fresh water areas such as arid zones, several coastal countries and islands [1–3]. Moreover, electrochemical water splitting could produce H<sub>2</sub> sustainably by transforming electrical energy from intermittent-renewable resources such as solar and wind energies. Electrochemical water splitting is composed of oxygen evolution reaction (OER) at the anode and hydrogen evolution reaction (HER) at the cathode, where four electrons could be involved in OER (acid medium: 2H<sub>2</sub>O → O<sub>2</sub> + 4H<sup>+</sup> + 4e<sup>-</sup>; alkaline

medium: 4OH<sup>-</sup> → O<sub>2</sub> + 2H<sub>2</sub>O + 4e<sup>-</sup>), while two electrons could be involved in HER (acid medium: 2H<sup>+</sup> + 2e<sup>-</sup> → H<sub>2</sub>; alkaline medium: 2H<sub>2</sub>O + 2e<sup>-</sup> → H<sub>2</sub> + 2OH<sup>-</sup>) [4,5]. Currently, noble electrocatalysts [6] such as Pt for hydrogen evolution reaction (HER), and Ru/Ir-based compounds for oxygen evolution reaction (OER) are used as highly active electrocatalysts for water splitting, whereas their scarcity and high cost hinder their usage. Therefore, various promising strategies have been used to achieve high performance earth-abundant electrocatalysts for HER and OER [7–36].

Thus, several promising strategies such as facilitate the gas evolution behavior, tuning of the electronic structure, increase the metallic character, increase the electrocatalytically active surface area (ECSA), enhance the conductivity of the electrocatalysts could improve the performance of the catalysts, and the *in situ* generation of thin layer of oxide/oxyhydroxide as highly OER active layer on the surface of the catalyst during OER could also enhance the performance of the catalysts [4,5,9–11]. Constructing nanostructured catalyst could provide superhydrophobic surface, which can reduce the bubble releasing size and bubble adhesive force by forming a discontinuous triple phase contact line (TPCL) rather than continuous TPCL, and that can enhance the gas evolution behavior [5], while it can prevent the blocking of abundant active sites, and that can boost the performance for HER and

\* Corresponding authors.

E-mail addresses: [jmohammed2-c@my.cityu.edu.hk](mailto:jmohammed2-c@my.cityu.edu.hk) (J. Mohammed-Ibrahim), [moussab.harb@kaust.edu.sa](mailto:moussab.harb@kaust.edu.sa) (H. Moussab).

<sup>1</sup> Alumi.

Peer review under responsibility of KeAi Communications Co., Ltd.

OER. Liu et al. [37] have synthesized the NiFe LDH nano sheet array on 3D Fe foam (LDH: Layered double hydroxide), which could facilitate the evolution of gas, and that could enhance the OER performance, and it exhibits  $\eta$  of 200 mV at 10 mA cm<sup>-2</sup> for OER in 1.0 M KOH, suggesting its much high activity, while it exhibits negligible decay at 1000 mA cm<sup>-2</sup> for 5000 h in 1 M KOH followed by 1050 h in 10 M KOH for OER, suggesting its robust stability. Moreover, for OER in 1 M KOH, the NiFe LDH@Cu nanoarray [38], NiFeO<sub>x</sub> nanotube array [39], Ni(Fe)O<sub>x</sub>H<sub>y</sub> nano-cone array [40], nanostructured (Ni, Fe)OOH [41], NiFeOOH-NiCo<sub>2</sub>O<sub>4</sub> nanoarray [42], and (Ni<sub>3</sub>Fe<sub>0.5</sub>-V<sub>0.5</sub>)OOH nanoarray [43] exhibit less  $\eta$  at huge current density of 1000 mA cm<sup>-2</sup>, where the nanostructured catalysts could facilitate the evolution of gas, and that could enhance the OER performance even at much high current density. Besides, for HER in 1 M KOH, the nanostructured Ni<sub>3</sub>S<sub>2</sub> [44], NiCo<sub>2</sub>P<sub>x</sub> nanowires [45], NC/CuCo/CuCoO<sub>x</sub> nanoarray [46], and WP/W nanorod array [47] exhibit remarkably much high stability, where the nanostructured catalysts could facilitate the evolution of gas, and that could enhance the HER performance. Moreover, fabricating nanostructured surface could also enhance the performance of the state-of-art, noble, catalyst such as Pt. In 0.5 M H<sub>2</sub>SO<sub>4</sub>, Li et al. [48] have observed that the pine shaped Pt nanoarray affords much higher HER activity and stability than Pt flat, where the contact angle, bubble adhesive force, and bubble releasing size of Pt nanoarray are 29.3° ± 2.5, 11.5 ± 1.2 μN, and <50 μm, respectively, while the contact angle, bubble adhesive force, and bubble releasing size of Pt flat are 81.4° ± 2.4, 145.6 ± 2.1 μN, and ~500 μm, respectively, where the superhydrophobic nanostructured surface of Pt nanoarray could evolve the H<sub>2</sub> bubbles with smaller size from the catalyst surface with weaker adhesive force, and that could provide higher intrinsic HER activity and stability for Pt nanoarray.

Tuning the electronic structure of the electrocatalysts is a promising strategy, which could produce active sites with optimal binding energy for OER intermediates, and that could decrease the energy barrier for OER, and that could enhance the activity for OER [4,8,10]. Moreover, atomic-scale investigation of the catalytic activity, evaluating the active centers located on the surface of the catalysts, screening of catalysts for improved activity and enhanced selectivity could be viable by density functional theory (DFT) calculations [49–56]. The synergistic effect between NiFe LDH and the hydroxide layer in NiFe LDH with hydroxide interfacial layer [57] could cause a favorable local chemical environment with a suitable electronic structure, and that could exhibit optimal OH intermediates adsorption (-3.184 eV) than that of pure NiFe LDH (-1.859 eV), and therefore, it exhibits  $\eta$  of 130 mV at 10 mA cm<sup>-2</sup> for OER in 0.1 M KOH, suggesting its significantly much high activity. Moreover, modified electronic structure could also be observed for NiFe LDH intercalated anions with various redox potentials [58], where the intercalated anions with low standard redox potential could transfer more electrons to the hydroxide layers, and that could increase the electron density of the surface metal sites and stabilize their high-valence states during OER. In addition, in Fe and V co-doped Ni(OH)<sub>2</sub> [43], better delocalization of the  $\pi$ -symmetry electrons can be occurred among Ni, Fe, and V in the host matrix, where Ni<sup>2+</sup> can transfer partial electrons to Fe<sup>3+</sup> through the bridging O<sup>2-</sup> via  $\pi$ -donation, while the strongly electron-deficient t<sub>2g</sub> d-orbitals of V<sup>4+</sup> and V<sup>5+</sup> can receive electrons from the electron-riched t<sub>2g</sub> d-orbitals of Fe<sup>3+</sup> through the bridging O<sup>2-</sup> ions between them, and that could stabilize the high valence states of V; Hence, instead of a strong bond strength, a moderate bond strength could be formed between V and adsorbed oxygen species due to the modified electronic structure, and that could facilitate the O<sub>2</sub> evolution from the V site during OER process. Besides, tuning the electronic structure of the electrocatalysts

could also produce active sites with optimal binding energy for HER intermediates, which could diminish the Gibbs free energy for H adsorption ( $\Delta G_{H^*}$ ) almost close to 0 eV of ideal  $\Delta G_{H^*}$ , and that could enhance the activity for HER [9]. The nanostructured Ni<sub>3</sub>N-NiMoN [59] exhibits interface between the (100) face of Ni<sub>0.2</sub>-Mo<sub>0.8</sub>N and (111) face of Ni<sub>3</sub>N suggesting the modified electronic structure, while it exhibits very tiny  $\Delta G_{H^*}$  of -0.03 eV, which has been almost close to the optimal  $\Delta G_{H^*}$  of 0 eV, and it exhibits lower water adsorption energy of -0.62 eV, and therefore, it exhibits substantially much high HER activity ( $\eta$  of -31 mV at -10 mA cm<sup>-2</sup>) in 1 M KOH. Similarly, the modified electronic structure could play vital role in several electrocatalysts to enhance their HER activity, while the Ni<sub>3</sub>FeN/reduced graphene oxide [60], Co-Ni<sub>3</sub>N [61], and NiCu@C [62] exhibit high HER activity in 1 M KOH. Moreover, fabrication of electrocatalysts with metallic character, low charge transfer resistance, and high electrocatalytic active surface area (ECSA) could improve the performance of the catalyst, while the *in situ* formation of thin oxide/oxyhydroxide layer on the catalyst surface during OER could also enhance the catalyst performance [9,10].

On the other hand, the following advantages could be obviously there by the using of seawater for producing H<sub>2</sub> through electrochemical water splitting: (a) Seawater is mostly abundant resource (~96.5% of the total earth's water resources), which could alleviate the consumption of highly demanding fresh water; (b) Higher hydrogen production rate could be observed in real seawater when compared to that of simulated seawater [56], where the cations such as Na<sup>+</sup>, Mg<sup>2+</sup>, Ca<sup>2+</sup>, K<sup>+</sup> and B<sup>3+</sup> present in real seawater could improve the conductivity; Moreover, different seawater exhibit different salinity, while the hydrogen production rate increases with salinity, which could be due to the variation of conductivity of the electrolyte with respect to the salinity of the seawater. Besides, producing H<sub>2</sub> through electrochemical water splitting could be more complicated in seawater electrolyte (natural seawater) when compared to that of the alkaline electrolyte such as in 1 M KOH or 10 M KOH, etc (Table 1). Electrolysis of seawater has some significant advantages, whereas producing hydrogen via electrochemical water splitting using seawater encounter several challenging issues, which includes: (a) Seawater splitting requires highly OER selective anode because chlorine evolution reaction (ClER) could compete with the OER [63–65], where ClER can be occurred in acidic environment (2Cl<sup>-</sup> → Cl<sub>2</sub> + 2e<sup>-</sup>; E<sup>0</sup> = ~+1.36 V<sub>SHE</sub>), while hypochlorite formation could be involved in alkaline environment (Cl<sup>-</sup> + 2OH<sup>-</sup> → ClO<sup>-</sup> + H<sub>2</sub>O + 2e<sup>-</sup>; E<sup>0</sup> = ~+0.89 V<sub>SHE</sub> at pH 14 or E<sup>0</sup> = ~+1.72 V -0.059 pH versus NHE); Two electrons are involved in both the ClER and hypochlorite formation, whereas four electrons are involved in OER in acid and alkaline environment; Therefore, ClER and hypochlorite formation could have faster kinetics than that of OER, whereas OER could be more favorable than that of hypochlorite formation from thermodynamics point of view; Moreover, in contrast to ClER, the standard electrode potential of hypochlorite formation could be pH dependent as depicted in the Pourbaix diagram (Fig. 1a) [63]; Therefore, OER could be occurred for an electrocatalyst operating at  $\eta$  of <~480 mV, whereas hypochlorite formation could be occurred for an electrocatalyst operating at  $\eta$  of >~480 mV in alkaline environment (Fig. 1b). (b) As seawater contains huge quantity of aggressive chloride anions, seawater electrolysis needs robust and efficient electrocatalysts to sustain against chloride corrosion, especially for the anode [1,66]; (c) The formation of white insoluble precipitates such as Mg(OH)<sub>2</sub> and Ca(OH)<sub>2</sub> on the surface of the cathode/anode could be possible during electrolysis, which could partially diminish the activity possibly due to the blocking of some active sites [1,67,68].

**Table 1**

Comparison of HER, OER, and overall water splitting performance of various reported electrocatalysts in different electrolyte (with and without seawater electrolyte), while the details of the natural seawater are described on the footnote of this Table.

Comparison of HER performance for NiMoN in 1 M KOH, 1 M KOH + seawater, and seawater (pH = ~7.2) electrolyte			
Electrocatalysts	Electrolyte	$\eta$ (mV) at $-100 \text{ mA cm}^{-2}$	Refs.
NiMoN	1 M KOH	-56	[1]
NiMoN	1 M KOH + seawater <sup>a†</sup>	-82	[1]
NiMoN	Seawater <sup>a†</sup> (pH = ~7.2)	-339	[1]
Comparison of OER performance for NiMoN@NiFeN in 1 M KOH, 1 M KOH + seawater, and seawater (pH = ~7.2) electrolyte			
Electrocatalysts	Electrolyte	$\eta$ (mV) at $100 \text{ mA cm}^{-2}$	Refs.
NiMoN@NiFeN	1 M KOH	277	[1]
NiMoN@NiFeN	1 M KOH + seawater <sup>a†</sup>	307	[1]
NiMoN@NiFeN	Seawater <sup>a†</sup> (pH = ~7.2)	-423	[1]
Comparison of overall water splitting performance for NiFe LDH <sup>OER</sup> //Pt/C <sup>HER</sup> in 0.1 M KOH, and 0.1 M KOH + 0.5 M NaCl electrolyte			
Electrocatalysts	Electrolyte	Cell voltage (V) at $25 \text{ mA cm}^{-2}$	Refs.
NiFe LDH <sup>OER</sup> //Pt/C <sup>HER</sup>	0.1 M KOH	~1.44	[90]
NiFe LDH <sup>OER</sup> //Pt/C <sup>HER</sup>	0.1 M KOH + 0.5 M NaCl	~1.56	[90]

Ref.: References; LDH: Layered Double Hydroxides; Seawater<sup>a†</sup>: It is natural seawater (pH = ~7.2), which is collected from Galveston Bay near Houston, Texas, USA.

Therefore, various promising strategies have been applied for electrocatalysts to achieve enhanced activity, and stability for HER and OER in seawater electrolyte. Fabricating transition metal hexacyanometallates based electrocatalysts could be used as highly OER selective anode. Guided by DFT calculations, Qiao and Bin Liu's group [64] have designed MHCM-z-BCC (MHCM: Transition metal hexacyanometallate; z-BCC: ZIF-67 on the basic cobalt carbonate surface) electrode as superior selectivity toward the OER in seawater, while, 50 and 22  $\mu\text{mol L}^{-1}$  of  $\text{Cl}_2$  have been determined from the  $\text{Pt}^{\text{OER}}//\text{Pt}^{\text{HER}}$ , and  $\text{IrO}_2^{\text{OER}}//\text{Pt}^{\text{HER}}$  electrolyzers, respectively after 12 h of continuous operation in seawater (buffered; pH ~7), whereas MHCM-z-BCC<sup>OER</sup>//NiMoS<sup>HER</sup> electrolyzer has not produced any traceable amount of  $\text{Cl}_2$  even after 100 h of continuous electrolysis suggesting its negligible side reactions. Moreover, using NiMoN@NiFeN<sup>OER</sup>//NiMoN<sup>HER</sup> electrolyzer [1] in simulated sea water electrolyte (1 M KOH with 0.5 M NaCl), only  $\text{H}_2$  and  $\text{O}_2$  gases have been detected with a molar ratio near to 2:1, while ~97.8% of Faradaic efficiency is observed during seawater electrolysis, suggesting the high selectivity for OER on the anode. Besides, CoFe LDH [69] exhibits a Faradaic efficiency of  $94 \pm 4\%$  at  $\eta$  of 560 mV. In addition to the deviation in Faradaic efficiency for  $\text{O}_2$  evolution during OER, the deviation could also be observed for  $\text{H}_2$  evolution during HER. The evolution of hydrogen from Mn-NiO-Ni [67] during HER in seawater has been verified by gas chromatography, while it exhibits ~100% of Faradaic efficiency within 1 h, whereas, deviation from linearity is observed after 1 h, where the deviation increases with time, and ~70% of Faradaic efficiency is observed at about 7 h suggesting the existence of the side reactions, which consumes the remaining ~30% of the total charge. In addition, the evolution of hydrogen from NiCoP [68] during HER in seawater has been verified for about 60 min, while it exhibits ~96.5% of Faradaic efficiency. Moreover, the amount of  $\text{H}_2$  gas evolved for 3600 s of electrolysis in seawater for  $\text{Ni}_5\text{P}_4@/\text{Ni}^{2+\delta}\text{O}_8(\text{OH})_{2-\delta}$  [70] has been measured using *in situ* gas chromatography, while it exhibits ~93% of faradaic efficiency sug-

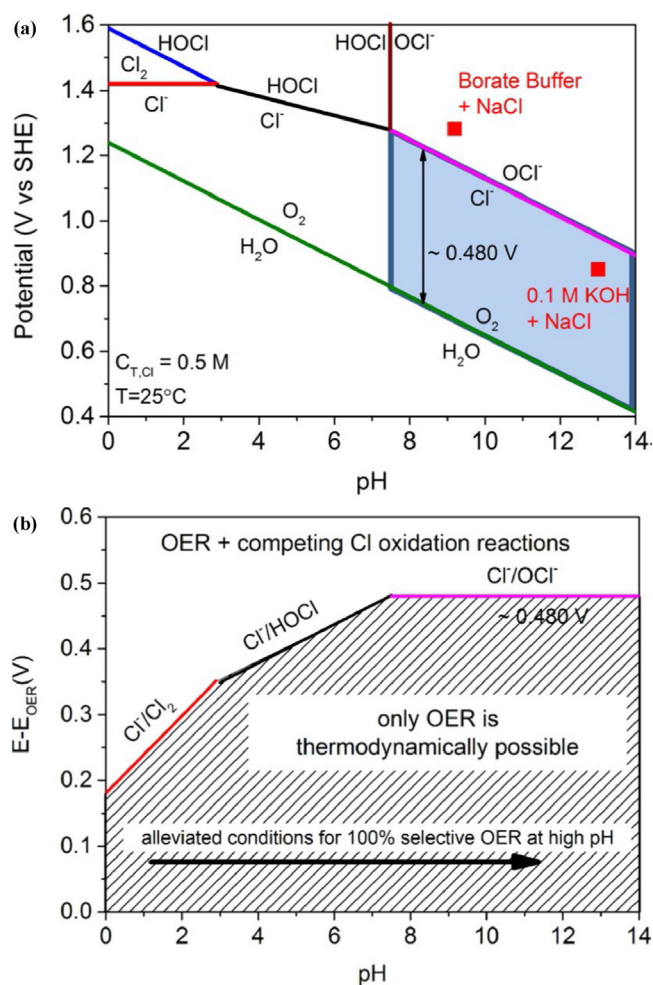


**Fig. 1.** (a) Pourbaix diagram for simulated seawater model, where the chlorine system containing the dissolved 0.5 M NaCl aqueous solution without other chlorine sources, with a total chlorine species ( $C_{T, Cl}$ ) of 0.5 M is used, while the electrode potential for OER has also been included assuming that the oxygen partial pressure of 0.21 atm is equal to 0.021 MPa; The two red square points indicate the operating potentials (vs. SHE) after 1 h electrolysis of NiFe LDH at  $10 \text{ mA cm}^{-2}$  in 0.3 M borate buffer with 0.5 M NaCl (pH 9.2; upper right side) and 0.1 M KOH with 0.5 M NaCl (pH 13; lower right side); The light blue colored area indicates the proposed design criterion; (b) Maximum permitted  $\eta$  for OER electrolyzer to ensure 100% selective OER; The values have been obtained as difference between standard electrode potentials of the three relevant chloride oxidation reactions such as chlorine, hypochlorous acid, and hypochlorite formation, and the OER versus pH; The shaded area indicates the oxygen-selective overpotential-pH conditions, here thermodynamics point to 100% selective OER, while above the limiting lines, chlorine-based reaction products have been thermodynamically possible, yet may be restricted by kinetic overpotentials (Reproduced with permission from Ref. [63]; Copyright 2016, Wiley-VCH Verlag GmbH & Co. KGaA, Weinheim).

gesting the existence of little side reactions during the electrolysis, and it exhibits 7  $\mu\text{mol}$ , 15  $\mu\text{mol}$  and 22  $\mu\text{mol}$  of hydrogen evolution at 1200 s, 2400 s and 3600 s, respectively, depicting almost linear increment suggesting its high stability. In addition, the evolution of hydrogen from NiRuR-Graphene [71] during HER in seawater has been verified by gas chromatography-mass spectrometry, while it exhibits almost 100% of Faradaic efficiency for 2 h suggesting its negligible side reactions.

As seawater contains huge quantity of aggressive chloride anions, seawater electrolysis needs robust and efficient electrocatalysts to sustain against chloride corrosion, especially for the anode [1,66]. Corrosion stability is a fraction of the long-term stability of

the electrode [7], while the corrosion stability can be inversely proportional to the degradation of electrode materials [72,73], and the corrosion stability can be modified with respect to time [74,75]. The fabrication of dual layered anode and subsequent activation could play a significant role against chloride corrosion, and that could afford long-term stability for OER in seawater electrolyte. Xiaoming Sun and Hongjie Dai's group [66] have observed that the  $\text{NiFe-NiS}_x\text{-Ni}^{\#\text{OER}}//\text{Ni-NiO-Cr}_2\text{O}_3^{\text{HER}}$  electrolyzer ( $\text{NiFe-NiS}_x\text{-Ni}^{\#\text{OER}}$ : activated  $\text{NiFe-NiS}_x\text{-Ni}$  anode) exhibits robust stability in alkaline simulated/real seawater electrolyte; It exhibits negligible decay at  $400\text{ mA cm}^{-2}$  for 1000 h in 1 M KOH with seawater, while it exhibits negligible decay at much high current density of  $1000\text{ mA cm}^{-2}$  for 500 h in 1 M KOH with 0.5 M NaCl, where the activated  $\text{NiFe-NiS}_x\text{-Ni}$  anode exhibits  $\eta$  of  $\sim 300\text{ mV}$  at  $400\text{ mA cm}^{-2}$  in 1 M KOH with 0.5 M NaCl, which is much lower than the  $\eta$  of  $\sim 480\text{ mV}$ , and therefore, this could not compete with the hypochlorite formation suggesting the highly OER selective robust anode; Moreover, the activated  $\text{NiFe-NiS}_x\text{-Ni}$  anode exhibits negligible decay for  $>500\text{ h}$  but activated  $\text{NiS}_x\text{-Ni}$  anode exhibits severe decay with  $<1\text{ h}$  when paired with  $\text{Ni-NiO-Cr}_2\text{O}_3$  cathode at  $400\text{ mA cm}^{-2}$  in 1 M KOH with 2 M NaCl (harsh electrolyte), suggesting the substantially much high stability of the activated  $\text{NiFe-NiS}_x\text{-Ni}$  anode and poor stability of the activated  $\text{NiS}_x\text{-Ni}$  anode, where the activation of  $\text{NiFe-NiS}_x\text{-Ni}$  anode could lead to the transient etching followed by the formation of polyatomic anion passivated layers (sulfate and carbonate ions could be intercalated into  $\text{NiFe LDH}$ ) and that could repel chloride anions, whereas the existence of the  $\text{LDH}$  ( $\alpha\text{-Ni(OH)}_2$ ), sulfate ions and carbonate ions are also observed in the activated  $\text{NiS}_x\text{-Ni}$  anode; Therefore, for the activated  $\text{NiFe-NiS}_x\text{-Ni}$  anode, the sulfate and carbonate ions co-intercalated  $\text{NiFe LDH}$  layer along with the underneath sulfate-rich anodized  $\text{NiS}_x$  layer could be responsible for the high corrosion resistance against chloride anions together with high OER activity during seawater electrolysis. The fabrication of metal nitride anode with core-shell structure having  $\text{NiFe}$  based shell could *in situ* form the OER active thin amorphous layers during OER, where the *in situ* formed OER active layers could also improve the corrosion resistance against chloride anions in seawater, while the core-shell structured anode could also tune the electronic structure, expose abundant active sites, enhance the charge transfer, and facilitate gas evolution, and those could enhance the OER performance in sea water. Ying Yu, Shuo Chen and Zhifeng Ren's group [1] have observed that  $\text{NiMoN@NiFeN}^{\text{OER}}//\text{NiMoN}^{\text{HER}}$  electrolyzer exhibits negligible decay at  $100\text{ mA cm}^{-2}$  for 100 h in 1 M KOH with seawater, suggesting its significantly much high stability; Moreover, the post-OER  $\text{NiMoN@NiFeN}$  sample retains its structural integrity after 1 day immersion in seawater whereas the fresh  $\text{NiMoN@NiFeN}$  sample shows apparent corrosion after 1 day immersion in seawater, and these suggest that the *in situ* generated amorphous  $\text{NiFe}$  oxide and  $\text{NiFe}$  oxy(hydroxide) layers on  $\text{NiMoN@NiFeN}$  anode after OER could enhance the corrosion resistance by chloride anions in seawater. Fabrication of porous stainless steel with high conductivity and tensile strength could expose abundant active sites, facilitate the charge transfer, and that could enhance the performance for OER. Jun Ding and Jun Min Xue's group [76] have observed that the cellular stainless steel exhibits negligible decay at  $40\text{ mA cm}^{-2}$  for 110 h, suggesting its robust stability, while it has porous structure, and it possesses high conductivity and tensile strength. Fabricating nitrogen-rich, high valence state of Mo containing, atomically thin, nanostructured  $\text{Mo}_5\text{N}_6$  could modify the electronic structure, expose abundant active sites, facilitate the charge transfer process, and that could enhance the HER performance. Yao Zheng and Shi-Zhang Qiao's group [77] have observed that the nitrogen-rich, high valence state of Mo containing, atomically thin, nanostructured  $\text{Mo}_5\text{N}_6$  exhibits significantly much high activity ( $\eta$  of  $-257\text{ mV}$  at  $-10\text{ mA cm}^{-2}$ ), while it exhibits reason-

able stability at  $\eta$  of  $-300\text{ mV}$  for 100 h for HER in seawater (Ar saturated). Fabrication of manganese doped nickel oxide/nickel hetero structure could expose abundant active sites, facilitate the charge transfer process, tune the electronic structure, and that could enhance the performance for HER. Xunyu Lu and Rose Amal's group [67] have observed that the  $\text{Mn-NiO-Ni}$  exhibits  $\eta$  of  $-170\text{ mV}$  at  $-10\text{ mA cm}^{-2}$  in seawater suggesting its significantly much high activity, while it exhibits reasonable stability at  $\eta$  of  $-140\text{ mV}$  for 14 h suggesting its high stability. Construction of nanoarray structured  $\text{NiCoP}$  could modify the electronic structure, enhance the charge transfer process, expose abundant active sites, and facilitate the evolution of gas, and that could enhance the HER performance. Lixin Cao and Bohua Dong's group [68] have observed that the feather-like nanoarray structured  $\text{NiCoP}$  exhibits  $\eta$  of  $-287\text{ mV}$  at  $-10\text{ mA cm}^{-2}$  in seawater suggesting its high activity, while it exhibits reasonable stability at  $\eta$  of  $-290\text{ mV}$  for 20 h suggesting its high stability. Fabricating nanostructured  $\text{Ni}_5\text{P}_4$  with thin amorphous nickel hydr(oxy)oxide layer could modify the electronic structure, afford optimal H adsorption/phosphide-hydrogen bond, provide optimal water adsorption, enhance the charge transfer process, expose abundant active sites, facilitate the evolution of gas, and that could enhance the performance for HER. Balogun and Tong's group [70] have observed that the  $\text{Ni}_5\text{P}_4@\text{Ni}^{2+\delta}\text{O}_8(\text{OH})_{2-\delta}$  (nanostructured  $\text{Ni}_5\text{P}_4$  with thin amorphous  $\text{Ni}^{2+\delta}\text{O}_8(\text{OH})_{2-\delta}$  layer) exhibits  $\eta$  of  $-144\text{ mV}$  at  $-10\text{ mA cm}^{-2}$  in seawater suggesting its significantly much high activity, while it exhibits negligible decay at  $-10$ ,  $-30$ ,  $-50$ , and  $-100\text{ mA cm}^{-2}$  for 40 h ( $\sim 10\text{ h}$  at each current density) suggesting its substantially much high stability. Alloying of Mo with noble metal could modify the electronic structure and enhance the charge transfer process, while the nanostructure could expose abundant active sites, and that could enhance the performance for HER. Jingjing Zheng's group [78] has observed that the  $\text{PtMo}$  alloy exhibits  $\eta$  of  $-254.6\text{ mV}$  at  $-10\text{ mA cm}^{-2}$  in seawater, suggesting its substantially much high activity, while it exhibits 91.13% retention at  $\eta$  of  $-800\text{ mV}$  for 173 h, suggesting its significantly much high stability. Moreover, Qunwei Tang's group [79] has observed that the  $\text{PtRuMo}$  alloy exhibits  $\eta$  of  $-196\text{ mV}$  at  $-10\text{ mA cm}^{-2}$  in seawater, suggesting its remarkably much high activity, while it exhibits 97.9% retention at  $\eta$  of  $-800\text{ mV}$  for 172 h suggesting its substantially much high stability. Fabrication of nanostructured ternary  $\text{NiRuIr}$  alloy anchored on graphene could enhance the performance for HER, where the alloying of Ni and Ru with Ir could modify the electronic structure and facilitate the charge transfer process, and the nanostructure morphology could expose abundant active sites, while the highly conductive graphene support could further enhance the conductivity and inhibit the aggregation of active materials. Maria Sarno's group [71] has observed that the  $\text{NiRuIr-Graphene}$  exhibits  $\sim 90\%$  retention for 200 h in seawater, suggesting its substantially much high stability. Fabricating nanostructured  $\text{T@Td-ReS}_2$  with Re vacancies having metallic T and semiconducting Td phase interface could exhibit lowest adsorption energy for  $\text{H}^+$  than that of other cationic impurities ( $\text{Mg}^{2+}$ ,  $\text{B}^{3+}$ ,  $\text{Ca}^{2+}$ ,  $\text{K}^+$ , and  $\text{Na}^+$ ), which could afford optimal  $\text{H}^+$  adsorption, while the nanostructure could expose abundant active sites, and that could enhance the performance for HER. Lizhe Liu and Xinglong Wu's group [56] have observed that the  $\text{T@Td-ReS}_2$  with Re vacancies exhibits enhanced performance for HER in seawater; Moreover, highest conductivity for the electrolyte is observed at about  $45\text{ }^\circ\text{C}$  rather than at about  $35\text{ }^\circ\text{C}$ , whereas, the  $\text{T@Td-ReS}_2$  with Re vacancies exhibits highest hydrogen production rate at about  $35\text{ }^\circ\text{C}$  rather than at about  $45\text{ }^\circ\text{C}$ , while it exhibits highest electric near-field intensity at about  $35\text{ }^\circ\text{C}$ , which could be due to the synergy of the conductivity and dielectric constant, and that could cause the highest hydrogen production rate.

Thus, various promising strategies have been applied for electrocatalysts to achieve enhanced activity, and stability for HER and OER in seawater electrolyte, whereas insight reviews on the recent advancement in terms of synthetic methodologies, chemical properties, DFT calculations, and catalytic performances on various nanostructured earth-abundant/precious-metal-containing electrocatalysts for HER and OER in seawater electrolyte have been rarely reported. In this respect, the present review provides the recent advancement in terms of synthetic methodologies, chemical properties, DFT calculations, and catalytic performances of several nanostructured earth-abundant/precious-metal-containing electrocatalysts for HER and OER in seawater electrolyte, where the discussion includes highly OER selective robust electrocatalysts such as transition metal hexacyanometallates based electrocatalyst, transition metal nitride, and LDH integrated with transition metal sulfide. At first, this review discusses the earth-abundant electrocatalysts including transition metal alloys, transition metal nitrides, transition metal oxides, transition metal doped metal oxides, transition metal phosphides, and transition metal integrated carbon nanotubes for HER in sea water (including  $\eta$  of  $\leq -200$  mV at  $-10$  mA cm $^{-2}$  for HER). Later, we review the precious metal containing electrocatalysts including precious metal containing alloys, graphene supported precious metal containing alloy, precious metal based chalcogenide with cation vacancies, and heteroatom-doped carbon supported precious metal for HER in sea water. Further, this review discusses the earth-abundant electrocatalysts including transition metal alloys, transition metal based LDH, LDH integrated with transition metal sulfide, and transition metal nitride for OER in sea water (including  $\eta$  of  $\leq 300$  mV at  $\geq 100$  mA cm $^{-2}$  for OER). Moreover, we review the noble metal containing electrocatalysts including noble metal containing alloys for OER in sea water. Then, this review discusses the earth-abundant electrocatalysts including transition metal nitride/sulfide, transition metal oxides, LDH integrated with transition metal sulfide, and transition metal hexacyanometallates based electrocatalyst for overall water splitting in sea water (including high long term stability for  $\geq 600$  h for overall water splitting). Later, we review the noble metal containing electrocatalysts for overall water splitting in sea water. Finally, this review summarizes the various promising strategies to enhance the HER and OER performance of electrocatalysts in seawater.

## 2. Electrocatalysts for HER in seawater

### 2.1. Earth-abundant electrocatalysts for HER in sea water

Alloying of Co or Cu with Ni could tune the electronic structure and enhance the charge transfer process, while the nanostructure could expose abundant active sites, and that could enhance the performance for HER. Zhang et al. [80] have compared the HER performance of Ni alloys such as NiCo, and NiCu with Ni in seawater (filtered), while the Ni alloys are fabricated on the pretreated Ti substrate by electrodeposition method, and the NiCu possesses nanostructure with feather, whereas the NiCo possesses loose structure; The XRD patterns of the Ni alloys (NiCo and NiCu) exhibit the pattern of pristine Ni, substrate Ti, and corresponding alloying element (Co or Cu), whereas, the peak positions of each alloying element have deviations with their metallic peaks, which could be due to the incorporation of alloying guest atoms into host lattices, while the crystallite size of Ni is reduced from 74.68 nm to 62.08 and 25.87 nm for NiCo and NiCu alloy, respectively, suggesting the influence of the alloying process on the growth of nanocrystallites; The charge transfer resistance of the different samples are in the following order: NiCo < NiCu < Ni; Thus, alloying of Co or Cu with Ni could tune the electronic structure and enhance the charge

transfer process, while the nanostructure expose abundant active sites, and that could enhance the performance for HER; The HER activity of the different samples are in the following order: NiCo > NiCu > Ni; For HER in seawater (filtered), the NiCo exhibits  $\eta$  of  $-1000$  mV at  $-111$  mA cm $^{-2}$ , while it exhibits negligible decay at  $\eta$  of  $-1000$  mV for  $\sim 10$  h; For HER in seawater (filtered), the NiCu exhibits  $\eta$  of  $-1000$  mV at  $-88$  mA cm $^{-2}$ , while it exhibits reasonable stability at  $\eta$  of  $-1000$  mV for  $\sim 10$  h.

Fabricating nitrogen-rich, high valence state of Mo containing, atomically thin, nanostructured Mo $_5$ N $_6$  could modify the electronic structure, expose abundant active sites, facilitate the charge transfer process, and that could enhance the HER performance. Yao Zheng and Shi-Zhang Qiao's group [77] have observed that the Mo $_5$ N $_6$  exhibits significantly much high activity and stability for HER in seawater (Ar saturated). The Mo $_5$ N $_6$  was synthesized by a Ni-induced salt-templated method through the following steps: At first, a precursor solution containing nickel acetate and Mo(OH) $_x$  was prepared; Later, a mixture was obtained by mixing the precursor solution with NaCl powder (640 g) followed by drying at 50 °C with stirring; Then, a product was formed by annealing the mixture under a 5% NH $_3$ /Ar atmosphere for 5 h at 750 °C (heating rate: 1 °C min $^{-1}$ ), where nickel acetate can be reduced to metallic Ni; Finally, Mo $_5$ N $_6$  was obtained by washing the product with deionized water and dilute hydrochloric acid for numerous times, where NaCl template and Ni nanoparticles had been removed. The Mo $_5$ N $_6$  possesses nanosheets morphology with  $\sim 3$  nm in thickness, which have been transparent and wrinkled suggesting its atomically thin 2D structure with large surface area and homogeneously exposed lattice; It is single crystalline comprising of Mo $_5$ N $_6$ ; The hexagonal structure of Mo $_5$ N $_6$  with an interplanar distance of 2.45 Å for (110) facets is observed from the scanning TEM image, and this has been smaller than that of 2.5 Å for the (200) facets of MoN, and those suggested that the hexagonal structure of Mo $_5$ N $_6$  is more compact than that of MoN; It contains high quantity of nitrogen; It contains Mo with high valence state (Mo $^{4+}$ ), which could be due to the high quantity of nitrogen atoms in the crystal lattice causing an elevated electron redistribution to N from Mo atoms; The XANES spectra of Mo $_5$ N $_6$  and MoN for N K-edge exhibit two sharp peaks and two broad peaks at lower and higher energy, respectively; The two sharp peaks at lower energy can be attributed to the transitions of N 1s electrons to the p – d(t $_{2g}$ ) and p – d(e $_g$ ) hybridized orbitals, respectively, while the two broad peaks at higher energy can be ascribed to the transition of N 1s electrons to an orbital, which includes the contributions from the 2p and 3p orbitals of nitrogen, and the d and s states of Mo; In the two sharp peaks at lower energy, when compared to the MoN, the relative peak intensity at 399.0 eV of Mo $_5$ N $_6$  has been stronger than the peak at 401.3 eV, which could be due to the transfer of more N 1s electrons to the p – d(t $_{2g}$ ) orbital suggesting the more N atoms in Mo $_5$ N $_6$ ; The total DOS of Mo $_5$ N $_6$  depicts a continuous distribution near the Fermi level, which suggests its metallic character; The calculated d band center position has been located at  $-1.96$  eV for Mo $_5$ N $_6$ , which has been almost closer to the d band center of Pt ( $-2.28$  eV) when compared to that of MoN ( $-1.75$  eV), which suggest the suitable electronic structure of Mo $_5$ N $_6$  for HER; Thus, fabrication of the nitrogen-rich, high valence state of Mo containing, atomically thin, nanostructured Mo $_5$ N $_6$  could modify the electronic structure, expose abundant active sites, facilitate the charge transfer process, and that could enhance the HER performance. For HER in seawater (Ar saturated), the Mo $_5$ N $_6$  exhibits higher HER activity than that of Ni $_{0.2}$ Mo $_{0.8}$ N, MoN and Ni $_3$ N. For HER in seawater (Ar saturated), the Mo $_5$ N $_6$  exhibits significantly much high activity ( $\eta$  of  $-257$  mV at  $-10$  mA cm $^{-2}$ ; Table 2), while it exhibits reasonable stability at  $\eta$  of  $-300$  mV for 100 h (Table 3); For HER in seawater (Ar saturated), the MoN exhibits  $\eta$  of  $\sim -520$  mV at  $-10$  mA cm $^{-2}$ , while

**Table 2**

Overpotential ( $\eta$ ) to achieve  $-10 \text{ mA cm}^{-2}$  for hydrogen evolution reaction (HER) of various reported electrocatalysts in real/simulated seawater electrolyte ( $\eta$  to achieve other than  $-10 \text{ mA cm}^{-2}$  are indicated on the  $\eta$ , which are described on the footnote of this Table, while the details of the natural seawater are described on the footnote of this Table).

HER Electrocatalysts	Electrolyte	$\eta$ at $-10 \text{ mA cm}^{-2}$ (mV)	Refs.
NiMoN	1 M KOH + 0.5 M NaCl	$\sim -80^a$	[1]
NiMoN	1 M KOH + Seawater <sup>a</sup>	$-82^b$	[1]
Ni <sub>5</sub> P <sub>4</sub> @Ni <sup>2+</sup> / <sub>6</sub> O <sub>8</sub> (OH) <sub>2-<math>\delta</math></sub>	Seawater <sup>b</sup>	$-144$	[70]
Ni-NiO-Cr <sub>2</sub> O <sub>3</sub>	1 M KOH + 0.5 M NaCl	$\sim -160^c$	[66]
Mn-NiO-Ni	Seawater <sup>c</sup>	$-170$	[67]
PtRuMo	Seawater <sup>d</sup>	$-196$	[79]
PtRuNi	Seawater <sup>d</sup>	$-206$	[79]
PtRuCo	Seawater <sup>d</sup>	$-222$	[79]
PtRuFe	Seawater <sup>d</sup>	$-248$	[79]
Co/N-C	Seawater <sup>e</sup> (buffered; pH $\sim 7$ )	$-250$	[82]
PtMo	Seawater <sup>f</sup>	$-254.6$	[78]
PtRuCr	Seawater <sup>d</sup>	$-256$	[79]
Mo <sub>5</sub> N <sub>6</sub>	Seawater <sup>g</sup> (Ar saturated)	$-257$	[77]
PtNi	Seawater <sup>f</sup>	$-263.3$	[78]
PtCo	Seawater <sup>f</sup>	$-266.5$	[78]
PtFe	Seawater <sup>f</sup>	$-275.2$	[78]
PtCr	Seawater <sup>f</sup>	$-283.8$	[78]
NiCoP	Seawater <sup>h</sup>	$-287$	[68]
Pt	Seawater <sup>f</sup>	$-305.9$	[78]
Rh-N/S-C	Seawater <sup>i</sup>	$-320$	[86]
NiMoN	Seawater <sup>a</sup>	$-339^d$	[1]
PtPd	Seawater <sup>j</sup>	$\sim -380^e$	[83]
RuCo	Seawater <sup>k</sup> (filtered)	$\sim -387$	[85]
PtNi	Seawater <sup>j</sup>	$\sim -420^f$	[83]
PtCo	Seawater <sup>j</sup>	$\sim -440^g$	[83]
Ni <sub>0.2</sub> Mo <sub>0.8</sub> N	Seawater <sup>g</sup> (Ar saturated)	$\sim -480$	[77]
PtFe	Seawater <sup>j</sup>	$\sim -480^h$	[83]
MoN	Seawater <sup>g</sup> (Ar saturated)	$\sim -520$	[77]
RuCoMo <sub>x</sub>	Seawater <sup>k</sup> (filtered)	$\sim -550$	[85]
Ni <sub>3</sub> N	Seawater <sup>g</sup> (Ar saturated)	$\sim -750$	[77]
Ni	Seawater <sup>l</sup> (filtered)	$-1000^i$	[80]
NiPt	Seawater <sup>l</sup> (filtered)	$-1000^j$	[80]
NiCo	Seawater <sup>l</sup> (filtered)	$-1000^k$	[80]
NiCu	Seawater <sup>l</sup> (filtered)	$-1000^l$	[80]
NiAu	Seawater <sup>l</sup> (filtered)	$-1000^m$	[80]
NiMo	Seawater <sup>l</sup> (filtered)	$-1000^n$	[80]
PtNi <sub>5</sub>	Seawater <sup>m</sup> (filtered)	$-1200^o$	[84]

$\eta$ : Overpotential; Ref.: References;  $\sim -80^a$ :  $\sim -80 \text{ mV}$  at  $-100 \text{ mA cm}^{-2}$ ;  $-82^b$ :  $-82 \text{ mV}$  at  $-100 \text{ mA cm}^{-2}$ ;  $\sim -160^c$ :  $\sim -160 \text{ mV}$  at  $-500 \text{ mA cm}^{-2}$ ;  $-339^d$ :  $-339 \text{ mV}$  at  $-100 \text{ mA cm}^{-2}$ ;  $\sim -380^e$ :  $\sim -380 \text{ mV}$  at  $-50 \text{ mA cm}^{-2}$ ;  $\sim -420^f$ :  $\sim -420 \text{ mV}$  at  $-50 \text{ mA cm}^{-2}$ ;  $\sim -440^g$ :  $\sim -440 \text{ mV}$  at  $-50 \text{ mA cm}^{-2}$ ;  $\sim -480^h$ :  $\sim -480 \text{ mV}$  at  $-50 \text{ mA cm}^{-2}$ ;  $-1000^i$ :  $-1000 \text{ mV}$  at  $-57 \text{ mA cm}^{-2}$ ;  $-1000^j$ :  $-1000 \text{ mV}$  at  $-172 \text{ mA cm}^{-2}$ ;  $-1000^k$ :  $-1000 \text{ mV}$  at  $-111 \text{ mA cm}^{-2}$ ;  $-1000^l$ :  $-1000 \text{ mV}$  at  $-88 \text{ mA cm}^{-2}$ ;  $-1000^m$ :  $-1000 \text{ mV}$  at  $-75 \text{ mA cm}^{-2}$ ;  $-1000^n$ :  $-1000 \text{ mV}$  at  $-45 \text{ mA cm}^{-2}$ ;  $-1200^o$ :  $-1200 \text{ mV}$  at  $-78.96 \text{ mA cm}^{-2}$ ; Seawater<sup>a</sup>: It is natural seawater (pH =  $\sim 7.2$ ), which is collected from Galveston Bay near Houston, Texas, USA; Seawater<sup>b</sup>: Natural seawater (pH: neutral); Seawater<sup>c</sup>: Natural seawater (pH:  $\sim 8.2$ ); Seawater<sup>d</sup>: Natural seawater; Seawater<sup>e</sup> (buffered; pH  $\sim 7$ ): It is natural seawater (pH:  $\sim 5.5$ ), which is then buffered to pH of  $\sim 7$ ; Seawater<sup>f</sup>: Natural seawater; Seawater<sup>g</sup> (Ar saturated): It is Ar saturated natural seawater, where the natural seawater (pH:  $\sim 8.4$ ) is collected from Henley Beach at Adelaide in Australia; Seawater<sup>h</sup>: It is natural seawater (pH:  $\sim 8.4$ ), which is collected from Yellow Sea in China; Seawater<sup>i</sup>: It is natural seawater (pH:  $\sim 8.32$ ), which is collected from Zhangzhou at Fujian in China; Seawater<sup>j</sup>: Natural seawater; Seawater<sup>k</sup> (filtered): It is filtered natural-seawater, where the seawater is collected from Yellow Sea in China; Seawater<sup>l</sup> (filtered): It is filtered natural-seawater, where the seawater (salinity:  $\sim 3.1\%$ ) is collected from Yellow Sea near Qingdao in China; Seawater<sup>m</sup> (filtered): It is filtered natural-seawater, where the seawater is collected from Yellow Sea in China.

it exhibits 99.3% retention for 4 h; For HER in seawater (Ar saturated), the Ni<sub>0.2</sub>Mo<sub>0.8</sub>N exhibits  $\eta$  of  $\sim -480 \text{ mV}$  at  $-10 \text{ mA cm}^{-2}$ , while it exhibits 49.1% retention for 4 h; For HER in seawater (Ar saturated), the Ni<sub>3</sub>N exhibits  $\eta$  of  $\sim -750 \text{ mV}$  at  $-10 \text{ mA cm}^{-2}$ ,

while it exhibits 20% retention for 4 h. The XANES spectra of Mo<sub>5</sub>N<sub>6</sub> for the Mo L<sub>III</sub> (Fig. 2a) and N K edge exhibit negligible shift before and after the 100 h stability test, while the Mo<sub>5</sub>N<sub>6</sub> retains its crystal structure after 100 h stability test, and those suggested that the active sites of Mo<sub>5</sub>N<sub>6</sub> could be well preserved from corrosion in seawater (Ar saturated) after 100 h; However, the XANES spectra for the Mo L<sub>III</sub> or Ni L and N K edge of MoN (Fig. 2b), Ni<sub>0.2</sub>Mo<sub>0.8</sub>-N, and Ni<sub>3</sub>N exhibit severe change before and after stability test suggesting their less stability in sea water (Ar saturated).

The fabrication of bimetallic nitride cathode with nano array morphology could tune the electronic structure, enhance the charge transfer process, expose abundant active sites, and facilitate gas evolution, and those could enhance the HER performance in sea water. Yu et al. [1] have observed that NiMoN exhibits enhanced activity for HER in seawater or alkaline simulated/real seawater electrolyte. The NiMoN was prepared by thermal nitridation of NiMoO<sub>4</sub> at 500 °C for 1 h under NH<sub>3</sub> and Ar atmosphere, while the NiMoO<sub>4</sub> was obtained by hydrothermal treatment of Ni foam at 150 °C for 6 h. The NiMoN is crystalline; It possesses nano-rod array morphology, and that could expose abundant active sites; It contains Mo<sup>3+</sup> and Mo<sup>6+</sup>, where the Mo 3d at 229.6 eV is attributed to the Mo<sup>3+</sup> in the metal nitride, and that could be considered as active site for HER, and that possibly enhances its performance for HER. For HER in seawater or alkaline simulated/real seawater electrolyte, the NiMoN exhibits substantially much high activity ( $\eta$  of  $-339 \text{ mV}$  at  $-100 \text{ mA cm}^{-2}$  in seawater;  $\eta$  of  $-82 \text{ mV}$  at  $-100 \text{ mA cm}^{-2}$  in 1 M KOH with seawater;  $\eta$  of  $\sim -80 \text{ mV}$  at  $-100 \text{ mA cm}^{-2}$  in 1 M KOH with 0.5 M NaCl).

Preparing Ni-NiO/Cr<sub>2</sub>O<sub>3</sub> hybrid catalyst could form the chemically inert NiCrO<sub>x</sub> during HER by blending Cr<sub>2</sub>O<sub>3</sub> into NiO, and that could prevent the active sites from oxidation and aggregation, and that could enhance the activity and stability for HER [81]. Kuang et al. [66] have observed that Ni-NiO-Cr<sub>2</sub>O<sub>3</sub> exhibits significantly much high activity and stability for HER. The Ni-NiO-Cr<sub>2</sub>O<sub>3</sub> cathode was obtained by drop-drying the dispersion to coat on Ni foam followed by annealing at 300 °C, while the dispersion was prepared by sonication of the product with 30 wt% of 20 nm Ni particles, and the product was obtained by the hydrolysis of precursors at 90 °C. For HER in 1 M KOH with 0.5 M NaCl, the Ni-NiO-Cr<sub>2</sub>O<sub>3</sub> exhibits outstanding activity ( $\sim -160 \text{ mV}$  at  $-500 \text{ mA cm}^{-2}$ ), while it exhibits robust stability (negligible decay at  $\eta$  of  $-390 \text{ mV}$  for  $\sim 22 \text{ h}$ ).

Fabrication of manganese doped nickel oxide/nickel hetero structure could expose abundant active sites, facilitate the charge transfer process, tune the electronic structure, and that could enhance the performance for HER. Xunyu Lu and Rose Amal's group [67] have observed that the Mn-NiO-Ni exhibits substantially much high activity and stability for HER in seawater. The Mn-NiO-Ni was prepared by pyrolysis of Mn based MOF at 700 °C for 3 h under Ar atmosphere (Ramping rate:  $1 \text{ }^\circ\text{C min}^{-1}$ ), where the substrate Ni foam can be served as a source of Ni species, while the Mn based MOF was obtained on Ni foam by hydrothermal treatment at 110 °C for 48 h. The Mn-NiO-Ni is a composite on Ni foam, which is composed of Mn oxide and NiO-Ni hetero-structured nanoparticles, where Ni core is surrounded by NiO shell; It contains crystalline MnO, NiO and Ni; It contains Mn, Ni, C and O, which are uniformly distributed; It possesses array structure; Thus, the Mn-NiO-Ni could expose abundant active sites, facilitate the charge transfer process, tune the electronic structure, and that could enhance the performance for HER. For HER in seawater, the Mn-NiO-Ni exhibits  $\eta$  of  $-170 \text{ mV}$  at  $-10 \text{ mA cm}^{-2}$  suggesting its significantly much high activity. Moreover, the evolution of hydrogen from Mn-NiO-Ni during HER in seawater has been verified by gas chromatography; It exhibits  $\sim 100\%$  of Faradaic efficiency within 1 h, whereas, deviation from linearity is observed after 1 h, where the deviation increases

**Table 3**

Stability of various reported electrocatalysts for hydrogen evolution reaction (HER) in real/simulated seawater electrolyte, where electrolyte is indicated on the electrocatalyst, while the details of the natural seawater are described on the footnote of this Table.

HER Electrocatalysts	Chr Amp	Chr Pot	Dur (h)	Remark after stability test	Refs.
NiRuIr <sup>Seawater(n*)</sup>	Yes	NA	200	~90% retention	[71]
PtMo <sup>Seawater(f*)</sup>	Yes	NA	173	91.13% retention at η of -800 mV	[78]
PtRuMo <sup>Seawater(d*)</sup>	Yes	NA	172	97.9% retention at η of -800 mV	[79]
Mo <sub>5</sub> Ni <sub>6</sub> <sup>Seawater(g*) (Ar saturated)</sup>	Yes	NA	100	Reasonable stability at η of -300 mV	[77]
Ni <sub>5</sub> P <sub>4</sub> @Ni <sup>2+δ</sup> O <sub>8</sub> (OH) <sub>2-δ</sub> <sup>Seawater(b*)</sup>	NA	Yes	40	Negligible decay at -10, -30, -50, and -100 mA cm <sup>-2</sup>	[70]
Ni-NiO-Cr <sub>2</sub> O <sub>3</sub> <sup>1 M KOH + 0.5 M NaCl</sup>	Yes	NA	~22	Negligible decay at η of -390 mV	[66]
NiCoP <sup>Seawater(h*)</sup>	Yes	NA	20	Reasonable stability at η of -290 mV	[68]
Mn-NiO-Ni <sup>Seawater(c*)</sup>	Yes	NA	14	Reasonable stability at η of -140 mV	[67]
PtNi <sup>Seawater(f*)</sup>	Yes	NA	14	94.76% retention at η of -800 mV	[78]
PtCo <sup>Seawater(f*)</sup>	Yes	NA	14	93.87% retention at η of -800 mV	[78]
PtFe <sup>Seawater(f*)</sup>	Yes	NA	14	92.55% retention at η of -800 mV	[78]
PtCr <sup>Seawater(f*)</sup>	Yes	NA	14	90.74% retention at η of -800 mV	[78]
Pt <sup>Seawater(f*)</sup>	Yes	NA	14	82.25% retention at η of -800 mV	[78]
PtRuNi <sup>Seawater(d*)</sup>	Yes	NA	~13.9	Reasonable stability	[79]
PtRuCo <sup>Seawater(d*)</sup>	Yes	NA	~13.9	Reasonable stability	[79]
PtRuFe <sup>Seawater(d*)</sup>	Yes	NA	~13.9	Reasonable stability	[79]
PtRuCr <sup>Seawater(d*)</sup>	Yes	NA	~13.9	Reasonable stability	[79]
RuCo <sup>Seawater(k*) (filtered)</sup>	Yes	NA	12	70% retention at η of -1200 mV	[85]
RuCoMo <sub>x</sub> <sup>Seawater(k*) (filtered)</sup>	Yes	NA	12	Negligible decay at η of -1200 mV	[85]
PtNi <sub>5</sub> <sup>Seawater(m*) (filtered)</sup>	Yes	NA	12	Negligible decay at η of -800 mV	[84]
PtPd <sup>Seawater(j*)</sup>	Yes	NA	11	0.29% reduction at η of -600 mV	[83]
PtNi <sup>Seawater(j*)</sup>	Yes	NA	11	3.01% reduction at η of -600 mV	[83]
PtCo <sup>Seawater(j*)</sup>	Yes	NA	11	4.53% reduction at η of -600 mV	[83]
PtFe <sup>Seawater(j*)</sup>	Yes	NA	11	4.71% reduction at η of -600 mV	[83]
Rh-N/S-C <sup>Seawater(i*)</sup>	Yes	NA	10	95% retention	[86]
NiPt <sup>Seawater(l*) (filtered)</sup>	Yes	NA	~10	Reasonable stability at η of -1000 mV	[80]
NiCo <sup>Seawater(l*) (filtered)</sup>	Yes	NA	~10	Negligible decay at η of -1000 mV	[80]
NiCu <sup>Seawater(l*) (filtered)</sup>	Yes	NA	~10	Reasonable stability at η of -1000 mV	[80]
NiAu <sup>Seawater(l*) (filtered)</sup>	Yes	NA	~10	Reasonable stability at η of -1000 mV	[80]
NiMo <sup>Seawater(l*) (filtered)</sup>	Yes	NA	~10	Reasonable stability at η of -1000 mV	[80]
Co/N-C <sup>Seawater(e*) (buffered; pH ~7)</sup>	Yes	NA	7	Reasonable stability at η of -270 mV	[82]
Ni <sub>0.2</sub> Mo <sub>0.8</sub> N <sup>Seawater(g*) (Ar saturated)</sup>	Yes	NA	4	49.1% retention	[77]
MoN <sup>Seawater(g*) (Ar saturated)</sup>	Yes	NA	4	99.3% retention	[77]
Ni <sub>3</sub> N <sup>Seawater(g*) (Ar saturated)</sup>	Yes	NA	4	20% retention	[77]

Chr Amp: Chronoamperometry; Chr Pot: Chronopotentiometry; Dur: Duration for stability test; Ref.: References; Seawater(b\*): Natural seawater (pH: neutral); Seawater(c\*): Natural seawater (pH: ~8.2); Seawater(d\*): Natural seawater; Seawater(e\*) (buffered; pH ~7): It is natural seawater (pH: ~5.5), which is then buffered to pH of ~7; Seawater(f\*): Natural seawater; Seawater(g\*) (Ar saturated): It is Ar saturated natural seawater, where the natural seawater (pH: ~8.4) is collected from Henley Beach at Adelaide in Australia; Seawater(h\*): It is natural seawater (pH: ~8.4), which is collected from Yellow Sea in China; Seawater(i\*): It is natural seawater (pH: ~8.32), which is collected from Zhangzhou at Fujian in China; Seawater(j\*): Natural seawater; Seawater(k\*) (filtered): It is filtered natural-seawater, where the seawater is collected from Yellow Sea in China; Seawater(l\*) (filtered): It is filtered natural-seawater, where the seawater (salinity: ~3.1%) is collected from Yellow Sea near Qingdao in China; Seawater(m\*) (filtered): It is filtered natural-seawater, where the seawater is collected from Yellow Sea in China; Seawater(n\*): Natural seawater.

with time, and ~70% of Faradaic efficiency is observed at about 7 h suggesting the existence of the side reactions, which consumes the remaining ~30% of the total charge. For HER in seawater, first stability test for 14 h followed by 24 h interval followed by second stability test for ~8 h followed by 24 h interval followed by third stability test for ~5 h are performed at η of -140 mV for the Mn-NiO-Ni; It exhibits reasonable stability during the first stability test at η of -140 mV for 14 h suggesting its high stability; However, the current density decreases from ~7 mA cm<sup>-2</sup> to ~5 mA cm<sup>-2</sup> after 24 h interval followed by second stability test for ~8 h, while the current density further decreases from ~5 mA cm<sup>-2</sup> to ~3 mA cm<sup>-2</sup> after 24 h interval followed by third stability test for ~5 h; Moreover, a white deposit was observed on the surface of the Mn-NiO-Ni after first stability test for 14 h, while the XPS analysis further confirms the formation of precipitates on the cathode surface, which are comprised of Mg, Ca, and Na based precipitates (Fig. 2c); Thus, white precipitates could be deposited on the cathode surface during HER in seawater, which could consume a portion of total charge and degrade the catalytic performance by blocking the active sites; In addition, the Mn-NiO-Ni after first stability test for 14 h is subjected to acid treatment to selectively dissolve the white precipitates, where the acid treatment involves the immersion of electrode in 0.05 M HCl for 20 min under static conditions, while the acid treated Mn-NiO-Ni retains current density of ~7 mA cm<sup>-2</sup> at η of -140 mV for

~6 h, which is similar to the performance of fresh sample; Thus, after stability test in seawater, the acid treatment could regain the activity of the Mn-NiO-Ni.

Construction of nanoarray structured NiCoP could modify the electronic structure, enhance the charge transfer process, expose abundant active sites, and facilitate the evolution of gas, and that could enhance the HER performance. Lixin Cao and Bohua Dong's group [68] have observed that NiCoP exhibits much high activity and stability for HER in seawater. The NiCoP was prepared by phosphorization of NiCo precursor at 300 °C for 2 h under N<sub>2</sub> atmosphere, while the NiCo precursor was obtained on Ni foam by hydrothermal treatment at 120 °C for 6 h. The NiCoP is composed of single crystalline hexagonal NiCoP; It contains Ni, Co, and P, which are uniformly distributed; It possesses feather-like nanoarray structure with numerous veins (Fig. 2d), which could expose abundant active sites; It contains some pores on the edge of the heterostructure, which could reduce the ion-diffusion distance; It contains Ni-P bond, Ni-PO<sub>x</sub> bond, partially positive charged Ni species (Ni<sup>δ+</sup>), Co-P bond, Co-PO<sub>x</sub> bond, partially positive charged Co species (Co<sup>δ+</sup>), metal phosphides bond, phosphate species (PO<sub>4</sub><sup>3-</sup>), and partially negatively charged P species (P<sup>δ-</sup>) suggesting the modified electronic structure; Thus, feather-like nanoarray structured NiCoP could modify the electronic structure, enhance the charge transfer process, expose abundant active sites, and facilitate the evolution of gas, and that could enhance the HER

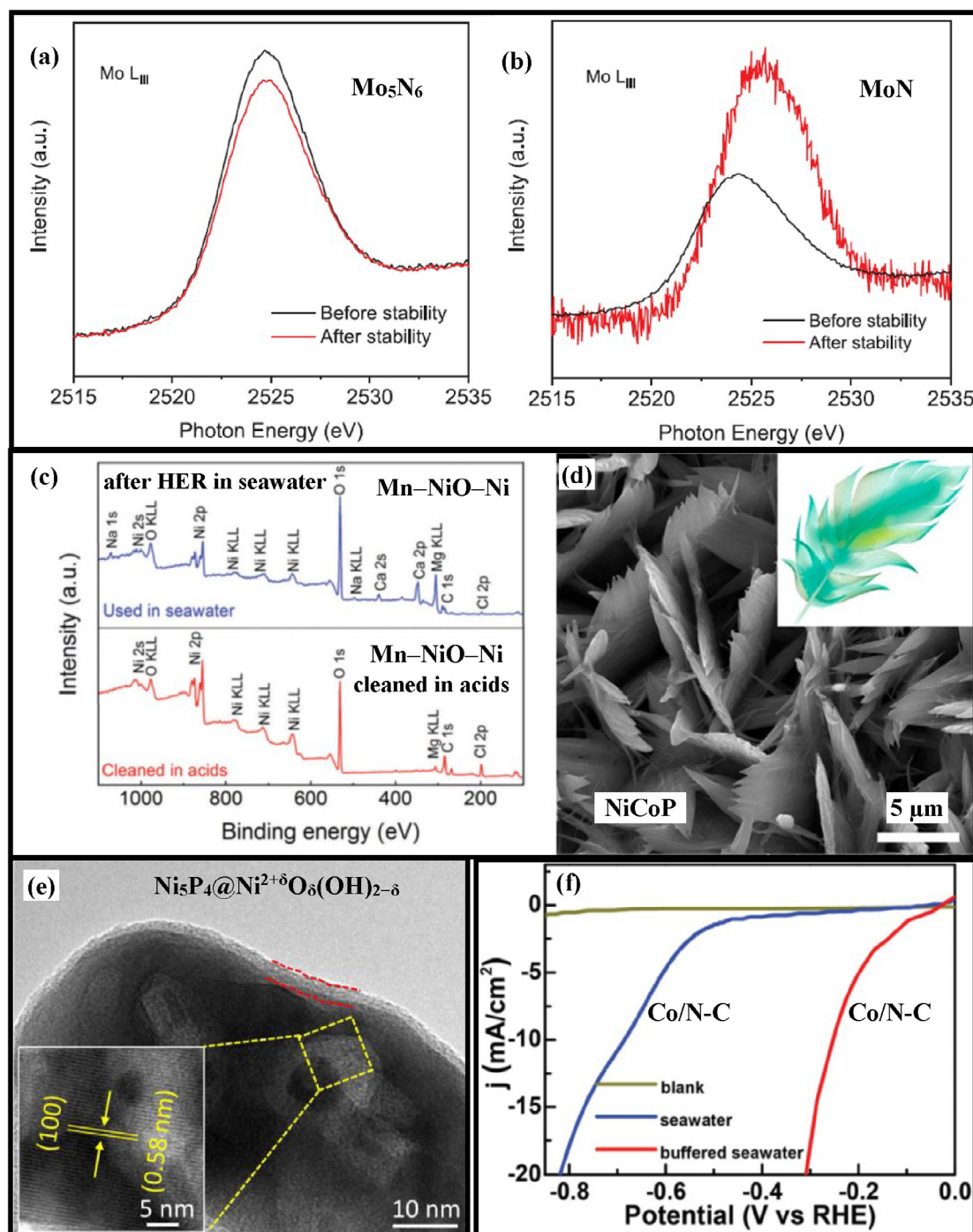


**Fig. 2.** (a, b) XANES spectra at the Mo  $L_{III}$  edge of (a)  $Mo_5N_6$  and (b)  $MoN$  before and after stability test in Ar saturated seawater (Reproduced with permission from Ref. [77]; Copyright 2018, American Chemical Society). (c) XPS survey spectra of Mn–NiO–Ni, where blue line represents the Mn–NiO–Ni after HER in seawater, while the red line indicates the Mn–NiO–Ni after HER in seawater followed by cleaning in diluted acidic solutions (Reproduced with permission from Ref. [67]; Copyright 2018, The Royal Society of Chemistry). (d) SEM image of the NiCoP (Reproduced with permission from Ref. [68]; Copyright 2019, American Chemical Society). (e) HRTEM image of  $Ni_5P_4@Ni^{2+\delta}O_\delta(OH)_{2-\delta}$  (Inset: HRTEM image depicts its corresponding lattice fringes) (Reproduced with permission from Ref. [70]; Copyright 2019, Elsevier B. V.). (f) LSV curves for HER of untreated (without catalyst) and Co/N-C, where yellow line is the blank experiment for untreated (without catalyst) in buffered seawater (pH 7), while blue line indicates the Co/N-C in natural seawater, and red line represents the Co/N-C in buffered seawater (pH 7) (Reproduced with permission from Ref. [82]; Copyright 2015, The Royal Society of Chemistry).

performance. It exhibits higher HER activity than that of CoP and  $Ni_2P$ . For HER in seawater, the NiCoP exhibits  $\eta$  of  $-287$  mV at  $-10$  mA  $cm^{-2}$  suggesting its high activity, while it exhibits reasonable stability at  $\eta$  of  $-290$  mV for 20 h suggesting its high stability; Moreover, a white precipitate is observed on the surface of the NiCoP after performing the HER stability test for 20 h; In addition, the evolution of hydrogen from NiCoP during HER in seawater

has been verified for about 60 min, while it exhibits  $\sim 96.5\%$  of Faradaic efficiency.

Fabricating nanostructured  $Ni_5P_4$  with thin amorphous nickel hydr(oxy)oxide layer could modify the electronic structure, afford optimal H adsorption/phosphide–hydrogen bond, provide optimal water adsorption, enhance the charge transfer process, expose abundant active sites, facilitate the evolution of gas, and that could

enhance the performance for HER. Balogun and Tong's group [70] have observed that the  $\text{Ni}_5\text{P}_4@\text{Ni}^{2+\delta}\text{O}_8(\text{OH})_{2-\delta}$  exhibits significantly much high activity and stability for HER in seawater. The  $\text{Ni}_5\text{P}_4@\text{Ni}^{2+\delta}\text{O}_8(\text{OH})_{2-\delta}$  was prepared by heating the  $\text{Ni}(\text{OH})_2 \cdot 0.75\text{H}_2\text{O}$  with  $\text{NaH}_2\text{PO}_2 \cdot \text{H}_2\text{O}$  at  $380^\circ\text{C}$  for 3 h under  $\text{N}_2$  atmosphere, where the  $\text{Ni}(\text{OH})_2 \cdot 0.75\text{H}_2\text{O}$  was obtained by hydrothermal treatment of cleaned carbon cloth at  $120^\circ\text{C}$  for 12 h. The  $\text{Ni}_5\text{P}_4@\text{Ni}^{2+\delta}\text{O}_8(\text{OH})_{2-\delta}$  possesses nanosheet morphology; It exhibits specific surface area of  $147.32\text{ m}^2\text{ g}^{-1}$  and pore sizes of  $33.86\text{ cm}^3\text{ g}^{-1}$ ; It is composed of crystalline hexagonal  $\text{Ni}_5\text{P}_4$ , which is covered by  $\sim 3\text{ nm}$  thin amorphous  $\text{Ni}^{2+\delta}\text{O}_8(\text{OH})_{2-\delta}$  layer (Fig. 2e), while the atomic ratio of the outer layer is 53:36:11 for Ni:P:O, and the atomic ratio of the inner layer is 44:53:3 for Ni:P:O suggesting the oxygen rich outer layer; The XPS spectra of Ni 2p and P 2p obtained from  $\text{Ni}_5\text{P}_4@\text{Ni}^{2+\delta}\text{O}_8(\text{OH})_{2-\delta}$  exhibit shift in their binding energies, while the peak shift is also observed from its Raman spectrum, suggesting the electronic interaction between  $\text{Ni}_5\text{P}_4$  and  $\text{Ni}^{2+\delta}\text{O}_8(\text{OH})_{2-\delta}$ ; Moreover, they had also performed theoretical investigation on  $\text{Ni}_5\text{P}_4@\text{Ni}^{2+\delta}\text{O}_8(\text{OH})_{2-\delta}$ ; Charge density distributions have been derived from DFT calculations, the  $\text{Ni}_5\text{P}_4@\text{Ni}^{2+\delta}\text{O}_8(\text{OH})_{2-\delta}$  exhibits higher positive charge for Ni and lesser negative charge for P than that of  $\text{Ni}_5\text{P}_4$  and  $\text{Ni}^{2+\delta}\text{O}_8(\text{OH})_{2-\delta}$ , which suggest the existence of electronic interaction between  $\text{Ni}_5\text{P}_4$  and  $\text{Ni}^{2+\delta}\text{O}_8(\text{OH})_{2-\delta}$  in  $\text{Ni}_5\text{P}_4@\text{Ni}^{2+\delta}\text{O}_8(\text{OH})_{2-\delta}$ ; The  $\text{Ni}_5\text{P}_4@\text{Ni}^{2+\delta}\text{O}_8(\text{OH})_{2-\delta}$  exhibits lowest water adsorption free energy than that of  $\text{Ni}_5\text{P}_4$  and  $\text{Ni}^{2+\delta}\text{O}_8(\text{OH})_{2-\delta}$  suggesting the water adsorption on  $\text{Ni}_5\text{P}_4@\text{Ni}^{2+\delta}\text{O}_8(\text{OH})_{2-\delta}$  could be much easier, and that could enhance its HER performance; The optimal Gibbs free energy change for catalyst –  $\text{H}^*$  ( $\Delta G_{\text{H}^*}$ ) of  $\text{Ni}_5\text{P}_4@\text{Ni}^{2+\delta}\text{O}_8(\text{OH})_{2-\delta}$  is almost close to 0 eV than that of  $\text{Ni}_5\text{P}_4$  and  $\text{Ni}^{2+\delta}\text{O}_8(\text{OH})_{2-\delta}$  suggesting the optimal H adsorption on the surface of  $\text{Ni}_5\text{P}_4@\text{Ni}^{2+\delta}\text{O}_8(\text{OH})_{2-\delta}$ , where phosphide – hydrogen (P –  $\text{H}_{\text{ads}}$ ) bond could be formed during HER, and the H atoms adsorbed point could be in the direction of the  $\text{P}_3$ -hollow site of  $\text{Ni}_5\text{P}_4$ , while the electronic interaction between  $\text{Ni}_5\text{P}_4$  and  $\text{Ni}^{2+\delta}\text{O}_8(\text{OH})_{2-\delta}$  in  $\text{Ni}_5\text{P}_4@\text{Ni}^{2+\delta}\text{O}_8(\text{OH})_{2-\delta}$  could afford optimal H adsorption leading to optimal phosphide – hydrogen bond, and that could facilitate the HER process; Thus, their proposed mechanism suggested that the  $\text{Ni}_5\text{P}_4$  in  $\text{Ni}_5\text{P}_4@\text{Ni}^{2+\delta}\text{O}_8(\text{OH})_{2-\delta}$  hybrid could serve as acceptor of H, while the amorphous  $\text{Ni}^{2+\delta}\text{O}_8(\text{OH})_{2-\delta}$  in hybrid could facilitate the adsorption of  $\text{H}_2\text{O}$  molecules, which could boost the H – O cleavage to enhance the water dissociation and those could facilitate both Volmer and Heyrovsky kinetic pathways; Thus, the nanostructured  $\text{Ni}_5\text{P}_4@\text{Ni}^{2+\delta}\text{O}_8(\text{OH})_{2-\delta}$  could expose abundant active sites, facilitate the evolution of gas, enhance the charge transfer process, modify the electronic structure, afford optimal H adsorption/phosphide–hydrogen bond, provide optimal water adsorption, and that could enhance the performance for HER. The amount of  $\text{H}_2$  gas evolved for 3600 s of electrolysis in seawater for  $\text{Ni}_5\text{P}_4@\text{Ni}^{2+\delta}\text{O}_8(\text{OH})_{2-\delta}$  has been measured using *in situ* gas chromatography, while it exhibits  $\sim 93\%$  of faradaic efficiency suggesting the existence of little side reactions during the electrolysis; It exhibits  $7\ \mu\text{mol}$ ,  $15\ \mu\text{mol}$  and  $22\ \mu\text{mol}$  of hydrogen evolution at 1200 s, 2400 s and 3600 s, respectively, depicting almost linear increment suggesting its high stability. The  $\text{Ni}_5\text{P}_4@\text{Ni}^{2+\delta}\text{O}_8(\text{OH})_{2-\delta}$  exhibits higher HER activity than that of  $\text{Ni}_5\text{P}_4$  and  $\text{Ni}^{2+\delta}\text{O}_8(\text{OH})_{2-\delta}$ . For HER in seawater, the  $\text{Ni}_5\text{P}_4@\text{Ni}^{2+\delta}\text{O}_8(\text{OH})_{2-\delta}$  exhibits  $\eta$  of  $-144\text{ mV}$  at  $-10\text{ mA cm}^{-2}$  suggesting its significantly much high activity, while it exhibits negligible decay at  $-10$ ,  $-30$ ,  $-50$ , and  $-100\text{ mA cm}^{-2}$  for 40 h ( $\sim 10\text{ h}$  at each current density) suggesting its substantially much high stability; Moreover, the LSV curves of  $\text{Ni}_5\text{P}_4@\text{Ni}^{2+\delta}\text{O}_8(\text{OH})_{2-\delta}$  exhibits almost negligible decay before and after stability test, and it almost retains its phase and morphology after stability test, and it almost retains the electronic states of Ni and P, suggesting its significantly much high stability.

Fabricating bamboo-like multi-walled carbon nanotubes with carbon-coated cobalt nanoparticles and the nitrogen dopants could

exhibit the synergistic effect of carbon-coated cobalt nanoparticles and the nitrogen dopants, and that could facilitate the charge transfer process, expose abundant active sites, enhance the conductivity, and that could enhance the HER performance. Xiaoxin Zou's group [82] has observed that Co/N-C exhibits much high activity and stability for HER in seawater (buffered; pH  $\sim 7$ ). The Co/N-C was prepared by the following steps: At first, a product was synthesized by thermal treatment of a mixture of  $\text{CoCl}_2 \cdot 6\text{H}_2\text{O}$  and urea at  $900^\circ\text{C}$  for 3 h under  $\text{N}_2$  atmosphere; Finally, Co/N-C was obtained by acid treatment ( $0.5\text{ M H}_2\text{SO}_4$ ) of the product for 48 h to etch away Co species present outside the carbon nanotubes. The Co/N-C contains multi-walled carbon nanotubes having bamboo-like morphology (wall thickness:  $2\text{--}10\text{ nm}$ ), while it contains Co nanoparticles, which are encapsulated by carbon, where the Co nanoparticles encapsulated by carbon have been present either inside or at the tip of the carbon nanotubes; It contains C – C, C = N, C = O, and C – O; It contains pyridinic and quaternary nitrogen; It exhibits 4.3:100 atomic ratio of N:C; It exhibits  $I_D/I_G$  ratio of about 0.67, while the structural defects could be caused by the presence of N dopants; Thus, the synergistic effect of carbon-coated cobalt nanoparticles and the nitrogen dopants of Co/N-C could facilitate the charge transfer process, expose abundant active sites, enhance the conductivity, and that could enhance the HER performance. For HER, the Co/N-C exhibits significantly much higher activity in seawater (buffered; pH  $\sim 7$ ) than that in natural seawater (Bohai Sea; pH  $\sim 5.5$ ), which suggested that buffering the seawater at neutral pH could enhance the activity for HER (Fig. 2f). For HER in seawater (buffered; pH  $\sim 7$ ), the Co/N-C exhibits  $\eta$  of  $-250\text{ mV}$  at  $-10\text{ mA cm}^{-2}$  suggesting its much high activity, while it exhibits reasonable stability at  $\eta$  of  $-270\text{ mV}$  for 7 h.

Alloying of Co or Cu with Ni could tune the electronic structure and enhance the charge transfer process, while the nanostructure could expose abundant active sites, and that could enhance the performance for HER. Thus, the NiCo and NiCu exhibit higher HER activity and lower charge transfer resistance than that of Ni in seawater (filtered), while the crystallite size of Ni is reduced from  $74.68\text{ nm}$  to  $62.08$  and  $25.87\text{ nm}$  for NiCo and NiCu alloy, respectively [80]. Fabricating nitrogen-rich, high valence state of Mo containing, atomically thin, nanostructured  $\text{Mo}_5\text{N}_6$  could modify the electronic structure, expose abundant active sites, facilitate the charge transfer process, and that could enhance the HER performance. Thus, the nitrogen-rich, high valence state of Mo containing, atomically thin, nanostructured  $\text{Mo}_5\text{N}_6$  exhibits significantly much high activity and stability for HER in seawater (Ar saturated) [77]. The fabrication of bimetallic nitride cathode with nano array morphology could tune the electronic structure, enhance the charge transfer process, expose abundant active sites, and facilitate gas evolution, and those could enhance the HER performance in sea water. Thus, the nanostructured NiMoN exhibits enhanced activity for HER in seawater or alkaline simulated/real seawater electrolyte [1]. Preparing Ni-NiO/ $\text{Cr}_2\text{O}_3$  hybrid catalyst could form the chemically inert  $\text{NiCrO}_x$  during HER by blending  $\text{Cr}_2\text{O}_3$  into NiO, and that could prevent the active sites from oxidation and aggregation, and that could enhance the activity and stability for HER [81]. Thus, the Ni-NiO- $\text{Cr}_2\text{O}_3$  exhibits significantly much high activity and stability for HER in  $1\text{ M KOH}$  with  $0.5\text{ M NaCl}$  [66]. Fabrication of manganese doped nickel oxide/nickel hetero structure could expose abundant active sites, facilitate the charge transfer process, tune the electronic structure, and that could enhance the performance for HER. Thus, the Mn-NiO-Ni exhibits substantially much high activity and stability for HER in seawater [67]. Construction of nanoarray structured NiCoP could modify the electronic structure, enhance the charge transfer process, expose abundant active sites, and facilitate the evolution of gas, and that could enhance the HER performance. Thus, the

nanostructured NiCoP exhibits much high activity and stability for HER in seawater [68]. Fabricating nanostructured Ni<sub>5</sub>P<sub>4</sub> with thin amorphous nickel hydr(oxy)oxide layer could modify the electronic structure, afford optimal H adsorption/phosphide – hydrogen bond, provide optimal water adsorption, enhance the charge transfer process, expose abundant active sites, facilitate the evolution of gas, and that could enhance the performance for HER. Thus, the nanostructured Ni<sub>5</sub>P<sub>4</sub>@Ni<sup>2+δ</sup>O<sub>8</sub>(OH)<sub>2–δ</sub> exhibits significantly much high activity and stability for HER in seawater [70]. Fabricating bamboo-like multi-walled carbon nanotubes with carbon-coated cobalt nanoparticles and the nitrogen dopants could exhibit the synergistic effect of carbon-coated cobalt nanoparticles and the nitrogen dopants, and that could facilitate the charge transfer process, expose abundant active sites, enhance the conductivity, and that could enhance the HER performance. Thus, the Co/N-C exhibits much high activity and stability for HER in seawater (buffered; pH ~7) [82].

## 2.2. Precious metal containing electrocatalysts for HER in sea water

Alloying of Mo, Ni, Co, Fe, or Cr with Pt could modify the electronic structure and enhance the charge transfer process, while the nanostructure could expose abundant active sites, and that could enhance the performance for HER. Jingjing Zheng's group [78] has compared the HER performance of Pt alloys such as PtMo, PtNi, PtCo, PtFe, and PtCr with Pt in seawater, while the Pt alloys are fabricated on the Ti mesh by cyclic voltammetry deposition. The PtMo possesses nanoparticles morphology (particle size: <10 nm); It exhibits the face-centered-cubic structure of Pt, whereas the incorporation of alloying guest atoms into host lattices alters the crystal size of Pt without varying the crystal structure, suggesting the influence of the alloying process, while it contains plenty of lattice distortions and defects; Moreover, XPS spectra of the Pt4f for PtMo alloy exhibits peak downshift in comparison with pristine Pt, where the diminished binding energies of Pt4f core electrons could be ascribed to the electronic interactions between the atomic orbitals of Pt and alloying guest atoms, and that could cause the partial electron transfer to Pt from alloying guest atoms, while, the XPS spectra of Mo 3d for PtMo alloy exhibit peak downshift suggesting the modified electronic structure; The charge transfer resistance of the different samples are in the following order: PtMo < PtNi < PtCo < PtFe < PtCr < Pt; Thus, alloying of Mo, Ni, Co, Fe, or Cr with Pt could tune the electronic structure and enhance the charge transfer process, while the nanostructure could expose abundant active sites, and that could enhance the performance for HER. The HER activity of the different samples are in the following order: PtMo > PtNi > PtCo > PtFe > PtCr > Pt; For HER in seawater, the PtMo exhibits  $\eta$  of –254.6 mV at –10 mA cm<sup>-2</sup>, suggesting its substantially much high activity, while it exhibits 91.13% retention at  $\eta$  of –800 mV for 173 h, suggesting its significantly much high stability; For HER in seawater, the PtNi exhibits  $\eta$  of –263.3 mV at –10 mA cm<sup>-2</sup>, suggesting its substantially much high activity, while it exhibits 94.76% retention at  $\eta$  of –800 mV for 14 h, suggesting its much high stability; For HER in seawater, the PtCo exhibits  $\eta$  of –266.5 mV at –10 mA cm<sup>-2</sup>, suggesting its substantially much high activity, while it exhibits 93.87% retention at  $\eta$  of –800 mV for 14 h, suggesting its much high stability; For HER in seawater, the PtFe exhibits  $\eta$  of –275.2 mV at –10 mA cm<sup>-2</sup>, suggesting its substantially much high activity, while it exhibits 92.55% retention at  $\eta$  of –800 mV for 14 h, suggesting its much high stability; For HER in seawater, the PtCr exhibits  $\eta$  of –283.8 mV at –10 mA cm<sup>-2</sup>, suggesting its substantially much high activity, while it exhibits 90.74% retention at  $\eta$  of –800 mV for 14 h, suggesting its much high stability.

Alloying of Pd, Ni, Co, or Fe with Pt could modify the electronic structure and facilitate the charge transfer process, while the

nanostructure of the alloys could expose abundant active sites, and that could enhance the performance for HER. Zheng [83] has compared the HER performance of Pt alloys such as PtPd, PtNi, PtCo, and PtFe with Pt in seawater, where the Pt alloys have been obtained on the pretreated Ti substrate by cyclic voltammetry deposition, and the Pt alloys possess nanoparticle morphology; The XRD patterns of the Pt alloys resembles the pattern of pristine Pt, whereas the diffraction peaks of Pt alloys shift to higher 2 $\theta$  angles when compared to that of pristine Pt; Besides, XPS spectra of the Pt4f<sub>7/2</sub> for Pt alloys exhibit peak downshift in comparison with pristine Pt, while, the XPS spectra of Ni2p, Fe2p, and Co2p for Pt alloys exhibit peak upshift suggesting the modified electronic structure; The Pt alloys exhibit lower charge transfer resistance than that of Pt; Thus, alloying of Pd, Ni, Co, or Fe with Pt could modify the electronic structure and facilitate the charge transfer process, while the nanoparticle morphology could expose abundant active sites, and that could enhance the performance for HER; The HER activity of the different samples are in the following order: PtPd > PtNi > PtCo > PtFe > Pt; For HER in seawater, the PtPd exhibits  $\eta$  of ~–380 mV at –50 mA cm<sup>-2</sup>, while it exhibits 0.29% reduction at  $\eta$  of –600 mV for 11 h suggesting its high stability; For HER in seawater, PtNi exhibits  $\eta$  of ~–420 mV at –50 mA cm<sup>-2</sup>, while it exhibits 3.01% reduction at  $\eta$  of –600 mV for 11 h; For HER in seawater, PtCo exhibits  $\eta$  of ~–440 mV at –50 mA cm<sup>-2</sup>, while it exhibits 4.53% reduction at  $\eta$  of –600 mV for 11 h; For HER in seawater, PtFe exhibits  $\eta$  of ~–480 mV at –50 mA cm<sup>-2</sup>, while it exhibits 4.71% reduction at  $\eta$  of –600 mV for 11 h.

Alloying of Pt or Au with Ni could modify the electronic structure and facilitate the charge transfer process, while the nanostructure could expose abundant active sites, and that could enhance the performance for HER. Zhang et al. [80] have compared the HER performance of Ni alloys such as NiPt, and NiAu with Ni in seawater (filtered), while the Ni alloys are fabricated on the pretreated Ti substrate by electrodeposition method, and the Ni alloys possess nanostructure; The XRD patterns of the Ni alloys (NiPt and NiAu) exhibit the pattern of pristine Ni, substrate Ti, and corresponding alloying element (Pt or Au), whereas, the peak positions of each alloying element have deviations with their metallic peaks, which could be due to the incorporation of alloying guest atoms into host lattices, while the crystallite size of Ni is reduced from 74.68 nm to 29.97 and 39.29 nm for NiPt and NiAu alloy, respectively, suggesting the influence of the alloying process on the growth of nanocrystallites; The charge transfer resistance of the different samples are in the following order: NiPt < NiAu < Ni; Thus, alloying of Pt or Au with Ni could tune the electronic structure and enhance the charge transfer process, while the nanostructure could expose abundant active sites, and that could enhance the performance for HER; The HER activity of the different samples are in the following order: NiPt > NiAu > Ni; For HER in seawater (filtered), the NiPt exhibits  $\eta$  of –1000 mV at –172 mA cm<sup>-2</sup>, while it exhibits reasonable stability at  $\eta$  of –1000 mV for ~10 h; For HER in seawater (filtered), the NiAu exhibits  $\eta$  of –1000 mV at –75 mA cm<sup>-2</sup>, while it exhibits reasonable stability at  $\eta$  of –1000 mV for ~10 h.

Alloying of Ni with Pt could modify the electronic structure and alter the charge transfer process, while the nanostructure could expose abundant active sites, and that could enhance the performance for HER. Zheng [84] has compared the HER performance of PtNi alloys with Ni in seawater (filtered), while the PtNi alloys are fabricated by chemical reduction method; The PtNi<sub>5</sub> exhibits the face-centered-cubic structure of Pt, whereas the incorporation of alloying guest atoms into host lattices alters the crystallite size of Pt without varying the crystal structure, where the crystallite size of PtNi<sub>5</sub> is reduced to 2.764 nm from 7.972 nm of Pt, suggesting the influence of the alloying process; It possesses nanostructure with high specific surface area of 274.1 m<sup>2</sup>g<sup>-1</sup>. The PtNi<sub>5</sub> exhibits lower charge transfer resistance than that of Pt<sub>3</sub>Ni, PtNi,

PtNi<sub>3</sub>, PtNi<sub>7</sub>, and PtNi<sub>10</sub>. Thus, alloying of Ni with Pt could tune the electronic structure and alter the charge transfer process, while the nanostructure could expose abundant active sites, and that could enhance the performance for HER. For HER in seawater (filtered) at  $\eta$  of  $-1200$  mV, the Pt<sub>3</sub>Ni, PtNi, PtNi<sub>3</sub>, PtNi<sub>5</sub>, PtNi<sub>7</sub>, and PtNi<sub>10</sub>, exhibit higher HER activity than that of Ni, while PtNi<sub>5</sub> exhibits higher HER activity than that of Pt<sub>3</sub>Ni, PtNi, PtNi<sub>3</sub>, PtNi<sub>7</sub>, and PtNi<sub>10</sub>. For HER in seawater (filtered), the PtNi<sub>5</sub> exhibits  $\eta$  of  $-1200$  mV at  $-78.96$  mA cm<sup>-2</sup>, while it exhibits negligible decay at  $\eta$  of  $-800$  mV for 12 h.

Alloying of Co with Ru could modify the electronic structure and alter the charge transfer process, while the nanostructure could expose abundant active sites, and that could enhance the performance for HER. Qunwei Tang's group [85] has compared the HER activity of the RuCoMo<sub>x</sub> alloys with RuCo alloy in seawater (filtered), while the RuCoMo<sub>x</sub> alloys are fabricated on pretreated Ti foil by cyclic voltammetry deposition. The RuCo possesses nanoparticles morphology (average size:  $\sim 50$  nm), while the RuCoMo<sub>7</sub> exhibits compact structure with cracks; The XRD pattern exhibits the deviation of peak for RuCo alloy, which could be due to the incorporation of Co atoms into Ru crystal lattice, while the peak shift is more apparent for the RuCoMo<sub>x</sub>; The XPS spectra of Ru 3d and Co 2p for RuCo alloy exhibit peak shift suggesting the modified electronic structure; Thus, alloying of Co with Ru could tune the electronic structure and alter the charge transfer process, while the nanostructure could expose abundant active sites, and that could enhance the performance for HER. For HER in seawater (filtered), the RuCo exhibits higher HER activity than that of RuCoMo, RuCoMo<sub>2</sub>, RuCoMo<sub>3</sub>, RuCoMo<sub>5</sub>, and RuCoMo<sub>7</sub>; For HER in seawater (filtered), the RuCo exhibits  $\eta$  of  $\sim -387$  mV at  $-10$  mA cm<sup>-2</sup>, while it exhibits 70% retention at  $\eta$  of  $-1200$  mV for 12 h; For HER in seawater (filtered), the RuCoMo<sub>x</sub> exhibits  $\eta$  of  $\sim -550$  mV at  $-10$  mA cm<sup>-2</sup>, while it exhibits negligible decay at  $\eta$  of  $-1200$  mV for 12 h.

Alloying of Mo and Ru, Ni and Ru, Co and Ru, Fe and Ru, or Cr and Ru with Pt could tune the electronic structure and facilitate the charge transfer process, while the nanostructure morphology could expose abundant active sites, and that could enhance the performance for HER. Qunwei Tang's group [79] has compared the HER performance of PtRuMo, PtRuNi, PtRuCo, PtRuFe, and PtRuCr alloys with PtRu and Pt in seawater, where the alloys are fabricated on Ti mesh by cyclic voltammetry deposition. The PtRuMo, PtRuNi, PtRuCo, PtRuFe, and PtRuCr alloys exhibit the face-centered-cubic structure of Pt, whereas the incorporation of alloying guest atoms into host lattices alters the crystal constant without varying the crystal structure of Pt, suggesting the influence of the alloying process; Besides, XPS spectra of the Pt 4f<sub>7/2</sub> and Pt 4f<sub>5/2</sub> for PtRuMo, PtRuNi, PtRuCo, PtRuFe, and PtRuCr alloys exhibit peak downshift in comparison with pristine Pt, while, the XPS spectra of Ru 3d<sub>5/2</sub> for PtRuMo, PtRuNi, PtRuCo, PtRuFe, and PtRuCr alloys exhibit peak downshift in comparison with PtRu, suggesting the modified electronic structure; The PtRuMo possesses nanostructure; The charge transfer resistance of the different samples are in the following order: PtRuMo < PtRuNi < PtRuCo < PtRuFe < PtRuCr < PtRu < Pt; Thus, alloying of Mo and Ru, Ni and Ru, Co and Ru, Fe and Ru, or Cr and Ru with Pt could modify the electronic structure and facilitate the charge transfer process, while the nanostructure morphology could expose abundant active sites, and that could enhance the performance for HER; The HER activity of the different samples are in the following order: PtRuMo > PtRuNi > PtRuCo > PtRuFe > PtRuCr > PtRu > Pt; For HER in seawater, the PtRuMo exhibits  $\eta$  of  $-196$  mV at  $-10$  mA cm<sup>-2</sup> suggesting its remarkably much high activity, while it exhibits 97.9% retention at  $\eta$  of  $-800$  mV for 172 h suggesting its substantially much high stability; For HER in seawater, the PtRuNi exhibits  $\eta$  of  $-206$  mV at  $-10$  mA cm<sup>-2</sup> suggesting its much high activity, while it exhibits reasonable stability

for  $\sim 13.9$  h; For HER in seawater, the PtRuCo exhibits  $\eta$  of  $-222$  mV at  $-10$  mA cm<sup>-2</sup> suggesting its much high activity, while it exhibits reasonable stability for  $\sim 13.9$  h; For HER in seawater, the PtRuFe exhibits  $\eta$  of  $-248$  mV at  $-10$  mA cm<sup>-2</sup> suggesting its much high activity, while it exhibits reasonable stability for  $\sim 13.9$  h; For HER in seawater, the PtRuCr exhibits  $\eta$  of  $-256$  mV at  $-10$  mA cm<sup>-2</sup> suggesting its much high activity, while it exhibits reasonable stability for  $\sim 13.9$  h.

Fabrication of nanostructured ternary NiRuIr alloy anchored on graphene could enhance the performance for HER, where the alloying of Ni and Ru with Ir could modify the electronic structure and facilitate the charge transfer process, and the nanostructure morphology could expose abundant active sites, while the highly conductive graphene support could further enhance the conductivity and inhibit the aggregation of active materials. Maria Sarno's group [71] has observed that the NiRuIr-Graphene exhibits significantly much high stability and activity for HER in seawater, while it is prepared by surfactant-free approach. The NiRuIr-Graphene is composed of NiRuIr nanoparticles (average diameter: 8 nm), which are anchored on few-layer graphene; The XRD pattern of the NiRuIr-Graphene exhibit the face-centered-cubic structure of Ir with the diffraction peaks shift to slightly higher  $2\theta$  angles, where the incorporation of alloying guest atoms (Ni and Ru) into host lattices (Ir) could alter the lattice parameters without varying the crystal structure of Ir, suggesting the influence of the alloying process, while the XRD pattern also exhibits the structure of few-layer graphene; Thus, alloying of Ni and Ru with Ir could modify the electronic structure and facilitate the charge transfer process, and the nanostructure morphology could expose abundant active sites, while the highly conductive graphene support could further enhance the conductivity and inhibit the aggregation of active materials, and that could enhance the performance for HER. For HER in seawater, the NiRuIr-Graphene exhibits  $\sim 90\%$  retention for 200 h, and it almost retains its XRD pattern with small peaks shift after stability test suggesting its substantially much high stability, while it exhibits high activity. Moreover, the evolution of hydrogen from NiRuIr-Graphene during HER in seawater has been verified by gas chromatography-mass spectrometry; It exhibits almost 100% of Faradaic efficiency for 2 h.

Fabricating nanostructured T@Td-ReS<sub>2</sub> with Re vacancies having metallic T and semiconducting Td phase interface could exhibit lowest adsorption energy for H<sup>+</sup> than that of other cationic impurities (Mg<sup>2+</sup>, B<sup>3+</sup>, Ca<sup>2+</sup>, K<sup>+</sup>, and Na<sup>+</sup>), which could afford optimal H<sup>+</sup> adsorption, while the nanostructure could expose abundant active sites, and that could enhance the performance for HER. Lizhe Liu and Xinglong Wu's group [56] have observed that the T@Td-ReS<sub>2</sub> with Re vacancies exhibits enhanced performance for HER in seawater; The T@Td-ReS<sub>2</sub> with Re vacancies was prepared by the following steps: At first, the pristine Td-ReS<sub>2</sub> crystals was synthesized by the Br<sub>2</sub>-assisted chemical vapor transport method; Finally, the T@Td-ReS<sub>2</sub> with Re vacancies was obtained by hydrothermally treatment at 80 °C for 6 h. The T@Td-ReS<sub>2</sub> with Re vacancies is composed of few-layer ReS<sub>2</sub> nanosheets comprising of the lateral 2D heterostructured interface between the metallic T and semiconducting Td phase, while it contains cationic vacancies (concentration of Re vacancies:  $\sim 6.1\%$ ); It exhibits high electron spin resonance (ESR) signal intensity, which could be ascribed to the existence of dangling bonds caused by the Re vacancies; Fig. 3(a) depicts the calculated adsorption energies for cationic impurity such as Mg<sup>2+</sup>, B<sup>3+</sup>, Ca<sup>2+</sup>, K<sup>+</sup>, Na<sup>+</sup>, and H<sup>+</sup> of T@Td-ReS<sub>2</sub> with Re and S vacancies; The T@Td-ReS<sub>2</sub> with Re vacancies exhibits smaller adsorption energy for Mg<sup>2+</sup>, B<sup>3+</sup>, Ca<sup>2+</sup>, and H<sup>+</sup> than that of T@Td-ReS<sub>2</sub> with S vacancies, and both the catalysts exhibit almost similar adsorption energy for K<sup>+</sup> and Na<sup>+</sup>, while the T@Td-ReS<sub>2</sub> with Re vacancies exhibits lowest adsorption energy for H<sup>+</sup> among all impurity ions; Subsequently, the heterostructured T@Td-ReS<sub>2</sub>

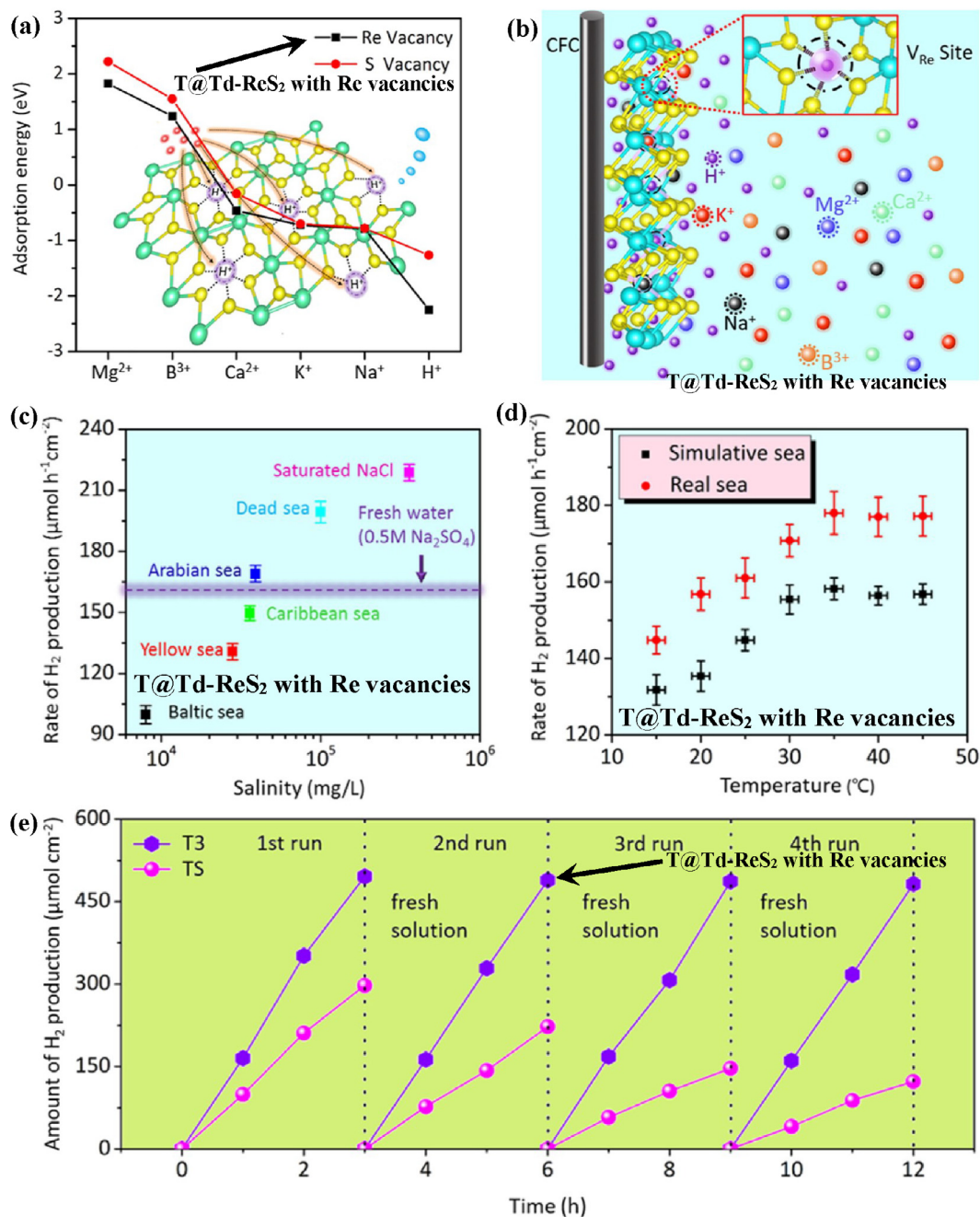


**Fig. 3.** (a) Calculated adsorption energies for cationic impurity of T@Td-ReS<sub>2</sub> with Re and S vacancies; (b) Schematic representation of cationic adsorption on the T@Td-ReS<sub>2</sub> nanosheets with Re vacancies in seawater; Comparison of hydrogen evolution of T@Td-ReS<sub>2</sub> nanosheets with Re vacancies in (c) saturated NaCl (salinity: 36 wt%) and different seawater such as Baltic Sea (salinity: 0.8 wt%), Yellow Sea (salinity: 2.8 wt%), Caribbean Sea (salinity: 3.6 wt%), Arabian Sea (salinity: 3.9 wt%) and Dead Sea (salinity: 10 wt%), and in (d) simulated and real East China seawater at -0.25 V versus RHE at different temperatures; (e) Recycling test of hydrogen generation of T@Td-ReS<sub>2</sub> nanosheets with Re vacancies and TS (ReS<sub>2</sub> with certain S vacancies) for the real East China seawater (Reproduced with permission from Ref. [56]; Copyright 2018, Elsevier Ltd.).

with Re vacancies could effectively alleviate the degeneration of active sites for water splitting; Fig. 3(b) depicts the schematic representation of cationic adsorption on the T@Td-ReS<sub>2</sub> with Re vacancies in seawater, where catalyst could effectively adsorb H<sup>+</sup> due to the lowest adsorption energy, while the impurity ions such as Mg<sup>2+</sup>, B<sup>3+</sup>, Ca<sup>2+</sup>, K<sup>+</sup>, and Na<sup>+</sup> around the catalyst could be efficiently excluded; Thus, the T@Td-ReS<sub>2</sub> with Re vacancies possesses cationic vacancies, where it exhibits lowest adsorption energy for H<sup>+</sup> than that of other cationic impurities (Mg<sup>2+</sup>, B<sup>3+</sup>, Ca<sup>2+</sup>, K<sup>+</sup>, and Na<sup>+</sup>), which could afford optimal H<sup>+</sup> adsorption, while the nanos-

tructure could expose abundant active sites, and that could enhance the performance for HER. Fig. 3(c) depicts the comparison of hydrogen evolution of T@Td-ReS<sub>2</sub> nanosheets with Re vacancies in saturated NaCl (salinity: 36 wt%) and different seawater such as Baltic Sea (salinity: 0.8 wt%), Yellow Sea (salinity: 2.8 wt%), Caribbean Sea (salinity: 3.6 wt%), Arabian Sea (salinity: 3.9 wt%) and Dead Sea (salinity: 10 wt%), and it exhibits the optimal hydrogen production rate of 216 μmol cm<sup>-2</sup>h<sup>-1</sup> in saturated salt solution, while it exhibits slightly higher hydrogen production rate in Arabian sea than in freshwater with 0.5 M sodium sulfate solution,

where the hydrogen production rate increases with salinity, and the hydrogen production rate depends on the conductivity of the electrolyte; Moreover, it exhibits higher hydrogen production rate in real seawater (East-China-seawater) than in simulated seawater, where the cations such as  $\text{Na}^+$ ,  $\text{Mg}^{2+}$ ,  $\text{Ca}^{2+}$ ,  $\text{K}^+$  and  $\text{B}^{3+}$  present in real seawater could improve the conductivity (Fig. 3d); In addition, the hydrogen production rate has been evaluated at different temperature (at about 15 °C, 20 °C, 25 °C, 30 °C, 35 °C, 40 °C, and 45 °C), where it exhibits highest hydrogen production rate at about 35 °C rather than at about 45 °C (Fig. 3d), while the highest electric near-field intensity for the catalyst is observed at about 35 °C rather than at about 45 °C, whereas highest conductivity for the electrolyte is observed at about 45 °C rather than at about 35 °C; Therefore, the hydrogen production rate could not completely depend on the conductivity of the electrolyte; Thus, the catalyst exhibits highest electric near-field intensity at about 35 °C, which could be due to the synergy of the conductivity and dielectric constant, and that could cause the highest hydrogen production rate; When the temperature is increased, then the conductivity could be increased, and that could alter the electric near-field distribution; Nevertheless, the increased electron–phonon coupling at a higher temperature could diminish the dielectric constant, and that could dissipate the electric near-field distribution; Thus, the two factors could simultaneously influence the HER performance of the catalyst, and therefore the T@Td-ReS<sub>2</sub> with Re vacancies exhibits highest hydrogen production rate at about 35 °C; Moreover, the T@Td-ReS<sub>2</sub> with Re vacancies exhibits higher stability (almost negligible decay) for hydrogen production than that of T@Td-ReS<sub>2</sub> with S vacancies (Fig. 3e), where the T@Td-ReS<sub>2</sub> with Re vacancies exhibits smaller adsorption energy for  $\text{Mg}^{2+}$ ,  $\text{B}^{3+}$ ,  $\text{Ca}^{2+}$ , and  $\text{H}^+$  than that of T@Td-ReS<sub>2</sub> with S vacancies, while the T@Td-ReS<sub>2</sub> with Re vacancies exhibits lowest adsorption energy for  $\text{H}^+$  among all other impurity ions such as  $\text{Mg}^{2+}$ ,  $\text{B}^{3+}$ ,  $\text{Ca}^{2+}$ ,  $\text{K}^+$ , and  $\text{Na}^+$  (Fig. 3a) suggesting the optimal  $\text{H}^+$  adsorption on the catalyst surface, and that could alleviate the degeneration of active sites on the T@Td-ReS<sub>2</sub> with Re vacancies (Fig. 3b), and that could enhance its stability.

The anchoring of Rh nanoparticle with N/S co-doped carbon support could modify the electronic structure, where the existence of sulfur in the N/S-C support could cause the transfer of electrons from Rh nanoparticles forming electron-rich interface between Rh and N/S-C support, while the nanostructure could expose abundant active sites, and that could enhance the HER performance. Zailai Xie's group [86] has observed that the Rh-N/S-C exhibits enhanced activity and stability for HER in seawater. The Rh-N/S-C was prepared by the following steps: At first, N/S-C was synthesized by carbonization of the solid mixture at 1000 °C for 1 h under nitrogen atmosphere followed by milling followed by carbonization at 1000 °C for 1 h under nitrogen atmosphere, where the solid mixture was obtained from biomolecule guanine and  $\text{H}_2\text{SO}_4$ ; Finally, Rh-N/S-C was prepared by wet impregnation method, where the dried mixture was obtained from  $\text{Rh}(\text{NO}_3)_3$  and support (N/S-C), while the dried mixture was heated at 250 °C for 2 h under 10%  $\text{H}_2$  atmosphere; The Rh-N/S-C exhibits higher HER activity than that of Rh-N-C. The Rh-N/S-C is composed of Rh nanoparticles, which are anchored on N/S co-doped carbon nanosheets; It contains C, N, S and Rh, which are homogeneously dispersed; The XRD pattern of the Rh-N/S-C corresponds to carbon slightly shift towards lower degree in comparison with N/S-C suggesting the interaction of Rh nanoparticles in the composite; It could contain pyrrolic N, pyridinic N, graphitic N, oxidized N, graphitic  $\text{sp}^2$  C–C,  $\text{sp}^2$  C–N, C–S–C, and C–SO<sub>x</sub>–C; The high-resolution XPS spectrum of the Rh 3d for Rh-N/S-C exhibits peak upshift in comparison with Rh-N-C, whereas the XPS spectra of C 1s, N 1s and S 2p spectra exhibit almost negligible peak shift, which suggested

that the electrons of Rh nanoparticle in Rh-N/S-C could be transferred to the interface between Rh nanoparticles and N/S-C support rather than into the N/S-C support; It possesses 2D nanosheet-like morphology with apparent wrinkles; It contains micro-meso-macro pore; It exhibits high surface area of 344.3  $\text{m}^2\text{g}^{-1}$ ; Thus, the anchoring of Rh nanoparticle with N/S-C support could modify the electronic structure, where the existence of sulfur in the N/S-C support could cause the transfer of electrons from Rh nanoparticles forming electron-rich interface between Rh and N/S-C support, while the nanostructure could expose abundant active sites, and that could enhance the HER performance. For HER in seawater, the Rh-N/S-C exhibits  $\eta$  of –320 mV at –10  $\text{mA cm}^{-2}$  suggesting its high activity, while it exhibits 95% retention for 10 h suggesting its high stability.

Alloying could modify the electronic structure and enhance the charge transfer process, while the nanostructure could expose abundant active sites, and that could enhance the performance for HER. Thus, the PtMo, PtNi, PtCo, PtFe, and PtCr exhibit higher HER activity and lower charge transfer resistance than that of Pt in seawater, where the incorporation of alloying guest atoms into host lattices alters the crystal size of Pt without varying the crystal structure [78]. Moreover, the PtPd, PtNi, PtCo, and PtFe exhibit higher HER activity than that of Pt in seawater, where the XRD patterns of the Pt alloys resembles the pattern of pristine Pt, whereas the diffraction peaks of Pt alloys shift to higher 2 $\theta$  angles when compared to that of pristine Pt [83]. In addition, the NiPt, and NiAu exhibit higher HER activity and lower charge transfer resistance than that of Ni in seawater (filtered), where the crystallite size of Ni is reduced for NiPt and NiAu alloy [80]. Moreover, the PtNi<sub>5</sub> exhibits high HER activity and low charge transfer resistance in seawater (filtered), where the incorporation of alloying guest atoms into host lattices alters the crystallite size of Pt without varying the crystal structure [84]. Besides, the RuCo alloy exhibits high HER activity and low charge transfer resistance in seawater (filtered), where the XRD pattern exhibits the deviation of peak for RuCo alloy, which could be due to the incorporation of Co atoms into Ru crystal lattice [85]. In addition, the PtRuMo, PtRuNi, PtRuCo, PtRuFe, PtRuCr, and PtRu exhibit higher HER activity and lower charge transfer resistance than that of Pt in seawater, where the incorporation of alloying guest atoms into host lattices alters the crystal constant without varying the crystal structure of Pt [79]. Fabrication of nanostructured ternary NiRuIr alloy anchored on graphene could enhance the performance for HER, where the alloying of Ni and Ru with Ir could modify the electronic structure and facilitate the charge transfer process, and the nanostructure morphology could expose abundant active sites, while the highly conductive graphene support could further enhance the conductivity and inhibit the aggregation of active materials. Thus, the NiRuIr–Graphene exhibits significantly much high stability and activity for HER in seawater [71]. Fabricating nanostructured T@Td-ReS<sub>2</sub> with Re vacancies having metallic T and semiconducting Td phase interface could exhibit lowest adsorption energy for  $\text{H}^+$  than that of other cationic impurities ( $\text{Mg}^{2+}$ ,  $\text{B}^{3+}$ ,  $\text{Ca}^{2+}$ ,  $\text{K}^+$ , and  $\text{Na}^+$ ), which could afford optimal  $\text{H}^+$  adsorption, while the nanostructure could expose abundant active sites, and that could enhance the performance for HER. Thus, the T@Td-ReS<sub>2</sub> with Re vacancies exhibits enhanced performance for HER in seawater [56]. The anchoring of Rh nanoparticle with N/S co-doped carbon support could modify the electronic structure, where the existence of sulfur in the N/S-C support could cause the transfer of electrons from Rh nanoparticles forming electron-rich interface between Rh and N/S-C support, while the nanostructure could expose abundant active sites, and that could enhance the HER performance. Thus, the Rh-N/S-C exhibits enhanced activity and stability for HER in seawater [86].

### 3. Electrocatalysts for OER in seawater

#### 3.1. Earth-abundant electrocatalysts for OER in sea water

Fabrication of nanostructured NiCo alloy could expose abundant active sites, facilitate the charge transfer process, and that could enhance the performance for OER. Zheng [87] has observed that NiCo alloy exhibits enhanced stability and activity for OER in seawater. The NiCo alloy was prepared by hydrothermal treatment at 200 °C for 12 h using diethanolamine, ethanolamine, mono-ethylene glycol, or propanediol as reducing agent, while the NiCo alloy prepared using diethanolamine exhibited higher OER activity than that of NiCo alloy prepared using ethanolamine, mono-ethylene glycol, or propanediol. The NiCo alloy is composed of crystalline NiCo alloy; It contains metallic Ni and Co; It possesses string structure, which is composed of interconnected nanospheres, and that could expose abundant active sites, facilitate the charge transfer process, and that could enhance the performance for OER. For OER in seawater, the NiCo alloy exhibits  $\eta$  of ~712 mV at 100 mA cm<sup>-2</sup>, while it exhibits 98.83% retention at  $\eta$  of 270 mV for ~40 h suggesting its high stability.

Fabrication of nanostructured NiFe LDH could expose abundant active sites, enhance electron transfer, tune the electronic structure, facilitate gas evolution, and that could enhance the OER performance. Peter Strasser's group [63] has observed that NiFe LDH/C exhibits enhanced activity and stability for OER in alkaline simulated sea water, where the NiFe LDH is prepared by solvothermal method; The NiFe LDH possesses hexagonal nanoplate morphology, and it is composed NiFe LDH nanoplates, which have been decorated with smaller amorphous FeO<sub>x</sub> particles, and that could expose abundant active sites, enhance electron transfer, tune the electronic structure, facilitate gas evolution, and that could enhance the OER performance; For OER in 0.1 M KOH with 0.5 M NaCl, the NiFe LDH/C exhibits  $\eta$  of ~359 mV at 10 mA cm<sup>-2</sup> suggesting its high activity, while it exhibits reasonable stability at 10 mA cm<sup>-2</sup> for 2 h.

Preparing nanostructured CoFe LDH could expose abundant active sites, facilitate charge transfer process, tune the electronic structure, and that could enhance the OER performance. Cheng et al. [69] have observed that CoFe LDH exhibits enhanced activity and stability for OER in simulated seawater. The CoFe LDH was prepared by separate nucleation and aging process, where the aging process was performed at 80 °C for 12 h. The CoFe LDH is composed of crystalline CoFe LDH; It possesses nanoparticle morphology; It contains 42.9:20.1 ratio of Co and Fe; It exhibits BET surface area of 40.5 m<sup>2</sup> g<sup>-1</sup>, and that could expose abundant active sites, facilitate charge transfer process, tune the electronic structure, and that could enhance the OER performance. For OER in simulated sea water, the CoFe LDH exhibits  $\eta$  of 530 mV at 10 mA cm<sup>-2</sup>, while it exhibits high stability by retaining ~86% at  $\eta$  of 560 mV for 8 h, and after OER, it almost retains its morphology, whereas the (003) diffraction has been slightly shifted to a lower angle, while the basal spacing of the LDH has been increased from 0.76 to 0.78 nm, which could be due to the insertion of Cl<sup>-</sup> into the LDH interlayers; It exhibits a Faradaic efficiency of 94 ± 4% at  $\eta$  of 560 mV. Moreover, it exhibits higher OER activity and lower charge transfer resistance in simulated sea water electrolyte than in NaCl, MgCl<sub>2</sub>, or Na<sub>2</sub>SO<sub>4</sub> suggesting the beneficial of multiple ions for the enhanced charge transfer process in simulated seawater electrolyte.

The fabrication of dual layered anode and subsequent activation could play a vital role against chloride corrosion, and that could afford long-term stability for OER in seawater electrolyte. Kuang et al. [66] have observed that NiFe-NiS<sub>x</sub>-Ni exhibits remarkably much high activity and stability for OER; The NiFe-NiS<sub>x</sub>-Ni was prepared by solvothermal reaction of annealed Ni foam followed

by electrodeposition; It is amorphous, and it is comprised of about 1 to 2 μm in thick NiS<sub>x</sub> layer on Ni foam, while the NiS<sub>x</sub> is covered by ~200 nm in thick top NiFe LDH layer; The activated NiFe-NiS<sub>x</sub>-Ni exhibits substantially much high OER activity ( $\eta$  of ~300 mV at 400 mA cm<sup>-2</sup> in 1 M KOH with 0.5 M NaCl (Table 4), where the  $\eta$  of ~480 mV is far away from the hypochlorite formation), and stability.

The fabrication of metal nitride anode with core-shell structure having NiFe based shell could *in situ* form the OER active thin amorphous layers during OER, where the *in situ* form OER active layers could also improve the corrosion resistance against chloride anions in seawater, while the core-shell structured anode could also tune the electronic structure, expose abundant active sites, enhance the charge transfer process, and facilitate gas evolution, and those could enhance the OER performance in sea water. Yu et al. [1] have observed that NiMoN@NiFeN exhibits enhanced activity for OER in seawater or alkaline simulated/real seawater electrolyte. The NiMoN@NiFeN was prepared by thermal nitridation of NiFe precursor coated NiMoO<sub>4</sub> at 500 °C for 1 h under NH<sub>3</sub> and Ar atmosphere, while the NiFe precursor coated NiMoO<sub>4</sub> was obtained by soaking the NiMoO<sub>4</sub> in NiFe precursor ink followed by drying, and the NiMoO<sub>4</sub> was obtained by hydrothermal treatment of Ni foam at 150 °C for 6 h. The NiMoN@NiFeN is crystalline; It possesses core-shell structure, where the core NiMoN nano-rods are surrounded by mesoporous NiFeN shell with ~100 nm in thickness, and that could expose abundant active sites; It contains Mo<sup>3+</sup> and Mo<sup>6+</sup>, where the binding energies of the Mo 3d are negatively shifted when compared to that of NiMoN suggesting the strong electronic interactions between NiMoN and NiFeN; It exhibit the *in situ* formation of thin amorphous layers of NiFe oxide and NiFe oxy(hydroxide) during OER, where the *in situ* form OER active layers could also enhance the corrosion resistance against chloride anions in seawater, and that possibly enhances its performance for OER. For OER in seawater or alkaline simulated/real seawater electrolyte, the NiMoN@NiFeN exhibits significantly much high activity ( $\eta$  of 288 mV at 50 mA cm<sup>-2</sup> in seawater;  $\eta$  of 307 mV at 100 mA cm<sup>-2</sup> in 1 M KOH with seawater;  $\eta$  of 286 mV at 100 mA cm<sup>-2</sup> in 1 M KOH with 0.5 M NaCl).

**Table 4**  
Overpotential ( $\eta$ ) and its corresponding current density for oxygen evolution reaction (OER) of various reported electrocatalysts in real/simulated seawater electrolyte, while the details of the natural seawater are described on the footnote of this Table.

OER Electrocatalysts	Electrolyte	$\eta$ and its corresponding current density	Refs.
NiFeN@NiMoN	1 M KOH + 0.5 M NaCl	286 mV at 100 mA cm <sup>-2</sup>	[1]
NiFeN@NiMoN	Seawater <sup>a</sup>	288 mV at 50 mA cm <sup>-2</sup>	[1]
NiFe-NiS <sub>x</sub> -Ni <sup>activated</sup>	1 M KOH + 0.5 M NaCl	~300 mV at 400 mA cm <sup>-2</sup>	[66]
NiFeN@NiMoN	1 M KOH + seawater <sup>a</sup>	307 mV at 100 mA cm <sup>-2</sup>	[1]
NiFe LDH/C	0.1 M KOH + 0.5 M NaCl	~359 mV at 10 mA cm <sup>-2</sup>	[63]
CoFe LDH	Simulated seawater <sup>p</sup>	530 mV at 10 mA cm <sup>-2</sup>	[69]
NiCo	Seawater <sup>o</sup>	~712 mV at 100 mA cm <sup>-2</sup>	[87]
PtPd	Seawater <sup>i</sup>	~900 mV at 100 mA cm <sup>-2</sup>	[83]
PtNi	Seawater <sup>i</sup>	~1300 mV at 100 mA cm <sup>-2</sup>	[83]
PtCo	Seawater <sup>i</sup>	~1540 mV at 100 mA cm <sup>-2</sup>	[83]
PtFe	Seawater <sup>i</sup>	~1640 mV at 100 mA cm <sup>-2</sup>	[83]

$\eta$ : Overpotential; Ref.: References; LDH: Layered Double Hydroxides; Seawater<sup>a</sup>: It is natural seawater (pH = ~7.2), which is collected from Galveston Bay near Houston, Texas, USA; Seawater<sup>i</sup>: Natural seawater; Seawater<sup>o</sup>: Natural seawater (pH = ~6.64); Simulated seawater<sup>p</sup>: It is simulated seawater (pH = ~8), which is prepared by dissolving 17.5 g of sea salt in 500 mL of deionized water, while the sea salt has been purchased from Qingdao Sea-Salt Aquarium Technology Co. Ltd. in China.

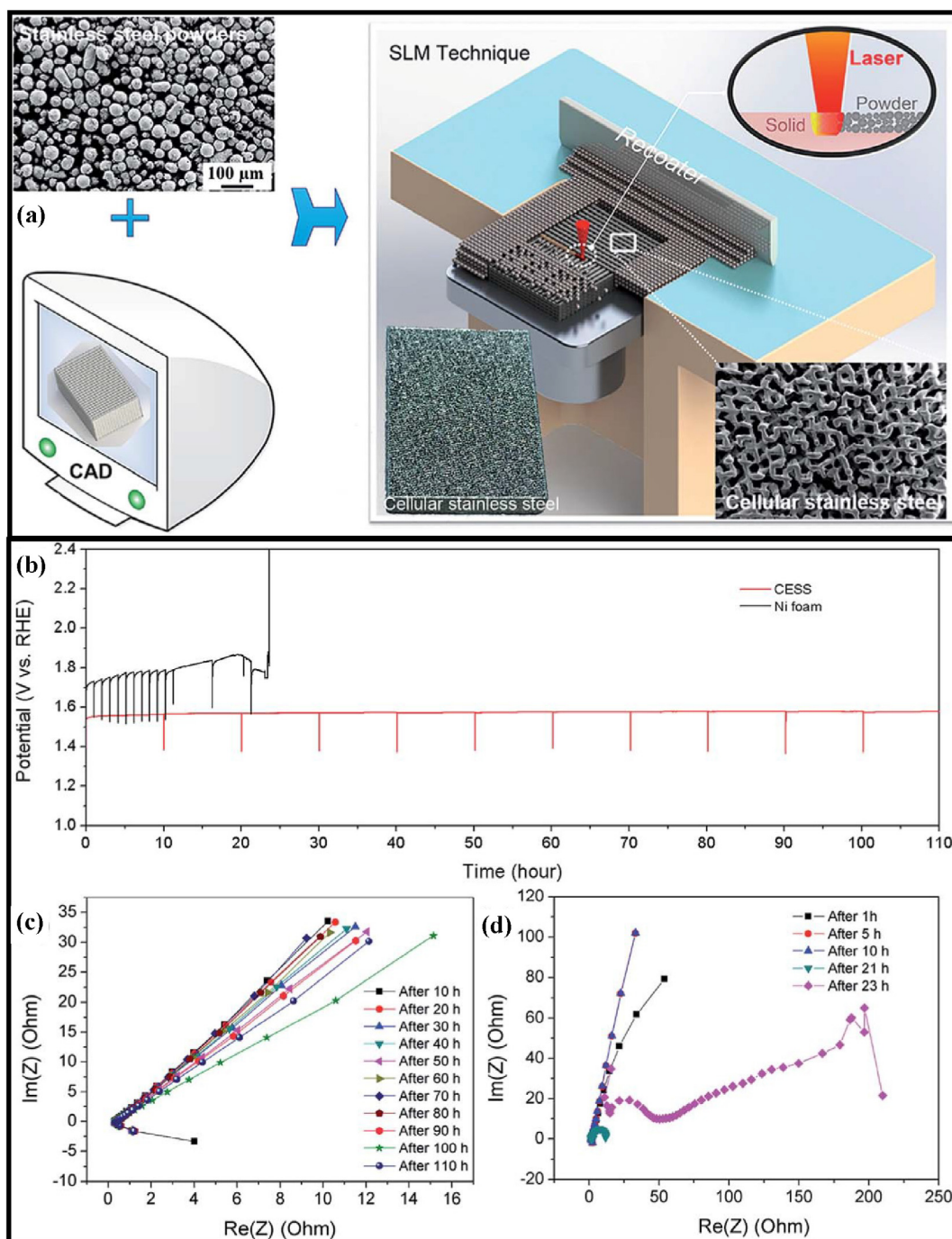


**Fig. 4.** (a) Schematic illustration of the fabrication process of the cellular stainless steel; (b) Chronopotentiometric response of cellular stainless steel (for 110 h) in comparison with Ni foam (for ~23.4 h) at  $40 \text{ mA cm}^{-2}$  in 1 M KOH with 0.6 M NaCl; Nyquist plots of (c) cellular stainless steel and (d) Ni foam at different time intervals during stability test (Reproduced with permission from Ref. [76]; Copyright 2017, The Royal Society of Chemistry).

Fabrication of porous stainless steel with high conductivity and tensile strength could expose abundant active sites, facilitate the charge transfer process, and that could enhance the performance for OER. Jun Ding and Jun Min Xue's group [76] have observed that cellular stainless steel exhibits substantially much high stability and activity for OER in simulated seawater. The cellular stainless steel was printed by a selective laser melting technique using spherical stainless steel powder under  $\text{N}_2$  atmosphere, where the laser beam with a wavelength of 1070 nm was used (Fig. 4a). It exhibits significantly much high tensile strength of ~160.0 MPa, which is about 10, 114, and 533 times higher than that of the com-

mercial stainless steel foam (~16.2 MPa), commercial nickel foam (~1.4 MPa), and commercial copper foam (~0.3 MPa), respectively. It exhibits high conductivity of  $39\,000 \text{ S cm}^{-1}$ , which is higher than that of commercial stainless steel foam ( $9200 \text{ S cm}^{-1}$ ). It exhibits high tensile strength and conductivity; It contains Fe, Ni, Cr, Mo, N, C, P and O; It contains thin oxide layer on its surface; It possesses porous structure, and that could expose abundant active sites, facilitate charge transfer process, and that could enhance the OER performance. For OER in 1 M KOH with 0.6 M NaCl, the cellular stainless steel exhibits negligible decay at  $40 \text{ mA cm}^{-2}$  for 110 h (Fig. 4b; Table 5), and it exhibits low charge transfer resistance

**Table 5**

Stability of various reported electrocatalysts for oxygen evolution reaction (OER) in real/simulated seawater electrolyte, while the details of the natural seawater are described on the footnote of this Table.

OER Electrocatalysts	Electrolyte	Chr Amp	Chr Pot	Dur (h)	Remark after stability test	Ref.s
Cellular stainless steel	1 M KOH + 0.6 M NaCl	NA	Yes	110	Negligible decay at 40 mA cm <sup>-2</sup>	[76]
NiCo	Seawater <sup>o†</sup>	Yes	NA	~40	98.83% retention at η of 270 mV	[87]
PtPd	Seawater <sup>l†</sup>	Yes	NA	~12	Negligible decay	[83]
PtFe	Seawater <sup>l†</sup>	Yes	NA	12	Reasonable stability	[83]
PtCo	Seawater <sup>l†</sup>	Yes	NA	~11	Reasonable stability	[83]
PtNi	Seawater <sup>l†</sup>	Yes	NA	~10	Negligible decay	[83]
CoFe LDH	Simulated seawater <sup>p†</sup>	Yes	NA	8	~86% retention at η of 560 mV	[69]
NiFe LDH/C	0.1 M KOH + 0.5 M NaCl	NA	Yes	2	Reasonable stability at 10 mA cm <sup>-2</sup>	[63]

Chr Amp: Chronoamperometry; Chr Pot: Chronopotentiometry; Dur: Duration for stability test; Ref.: References; LDH: Layered Double Hydroxides; Seawater<sup>l†</sup>: Natural seawater; Seawater<sup>o†</sup>: Natural seawater (pH = ~6.64); Simulated seawater<sup>p†</sup>: It is simulated seawater (pH = ~8), which is prepared by dissolving 17.5 g of sea salt in 500 mL of deionized water, while the sea salt has been purchased from Qingdao Sea-Salt Aquarium Technology Co. Ltd. in China.

after 110 h (Fig. 4c) suggesting its robust stability, whereas the Ni foam exhibits obvious decay after ~23 h (Fig. 4b), and the Ni foam exhibits high charge transfer resistance after ~23 h (Fig. 4d) suggesting its poor stability possibly due to the oxidation of metallic Ni.

Fabrication of nanostructured NiCo alloy could expose abundant active sites, facilitate the charge transfer process, and that could enhance the performance for OER. Thus, the NiCo alloy exhibits enhanced stability and activity for OER in seawater [87]. Fabrication of nanostructured NiFe LDH could expose abundant active sites, enhance electron transfer, tune the electronic structure, facilitate gas evolution, and that could enhance the OER performance. Thus, the NiFe LDH/C exhibits enhanced activity and stability for OER in alkaline simulated sea water [63]. Moreover, the CoFe LDH exhibits enhanced activity and stability for OER in simulated seawater [69]. The fabrication of dual layered anode and subsequent activation could play a vital role against chloride corrosion, and that could afford long-term stability for OER in seawater electrolyte. Thus, the NiFe-NiS<sub>x</sub>-Ni exhibits remarkably much high activity and stability for OER [66]. The fabrication of metal nitride anode with core-shell structure having NiFe based shell could *in situ* form the OER active thin amorphous layers during OER, where the *in situ* form OER active layers could also improve the corrosion resistance against chloride anions in seawater, while the core-shell structured anode could also tune the electronic structure, expose abundant active sites, enhance the charge transfer process, and facilitate gas evolution, and those could enhance the OER performance in sea water. Thus, the NiMoN@NiFeN exhibits enhanced activity for OER in seawater or alkaline simulated/real seawater electrolyte [1]. Fabrication of porous stainless steel with high conductivity and tensile strength could expose abundant active sites, facilitate the charge transfer process, and that could enhance the performance for OER. Thus, the cellular stainless steel exhibits substantially much high stability and activity for OER in simulated seawater [76].

### 3.2. Noble metal containing electrocatalysts for OER in sea water

Alloying of Pd, Ni, Co, or Fe with Pt could tune the electronic structure and enhance the charge transfer process, while the nanostructure of the alloys could expose abundant active sites, and that could enhance the performance for OER. Zheng [83] has compared the OER performance of Pt alloys such as PtPd, PtNi, PtCo, and PtFe with Pt in seawater, where the Pt alloys are prepared on the pretreated Ti substrate by cyclic voltammetry deposition, and the Pt alloys possess nanoparticle morphology; The XRD patterns of the Pt alloys resembles the pattern of pristine Pt, whereas the diffraction peaks of Pt alloys shift to higher 2θ angles compared to the pristine Pt, which could be due to the formation of Pt-metal bonds by the incorporation of alloying metal atoms into

the face-centered cubic structure of Pt, and that could alter the lattice parameters; The high-resolution XPS spectra of the Pt4f<sub>7/2</sub> for PtFe (71.27 eV), PtCo (71.11 eV), PtNi (71.12 eV), and PtPd (71.23 eV) exhibit peak downshift of 0.03, 0.19, 0.28 and 0.07 eV, respectively, in comparison with pristine Pt (71.3 eV), while, the XPS spectra of Ni2p, Fe2p, and Co2p for PtNi, PtFe, and PtCo exhibit peak upshift in comparison with metallic Ni, Fe, and Co, and those suggest the electronic interactions of atomic orbitals between Pt and alloying elements, and that could transfer the charge from alloying elements to Pt causing electronic redistribution on Pt surface; The charge transfer resistance of the different samples are in the following order: PtPd < PtNi < PtCo < PtFe < Pt; Thus, alloying of Pd, Ni, Co, or Fe with Pt could tune the electronic structure and enhance the charge transfer process, while the nanoparticle morphology could expose abundant active sites, and that could enhance the performance for OER; The OER activity of the different samples are in the following order: PtPd > PtNi > PtCo > PtFe > Pt; For OER in seawater, the PtPd exhibits η of ~900 mV at 100 mA cm<sup>-2</sup>, while it exhibits negligible decay for ~12 h suggesting its high stability; For OER in seawater, PtNi exhibits η of ~1300 mV at 100 mA cm<sup>-2</sup>, while it exhibits negligible decay for ~10 h suggesting its high stability; For OER in seawater, PtCo exhibits η of ~1540 mV at 100 mA cm<sup>-2</sup>, while it exhibits reasonable stability for ~ 11 h; For OER in seawater, PtFe exhibits η of ~1640 mV at 100 mA cm<sup>-2</sup>, while it exhibits reasonable stability for 12 h.

## 4. Electrocatalysts for overall water splitting in seawater

### 4.1. Earth-abundant electrocatalysts for overall water splitting in sea water

The fabrication of karst Ni foam could produce heterostructures, and modify the electronic structure, while it could *in situ* generate the polyatomic sulfate passivating layers during OER on anode, and that could enhance the activity and stability for overall water splitting in seawater. Wei Zhang, Qiang Wang, and Rui Cao's group [88] have observed that the karst Ni foam//karst Ni foam exhibits enhanced activity and stability for overall water splitting in seawater electrolyte. The karst Ni foam was obtained using etching method by applying 0.3 V for 5 min in 0.5 M H<sub>2</sub>SO<sub>4</sub> electrolyte, where pretreated Ni foam, saturated Ag/AgCl, and graphite rod were used as working electrode reference electrode, and counter electrode, respectively, while the karst Ni foam was washed with water and ethanol, and it was stocked in ethanol for consequent usage. The karst Ni foam possesses karst like morphology, which is composed of Ni/α-Ni(OH)<sub>2</sub> heterostructures at the tower (peak) areas and metallic Ni at the valley areas; It contains Ni, O, and S. In the XPS spectrum, the karst Ni foam exhibits peaks for Ni 2p at 852.0 and 855.6 eV, where the binding energy at 852.0 eV is

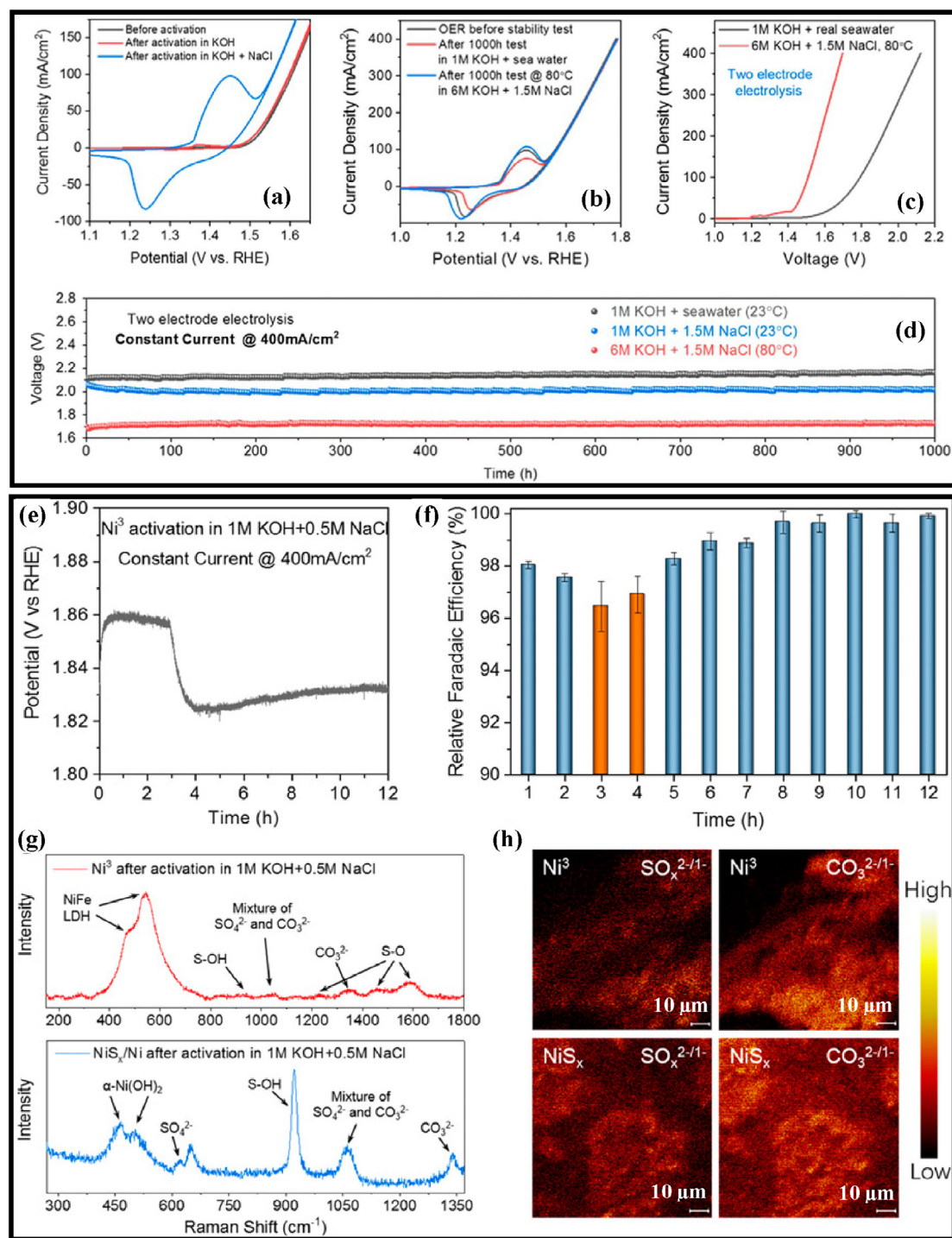


**Fig. 5.** (a) CV scans of an NiFe-NiS<sub>x</sub>-Ni anode recorded before and after activation in 1 M KOH for 12 h and 1 M KOH with 0.5 M NaCl for 12 h; (b) CV scans of an activated NiFe-NiS<sub>x</sub>-Ni anode (activated in KOH for 12 h followed by KOH with NaCl for 12 h) before, and after 1000 h seawater splitting in 1 M KOH with seawater at 23 °C, and after 1000 h seawater splitting in 6 M KOH with 1.5 M NaCl at 80 °C; (c) LSV scans of a NiFe-NiS<sub>x</sub>-Ni<sup>#OER</sup>//Ni-NiO-Cr<sub>2</sub>O<sub>3</sub><sup>HER</sup> electrolyzer (NiFe-NiS<sub>x</sub>-Ni<sup>#OER</sup>; activated NiFe-NiS<sub>x</sub>-Ni anode) in alkaline seawater electrolyte (1 M KOH with real seawater) at 23 °C (Resistance: 0.95 ± 0.05 Ω) and in near-saturated salt concentration under industrial electrolysis conditions (6 M KOH with 1.5 M NaCl electrolyte at 80 °C; Resistance: 0.55 ± 0.05 Ω); (d) Chronopotentiometry response of NiFe-NiS<sub>x</sub>-Ni<sup>#OER</sup>//Ni-NiO-Cr<sub>2</sub>O<sub>3</sub><sup>HER</sup> electrolyzer (NiFe-NiS<sub>x</sub>-Ni<sup>#OER</sup>; Activated NiFe-NiS<sub>x</sub>-Ni anode, where the electrolyte used for activation is varied with respect to the electrolyte used for stability test) recorded for 1000 h at 400 mA cm<sup>-2</sup> in 1 M KOH with real seawater (23 °C; Resistance: 0.95 ± 0.05 Ω), 1 M KOH with 1.5 M NaCl (23 °C; Resistance: 0.8 ± 0.05 Ω), and 6 M KOH with 1.5 M NaCl electrolyte (80 °C; Resistance: 0.55 ± 0.05 Ω), respectively; Investigation of cation selective layer generation during activation process of anode; (e) Chronopotentiometry response of NiFe-NiS<sub>x</sub>-Ni anode during the activation process in 1 M KOH with 0.5 M NaCl (Resistance: 1.4 ± 0.05 Ω; Electrode area: 0.5 cm<sup>2</sup>), where the decrease in voltage is occurred between 3 and 4 h, which could be due to the etching-passivation process (The NiFe-NiS<sub>x</sub>-Ni anode is first activated in 1 M KOH for 12 h before the activation in 1 M KOH with 0.5 M NaCl); (f) Relative Faradaic efficiency plots for the oxygen production during the activation process of anode in 1 M KOH with 0.5 M NaCl; (g) Raman spectra of NiFe-NiS<sub>x</sub>-Ni and NiFe-NiS<sub>x</sub>-Ni after 12 h activation in 1 M KOH with 0.5 M NaCl; (h) TOF-SIMS mapping from a NiFe-NiS<sub>x</sub>-Ni and NiS<sub>x</sub>-Ni electrode surface for SO<sub>x</sub><sup>2-/1-</sup> and CO<sub>3</sub><sup>2-/1-</sup> fragments after activation in 1 M KOH with 0.5 M NaCl; Negative TOF-SIMS counts have been collected from *m/z* = 96/48/80/40 (SO<sub>4</sub><sup>2-</sup>/SO<sub>3</sub><sup>2-</sup>/SO<sub>3</sub><sup>1-</sup>) and 60/30 (CO<sub>3</sub><sup>2-</sup>/CO<sub>3</sub><sup>1-</sup>) after Ar plasma milling for 5 to 15 minutes for cleaning the surface adsorbed electrolytes (Reproduced with permission from Ref. [66]; Copyright 2019, National Academy of Sciences of the United States of America).

slightly lower than the metallic Ni ( $\text{Ni}^0$ ), while the binding energy at 855.6 eV is slightly larger than the  $\text{Ni}(\text{OH})_2$  ( $\text{Ni}^{2+}$ ) suggesting the modified electronic structure, which could be due to the partial transfer of electrons from  $\text{Ni}(\text{OH})_2$  to Ni in the  $\text{Ni}/\alpha\text{-Ni}(\text{OH})_2$  heterostructures; Moreover, the DOS suggests the electron redistribution at the  $\text{Ni}/\alpha\text{-Ni}(\text{OH})_2$  heterostructures; The peak-force scanning electrochemical microscopy investigation suggests that the active sites for OER could be mainly located at tower areas (probably hydroxide), while the active sites for HER could be mainly located at valley areas (metallic Ni). For overall water splitting in natural seawater (pH:  $\sim 8$ ), the karst Ni foam//karst Ni foam electrolyzer exhibits enhanced activity ( $1.79\text{ V}$  at  $10\text{ mA cm}^{-2}$ ) and stability (reasonable stability for  $>9\text{ h}$  at  $10\text{ mA cm}^{-2}$ ). Moreover, the interaction of the ions such as  $\text{Cl}^-$ ,  $\text{Na}^+$ ,  $\text{SO}_4^{2-}$  and  $\text{Mg}^{2+}$  in seawater on the karst Ni foam electrode after electrolysis for 5 h at  $10\text{ mA cm}^{-2}$  was investigated;  $\text{Mg}(\text{OH})_2$  could be formed on the cathode during HER, while the polyatomic sulfate passivating layers could be formed on the anode (karst Ni foam) during OER; The polyatomic sulfate layers on anode could prevent the attack of  $\text{Cl}^-$ , and that could protect the electrode from corrosion.

Preparing nickel nitride and nickel sulfide with distinct interface could accelerate the dissociative adsorption of water molecules, serve as electrochemical active sites and function as bifunctional catalyst, and that could enhance the performance for overall water splitting. Shi-Zhang Qiao's group [89] has observed that NiNS catalyst can be used as bifunctional catalyst for overall water splitting in buffered seawater electrolyte. The NiNS was synthesized by a one-step calcination (at  $550\text{ }^\circ\text{C}$  for 5 h) of nickel foam with thiourea under vacuum atmosphere. They observed that  $\text{NiNS}^{\text{OER}}//\text{NiNS}^{\text{HER}}$  electrolyzer exhibits higher activity than  $\text{Ir-C}^{\text{OER}}//\text{Pt-C}^{\text{HER}}$  for overall water splitting in buffered seawater electrolyte. The NiNS is polycrystalline, and it is composed of  $\text{Ni}_3\text{N}$  and  $\text{Ni}_3\text{S}_2$  phases with distinct interface, which could be beneficial for dissociative adsorption of water molecules; It contains Ni, N and S, which are uniformly distributed; It contains 87.18 wt% of Ni, 4.17 wt% of nitrogen and 8.65 wt% of sulfur, and that possibly enhances its activity for overall water splitting in buffered seawater. For overall water splitting in buffered seawater (pH  $\sim 7.05$ ), the  $\text{NiNS}^{\text{OER}}//\text{NiNS}^{\text{HER}}$  electrolyzer exhibits a cell voltage of  $1.8\text{ V}$  at  $48.3\text{ mA cm}^{-2}$ , which indicates that NiNS catalyst can be used as bifunctional catalyst in buffered seawater electrolyte.

The construction of dual layered anode having top LDH thin layer along with the underneath  $\text{NiS}_x$  thick layer could play a vital role for its long-term stability for OER against chloride corrosion, and the activation of this dual layered anode could form the polyatomic anions intercalated LDH layer along with the underneath sulfate-rich anodized  $\text{NiS}_x$  layer, and that could repel chloride anions and that could inhibit the corrosion against chloride anions when paired with high performance cathode during seawater electrolysis. Xiaoming Sun and Hongjie Dai's group [66] have demonstrated that  $\text{NiFe-NiS}_x\text{-Ni}^{\#\text{OER}}//\text{Ni-NiO-Cr}_2\text{O}_3^{\text{HER}}$  electrolyzer ( $\text{NiFe-NiS}_x\text{-Ni}^{\#\text{OER}}$ : activated  $\text{NiFe-NiS}_x\text{-Ni}$  anode) exhibits substantially much high activity and stability for overall water splitting in alkaline simulated/real seawater electrolyte. The  $\text{NiFe-NiS}_x\text{-Ni}$  anode was prepared by the following steps: At first, the  $\text{NiS}_x\text{-Ni}$  was obtained by solvothermal reaction of annealed Ni foam with elemental sulfur in anhydrous toluene; Finally, the  $\text{NiFe-NiS}_x\text{-Ni}$  was prepared by electrodeposition process at  $10\text{ }^\circ\text{C}$  for 45 min, where the NiFe LDH was grown on the  $\text{NiS}_x\text{-Ni}$  through the reduction of nitrate from a solution of  $\text{Ni}(\text{NO}_3)_2$  and  $\text{Fe}(\text{NO}_3)_3$  with 3:1 ratio of Ni and Fe. The  $\text{Ni-NiO-Cr}_2\text{O}_3$  cathode was obtained by the following steps: At first a product was prepared by the hydrolysis of precursors at  $90\text{ }^\circ\text{C}$ ; Then, the dispersion was obtained by sonication of the product with 30 wt% of 20 nm Ni particles; Finally, the  $\text{Ni-NiO-Cr}_2\text{O}_3$  was prepared by drop-drying the dispersion to coat on Ni foam followed by annealing at  $300\text{ }^\circ\text{C}$ . The  $\text{NiFe-NiS}_x\text{-Ni}$  anode

is composed of amorphous  $\text{NiS}_x$  and NiFe layers, where the Ni foam is surrounded by  $\text{NiS}_x$  layer with about 1 to 2  $\mu\text{m}$  in thickness, while the  $\text{NiS}_x$  layer is surrounded by top NiFe LDH layer with about 200 nm in thickness. Fig. 5a depicts the CV scans of a  $\text{NiFe-NiS}_x\text{-Ni}$  anode recorded before and after activation in 1 M KOH for 12 h and 1 M KOH with 0.5 M NaCl for 12 h, where the huge increase in the oxidation peak ( $\text{Ni}^{2+} \rightarrow \text{Ni}^{3+}$ ) at  $\sim 1.44\text{ V}$  was observed for the anode after activation, and this suggested that the activation process increased the electrochemically active nickel sites of the anode for OER. The activated  $\text{NiFe-NiS}_x\text{-Ni}$  anode exhibits significantly much high OER activity by affording low  $\eta$  of  $\sim 300\text{ mV}$  at  $400\text{ mA cm}^{-2}$  in 1 M KOH with 0.5 M NaCl (Fig. 5b), which is much lower than the  $\eta$  of  $\sim 480\text{ mV}$ , and that could not compete with the formation of hypochlorite; The  $\text{Ni-NiO-Cr}_2\text{O}_3$  cathode exhibits substantially much high HER activity by affording low  $\eta$  of  $\sim 160\text{ mV}$  at  $\sim 500\text{ mA cm}^{-2}$  in 1 M KOH with 0.5 M NaCl. For overall water splitting in alkaline simulated/real seawater electrolyte (Fig. 5c, d, Table 6, and 7), the  $\text{NiFe-NiS}_x\text{-Ni}^{\#\text{OER}}//\text{Ni-NiO-Cr}_2\text{O}_3^{\text{HER}}$  electrolyzer exhibits substantially much high activity ( $\sim 2.02\text{ V}$  at  $400\text{ mA cm}^{-2}$  in 1 M KOH with 1.5 M NaCl;  $\sim 2.06\text{ V}$  at  $400\text{ mA cm}^{-2}$  in 1 M KOH with 0.5 M NaCl;  $\sim 2.09\text{ V}$  at  $400\text{ mA cm}^{-2}$  in 1 M KOH with 1 M NaCl;  $\sim 2.12\text{ V}$  at  $400\text{ mA cm}^{-2}$  in 1 M KOH with seawater;  $\sim 1.72\text{ V}$  at  $400\text{ mA cm}^{-2}$  in 6 M KOH with 1.5 M NaCl at  $80\text{ }^\circ\text{C}$ ), while the  $\text{NiFe-NiS}_x\text{-Ni}^{\#\text{OER}}//\text{Ni-NiO-Cr}_2\text{O}_3^{\text{HER}}$  electrolyzer exhibits significantly much high stability

**Table 6**

Cell voltage and its corresponding current density for overall water splitting of various reported electrocatalysts in real/simulated seawater electrolyte, while the details of the natural seawater are described on the footnote of this Table.

Electrocatalysts	Electrolyte	Cell voltage and its corresponding current density	Refs.
$\text{NiMoN@NiFeN}^{\text{OER}}//\text{NiMoN}^{\text{HER}}$	1 M KOH + 0.5 M NaCl at $60\text{ }^\circ\text{C}$	$\sim 1.44\text{ V}$ at $100\text{ mA cm}^{-2}$	[1]
$\text{NiMoN@NiFeN}^{\text{OER}}//\text{NiMoN}^{\text{HER}}$	1 M KOH + seawater <sup>a†</sup> at $60\text{ }^\circ\text{C}$	$1.454\text{ V}$ at $100\text{ mA cm}^{-2}$	[1]
$\text{NiMoN@NiFeN}^{\text{OER}}//\text{NiMoN}^{\text{HER}}$	6 M KOH + seawater <sup>a†</sup>	$1.491\text{ V}$ at $100\text{ mA cm}^{-2}$	[1]
$\text{Pt/C}^{\text{OER}}//\text{Pt/C}^{\text{HER}}$ (PEM)	Seawater <sup>s†</sup>	$\sim 1.51\text{ V}$ at $10\text{ mA cm}^{-2}$	[93]
$\text{NiFe LDH}^{\text{OER}}//\text{Pt/C}^{\text{HER}}$	0.1 M KOH + 0.5 M NaCl	$\sim 1.56\text{ V}$ at $25\text{ mA cm}^{-2}$	[90]
$\text{NiMoN@NiFeN}^{\text{OER}}//\text{NiMoN}^{\text{HER}}$	1 M KOH + 0.5 M NaCl	$1.564\text{ V}$ at $100\text{ mA cm}^{-2}$	[1]
$\text{NiMoN@NiFeN}^{\text{OER}}//\text{NiMoN}^{\text{HER}}$	1 M KOH + seawater <sup>a†</sup>	$1.581\text{ V}$ at $100\text{ mA cm}^{-2}$	[1]
$\text{NiFe-NiS}_x\text{-Ni}^{\#\text{OER}}//\text{Ni-NiO-Cr}_2\text{O}_3^{\text{HER}}$	6 M KOH + 1.5 M NaCl at $80\text{ }^\circ\text{C}$	$\sim 1.72\text{ V}$ at $400\text{ mA cm}^{-2}$	[66]
karst Ni foam//karst Ni foam	Seawater <sup>a†</sup>	$1.79\text{ V}$ at $10\text{ mA cm}^{-2}$	[88]
$\text{NiNS}^{\text{OER}}//\text{NiNS}^{\text{HER}}$	Seawater <sup>a†</sup> (buffered; pH $\sim 7.05$ )	$1.8\text{ V}$ at $48.3\text{ mA cm}^{-2}$	[89]
$\text{NiFe-NiS}_x\text{-Ni}^{\#\text{OER}}//\text{Ni-NiO-Cr}_2\text{O}_3^{\text{HER}}$	1 M KOH + 1.5 M NaCl	$\sim 2.02\text{ V}$ at $400\text{ mA cm}^{-2}$	[66]
$\text{NiFe-NiS}_x\text{-Ni}^{\#\text{OER}}//\text{Ni-NiO-Cr}_2\text{O}_3^{\text{HER}}$	1 M KOH + 0.5 M NaCl	$\sim 2.06\text{ V}$ at $400\text{ mA cm}^{-2}$	[66]
$\text{NiFe-NiS}_x\text{-Ni}^{\#\text{OER}}//\text{Ni-NiO-Cr}_2\text{O}_3^{\text{HER}}$	1 M KOH + 1 M NaCl	$\sim 2.09\text{ V}$ at $400\text{ mA cm}^{-2}$	[66]
$\text{NiFe-NiS}_x\text{-Ni}^{\#\text{OER}}//\text{Ni-NiO-Cr}_2\text{O}_3^{\text{HER}}$	1 M KOH + seawater <sup>a†</sup>	$\sim 2.12\text{ V}$ at $400\text{ mA cm}^{-2}$	[66]

$\text{NiFe-NiS}_x\text{-Ni}^{\#\text{OER}}$ : Activated  $\text{NiFe-NiS}_x\text{-Ni}$ ; PEM: Proton exchange membrane electrolyzer; Ref.: References; LDH: Layered Double Hydroxides; Seawater<sup>a†</sup>: It is natural seawater (pH =  $\sim 7.2$ ), which is collected from Galveston Bay near Houston, Texas, USA; Seawater<sup>q†</sup>: It is natural seawater (pH:  $\sim 8$ ), which is collected from Yellow Sea in China; Seawater<sup>r†</sup> (buffered; pH  $\sim 7.05$ ): It is natural seawater (the seawater is collected from Glenelg beach at Adelaide in Australia), which is then buffered using phosphate buffer solution to pH of  $\sim 7.05$ ; Seawater<sup>s†</sup>: seawater (Carolina Biological Supply Company, Seawater, 153,783 – Atlantic Ocean water); Seawater<sup>t†</sup>: It is natural seawater, which is collected from San Francisco Bay.

**Table 7**

Stability of various reported electrocatalysts for overall water splitting in real/simulated seawater electrolyte, while the details of the natural seawater are described on the footnote of this Table.

Electrocatalysts	Electrolyte	Chr Amp	Chr Pot	Dur (h)	Remark after stability test	Refs.
NiFe-NiS <sub>x</sub> -Ni <sup>#OER</sup> //Ni-NiO-Cr <sub>2</sub> O <sub>3</sub> <sup>HER</sup>	1 M KOH + seawater <sup>†</sup>	NA	Yes	1000	Negligible decay at 400 mA cm <sup>-2</sup>	[66]
NiFe-NiS <sub>x</sub> -Ni <sup>#OER</sup> //Ni-NiO-Cr <sub>2</sub> O <sub>3</sub> <sup>HER</sup>	6 M KOH + 1.5 M NaCl at 80 °C	NA	Yes	1000	Negligible decay at 400 mA cm <sup>-2</sup>	[66]
NiFe-NiS <sub>x</sub> -Ni <sup>#OER</sup> //Ni-NiO-Cr <sub>2</sub> O <sub>3</sub> <sup>HER</sup>	1 M KOH + 1.5 M NaCl	NA	Yes	1000	Negligible decay at 400 mA cm <sup>-2</sup>	[66]
NiFe-NiS <sub>x</sub> -Ni <sup>#OER</sup> //Ni-NiO-Cr <sub>2</sub> O <sub>3</sub> <sup>HER</sup>	1 M KOH + 1 M NaCl	NA	Yes	1000	Negligible decay at 400 mA cm <sup>-2</sup>	[66]
NiFe-NiS <sub>x</sub> -Ni <sup>#OER</sup> //Ni-NiO-Cr <sub>2</sub> O <sub>3</sub> <sup>HER</sup>	1 M KOH + 2 M NaCl	NA	Yes	~600	Negligible decay up to ~600 h at 400 mA cm <sup>-2</sup> but the stability is completely hampered at ~600 h	[66]
NiMoN@NiFeN <sup>OER</sup> //NiMoN <sup>HER</sup>	6 M KOH + seawater <sup>†</sup>	NA	Yes	600	~21 mV decay at 100 mA cm <sup>-2</sup>	[1]
NiFe-NiS <sub>x</sub> -Ni <sup>#OER</sup> //Ni-NiO-Cr <sub>2</sub> O <sub>3</sub> <sup>HER</sup>	1 M KOH + 0.5 M NaCl	NA	Yes	500	Negligible decay at 1000 mA cm <sup>-2</sup>	[66]
MHCM-z-BCC <sup>OER</sup> //NiMoS <sup>HER</sup>	Seawater <sup>††</sup> (buffered; pH ~ 7)	Yes	NA	100	~90% retention under simulated solar irradiation	[64]
NiFe LDH <sup>OER</sup> //Pt/C <sup>HER</sup>	0.1 M KOH + 0.5 M NaCl	Yes	NA	100	Reasonable stability at 1.6 V	[90]
NiMoN@NiFeN <sup>OER</sup> //NiMoN <sup>HER</sup>	1 M KOH + 0.5 M NaCl	NA	Yes	100	Negligible decay at 100 mA cm <sup>-2</sup>	[1]
NiMoN@NiFeN <sup>OER</sup> //NiMoN <sup>HER</sup>	1 M KOH + seawater <sup>†</sup>	NA	Yes	100	Negligible decay at 100 mA cm <sup>-2</sup>	[1]
Pt/C <sup>OER</sup> //Pt/C <sup>HER(PEM)</sup>	Seawater <sup>†††</sup>	Yes	NA	~50	Obvious decay at 1.6 V	[93]
karst Ni foam//karst Ni foam	Seawater <sup>†††</sup>	NA	YES	>9	Reasonable stability at 10 mA cm <sup>-2</sup>	[88]

Chr Amp: Chronoamperometry; Chr Pot: Chronopotentiometry; Dur: Duration for stability test; Ref.: References; NiFe-NiS<sub>x</sub>-Ni<sup>#</sup>: Activated NiFe-NiS<sub>x</sub>-Ni; PEM: Proton exchange membrane electrolyzer; MHCM: Transition metal hexacyanometallate; z-BCC: ZIF-67 on the basic cobalt carbonate surface; LDH: Layered Double Hydroxides; Seawater<sup>†</sup>: It is natural seawater (pH = ~7.2), which is collected from Galveston Bay near Houston, Texas, USA; Seawater<sup>††</sup>: It is natural seawater (pH: ~8), which is collected from Yellow Sea in China; Seawater<sup>†††</sup>: seawater (Carolina Biological Supply Company, Seawater, 153,783 – Atlantic Ocean water); Seawater<sup>†††</sup>: It is natural seawater, which is collected from San Francisco Bay; Seawater<sup>††††</sup> (buffered; pH ~7): It is natural seawater (the seawater (pH = ~8) is collected from West Coast Park in Singapore), which is then buffered using NaH<sub>2</sub>PO<sub>4</sub>/Na<sub>2</sub>HPO<sub>4</sub> acid/base conjugate pair to pH of 7.

(Negligible decay at 400 mA cm<sup>-2</sup> for 1000 h in 1 M KOH with seawater; Negligible decay at 400 mA cm<sup>-2</sup> for 1000 h in 1 M KOH with 1.5 M NaCl; Negligible decay at 400 mA cm<sup>-2</sup> for 1000 h in 1 M KOH with 1 M NaCl; Negligible decay at much high current density of 1000 mA cm<sup>-2</sup> for 500 h in 1 M KOH with 0.5 M NaCl; Negligible decay at 400 mA cm<sup>-2</sup> for 1000 h in 6 M KOH with 1.5 M NaCl at 80 °C; Negligible decay up to ~600 h at 400 mA cm<sup>-2</sup> but the stability is completely hampered at ~600 h in 1 M KOH with 2 M NaCl (harsh electrolyte)). Thus, the NiFe-NiS<sub>x</sub>-Ni<sup>#OER</sup>//Ni-NiO-Cr<sub>2</sub>O<sub>3</sub><sup>HER</sup> electrolyzer exhibits substantially much high stability in alkaline simulated/real seawater electrolyte, and this suggests the robust stability of the cathode and anode against chloride corrosion; The dual layers of the anode and the subsequent activation could play a vital role for its robust stability against chloride corrosion; Their 3- dimensional (3D) X-ray microtomography studies revealed that the activated NiFe-NiS<sub>x</sub>-Ni anode almost retains its skeleton structure after seawater electrolysis for 1000 h in 1 M KOH with real seawater, while the activated NiFe-NiS<sub>x</sub>-Ni anode almost maintains its skeleton structure after electrolysis for 300 h in 1 M KOH with 2 M NaCl (harsh electrolyte), whereas the activated NiFe-Ni anode (anode without NiS<sub>x</sub> layer and with only NiFe layer) almost deteriorates its skeleton structure (possibly due to the severe corrosion) after electrolysis for only 8 h in 1 M KOH with 2 M NaCl (harsh electrolyte); Thus, the top NiFe LDH thin layer as well as the underneath NiS<sub>x</sub> thick layer of the NiFe-NiS<sub>x</sub>-Ni anode and the subsequent activation could play a significant role for its long-term stability against chloride corrosion. Moreover, the activation of NiFe-NiS<sub>x</sub>-Ni anode could lead to the transient etching followed by the formation of polyatomic anion passivated layers and that could repel chloride anions and that could inhibit the corrosion against chloride anions; The Raman spectrum of the activated NiFe-NiS<sub>x</sub>-Ni anode exhibits vibrational modes at about 470 cm<sup>-1</sup> and 540 cm<sup>-1</sup> suggesting the existence of NiFe LDH, while it exhibits peaks around 1230 cm<sup>-1</sup>, 1440 cm<sup>-1</sup>, and

1590 cm<sup>-1</sup>, and those could be ascribed to S–O vibration (Fig. 5g); This result suggested that sulfides could be oxidized due to the etching of the NiFe-NiS<sub>x</sub>-Ni anode during the activation process, while the decrease in voltage with variation in relative Faradaic efficiency are observed between 3 and 4 h (Fig. 5e and f), which could be due to the etching-passivation process; In the activation process, the sulfate and carbonate ions could be intercalated into NiFe LDH, where the sulfate ions could be formed due to the anodic etching of the NiS<sub>x</sub> layer, while the carbonate ions could exist from electrolyte; Their Time-of-Flight Secondary Ion Mass Spectrometry (TOF-SIMS) mapping disclose the existence of sulfate and carbonate species on the activated NiFe-NiS<sub>x</sub>-Ni anode suggesting the formation of NiFe LDH intercalated with two kinds of polyanions (Fig. 5h); In addition, the activated NiFe-NiS<sub>x</sub>-Ni anode exhibits negligible decay for >500 h but activated NiS<sub>x</sub>-Ni anode exhibits severe decay with <1 h when paired with Ni-NiO-Cr<sub>2</sub>O<sub>3</sub> cathode at 400 mA cm<sup>-2</sup> in 1 M KOH with 2 M NaCl electrolyte suggesting the substantially much high stability of the activated NiFe-NiS<sub>x</sub>-Ni anode and poor stability of the activated NiS<sub>x</sub>-Ni anode, while the existence of the LDH (α-Ni(OH)<sub>2</sub>), sulfate ions and carbonate ions are observed in the activated NiS<sub>x</sub>-Ni anode (Fig. 5g and h); Thus, for the activated NiFe-NiS<sub>x</sub>-Ni anode, the sulfate and carbonate ions co-intercalated NiFe LDH layer along with the underneath sulfate-rich anodized NiS<sub>x</sub> layer could be responsible for the high corrosion resistance against chloride anions together with high OER activity during seawater electrolysis.

The fabrication of metal nitride anode with core-shell structure having NiFeN as shell could *in situ* form the OER active thin amorphous layers of NiFe oxide and NiFe oxy(hydroxide) during OER, where the *in situ* formed OER active layers could also enhance the corrosion resistance against chloride anions in seawater, while the core-shell structured anode could also tune the electronic structure, enhance the charge transfer process, expose abundant active sites, and facilitate gas evolution, and those could enhance

the OER performance in sea water; The core-shell structured metal nitride anode in combination with nano array cathode could enhance the activity and stability for overall water splitting in seawater electrolyte. Ying Yu, Shuo Chen and Zhifeng Ren's group [1] have observed that NiMoN@NiFeN<sup>OER</sup>//NiMoN<sup>HER</sup> electrolyzer exhibits substantially much high activity and stability for overall water splitting in alkaline simulated/real seawater electrolyte. The NiMoN cathode was prepared by the following steps: At first, the NiMoO<sub>4</sub> was obtained by hydrothermal treatment of Ni foam at 150 °C for 6 h; Finally, NiMoN was synthesized by thermal nitridation of NiMoO<sub>4</sub> at 500 °C for 1 h under NH<sub>3</sub> and Ar atmosphere. The NiMoN@NiFeN anode was prepared by the following steps: At first, the NiMoO<sub>4</sub> was obtained by hydrothermal treatment of Ni foam at 150 °C for 6 h; Later, NiFe precursor coated NiMoO<sub>4</sub> was prepared by soaking the NiMoO<sub>4</sub> in NiFe precursor ink followed by drying under ambient condition; Finally, NiMoN@NiFeN was obtained by thermal nitridation of NiFe precursor coated NiMoO<sub>4</sub> at 500 °C for 1 h under NH<sub>3</sub> and Ar atmosphere. The NiMoN is crystalline; It possesses nano-rod array morphology, and that could expose abundant active sites; It contains Mo<sup>3+</sup> and Mo<sup>6+</sup>, where the Mo 3d at 229.6 eV is attributed to the Mo<sup>3+</sup> in the metal nitride, and that could be considered as active for HER, and that possibly enhances its significantly much high activity and stability for HER. The NiMoN@NiFeN is crystalline; It possesses core-shell structure, where the core NiMoN nano-rods are surrounded by mesoporous NiFeN shell with ~100 nm in thickness, and that could expose abundant active sites; It contains Mo<sup>3+</sup> and Mo<sup>6+</sup>, where the binding energies of the Mo 3d are negatively shifted when compared to that of NiMoN suggesting the strong electronic interactions between NiMoN and NiFeN, and that possibly enhances its significantly much high activity and stability for OER. For overall water splitting in alkaline simulated/real seawater electrolyte, NiMoN@NiFeN<sup>OER</sup>//NiMoN<sup>HER</sup> electrolyzer (Fig. 6a) exhibits substantially much high activity (Fig. 6b; 1.581 V at 100 mA cm<sup>-2</sup> in 1 M KOH with seawater; 1.564 V at 100 mA cm<sup>-2</sup> in 1 M KOH with 0.5 M NaCl; 1.491 V at 100 mA cm<sup>-2</sup> in 6 M KOH with seawater; 1.454 V at 100 mA cm<sup>-2</sup> in 1 M KOH with seawater at 60 °C; ~1.44 V at 100 mA cm<sup>-2</sup> in 1 M KOH with 0.5 M NaCl at 60 °C), while it exhibits significantly much high stability (Fig. 6d; Negligible decay at 100 mA cm<sup>-2</sup> for 100 h in 1 M KOH with seawater; Negligible decay at 100 mA cm<sup>-2</sup> for 100 h in 1 M KOH with 0.5 M NaCl; ~21 mV decay at 100 mA cm<sup>-2</sup> for 600 h in 6 M KOH with seawater). Moreover, using NiMoN@NiFeN<sup>OER</sup>//NiMoN<sup>HER</sup> electrolyzer in 1 M KOH with 0.5 M NaCl, only H<sub>2</sub> and O<sub>2</sub> gases have been detected with a molar ratio near to 2:1 (Fig. 6c), while ~97.8% of Faradaic efficiency is observed during seawater electrolysis, suggesting the high selectivity for OER on the anode. In addition, they have demonstrated the harvesting of waste heat using seawater electrolyzer, where the waste heat is the major energy loss in different activities and device operations, and the electrolyzer has been powered with a commercial thermoelectric (TE) device, where the TE device (Fig. 6e) directly produce electricity from heat; As depicted in Fig. 6f, the electrolyzer in 1 M KOH with 0.5 M NaCl can be effectively driven by TE device, and the electrolyzer can constantly deliver a current density of around 30, 100, and 200 mA cm<sup>-2</sup>, when the temperature gradient between the hot and cold sides of the TE module has been 40, 50, and 60 °C, respectively. Moreover, the electrolyzer can still constantly deliver a current density of ~30 mA cm<sup>-2</sup>, when the temperature gradient through the TE module has been diminished to 40 °C, suggesting the effective production of hydrogen from waste heat by seawater electrolysis. In addition, they have investigated the changes on NiMoN@NiFeN anode after seawater electrolysis in 1 M KOH with seawater, where the 1 M KOH with seawater electrolyte is turbid after electrolysis, while the white insoluble precipitates on the surface of the anode is observed after electrolysis,

which could be due to the formation of Mg(OH)<sub>2</sub> and Ca(OH)<sub>2</sub> on the surface of the anode, and those could slightly decrease the activity possibly due to the blocking of some active sites. Moreover, they performed the material characterization to identify the OER active sites of NiMoN@NiFeN anode; The TEM image of NiMoN@NiFeN (Fig. 6g) depicts that it retains its 3D core-shell nanostructure after OER suggesting its structural stability; In addition, the TEM image of NiMoN@NiFeN (Fig. 6h) suggested the formation of thin layers on the NiFeN shell; Moreover, the HRTEM image (Fig. 6i) discloses the presence of thin amorphous layers and Ni(OH)<sub>2</sub>; The elemental mapping (Fig. 6j) and XPS spectra (Fig. 6k and l) suggested that the thin layers formed on the NiMoN@NiFeN after OER could be the *in situ* formed NiFe oxides and NiFe oxy(hydroxides); Dark field scanning transmission electron microscopy (DF-STEM) image and corresponding elemental mapping images (Fig. 6j) depict the almost disappearance of N and increased O content on the NiMoN@NiFeN surface after OER, which could be due to the intense oxidation process; The high-resolution XPS spectra of N 1s obtained on NiMoN@NiFeN before and after OER revealed that the N content on the catalyst surface was diminished from 10.3% to 0.36% after OER, which is corroborate with the above DF-STEM investigation; The high-resolution XPS spectra of Ni 2p (Fig. 6k) on NiMoN@NiFeN show the absence of the two peaks ascribed to Ni-N species at 853.4 and 870.8 eV after OER, which could be due to the surface oxidation, while a new peak at 868.9 eV is appeared, which is attributed to Ni(OH)<sub>2</sub>; Moreover, the two peaks at 856.3 (Ni-O) and 862.0 eV (Sat.) are positively shifted toward higher binding energy for NiMoN@NiFeN after OER, while the Fe 2p and satellite peaks are also positively shifted toward higher binding energy for NiMoN@NiFeN after OER, and those suggest that the NiFe oxides/oxy (hydroxides) could be formed after OER on NiMoN@NiFeN due to the oxidation of Ni<sup>2+</sup> and Fe<sup>2+</sup> to the higher valence states of Ni<sup>3+</sup> and Fe<sup>3+</sup>, respectively; In addition, the O 1s XPS spectra on NiMoN@NiFeN show the negative shift for the main peaks at 531.9 and 530.1 eV, which further suggest the increased valence states of Ni<sup>2+</sup> and Fe<sup>2+</sup> after OER, while a new peak at 532.3 eV is appeared after OER, which suggest the formation of Fe-OH from the NiFe oxy (hydroxides); They have performed *in situ* Raman measurements (Fig. 6m) to disclose the real-time evolution of the NiMoN@NiFeN catalyst during the OER process; A sharp and broad peak at around 80.3 cm<sup>-1</sup> is observed for the as-prepared NiMoN@NiFeN, which could be attributed to the metal-N stretching modes; When the potential reaches to 1.4 V, a new Raman band located at 480.1 cm<sup>-1</sup> is observed, which could be due to the formation of NiOOH; When the potential reaches to 1.6 and 1.7 V, two additional Raman bands at 324.7 cm<sup>-1</sup> and 693.1 cm<sup>-1</sup> are observed, and those could be ascribed to the Fe-O vibrations in Fe<sub>2</sub>O<sub>3</sub> and Fe-O vibrations in amorphous FeOOH, respectively; Thus, the DF-STEM, XPS, and *in situ* Raman investigations suggest the *in situ* formation of thin amorphous layers of NiFe oxide and NiFe oxy(hydroxide) as active sites on the NiFeN shell of the NiMoN@NiFeN anode during OER, where the NiMoN core could transfer the electrons to the NiFeN shell, and the NiFeN shell could migrate the electrons to the *in situ* formation of thin amorphous layers, and that could boost the OER performance; Moreover, such *in situ* generated amorphous NiFe oxide and NiFe oxy(hydroxide) layers on NiMoN@NiFeN anode after OER could also improve the corrosion resistance by chloride anions in seawater; The NiMoN@NiFeN before and after OER samples are immersed in seawater for 1 day, and the optical images are recorded before and after immersion, where the post-OER NiMoN@NiFeN sample retains its structural integrity after 1 day immersion in seawater whereas the fresh NiMoN@NiFeN sample shows apparent corrosion after 1 day immersion in seawater, and these suggest that the *in situ* generated amorphous NiFe oxide and NiFe oxy(hydroxide) layers on NiMoN@NiFeN anode

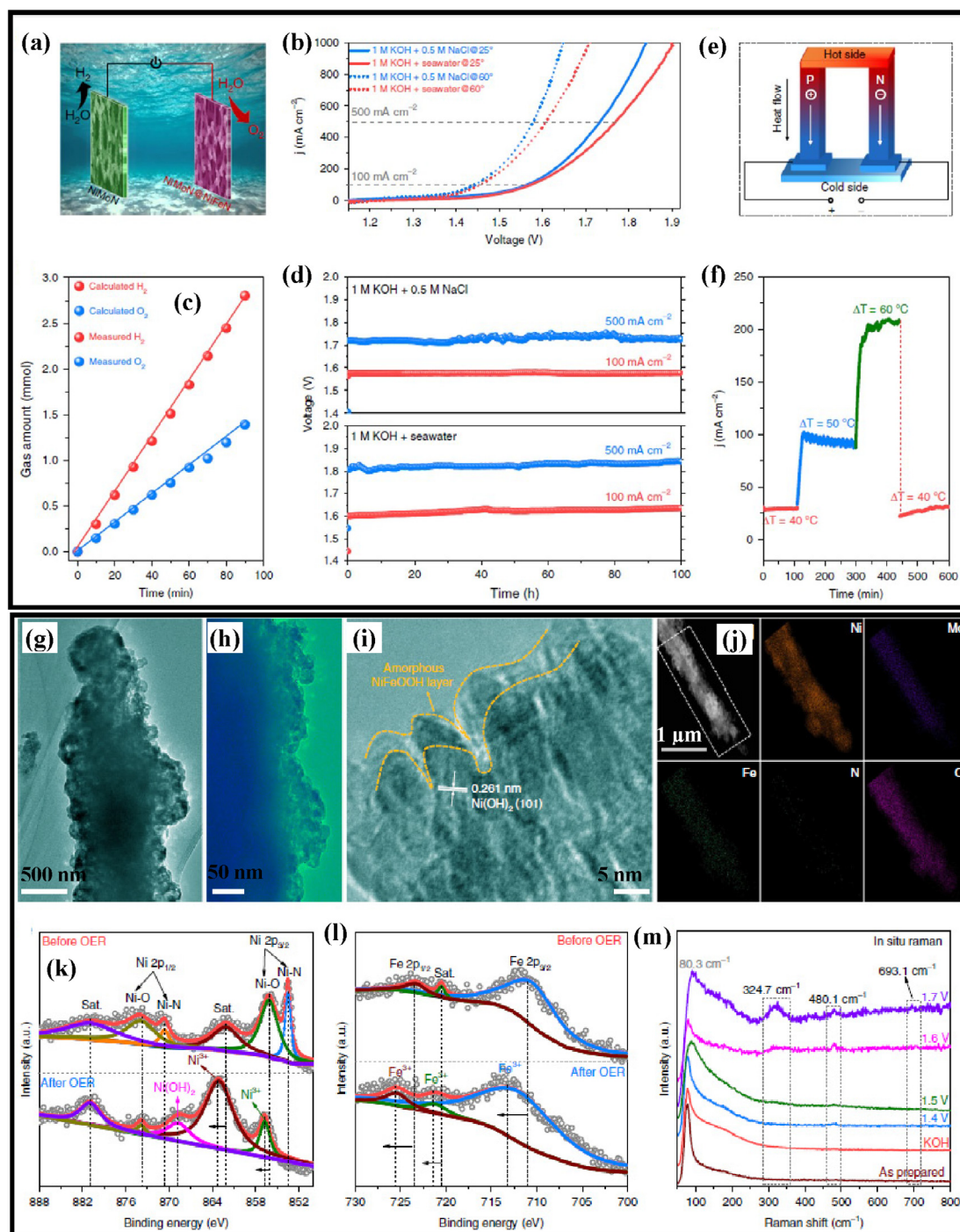


**Fig. 6.** Overall seawater splitting performance of NiMoN@NiFeN<sup>OER</sup>//NiMoN<sup>HER</sup> electrolyzer: (a) Schematic diagram depicts the overall seawater splitting electrolyzer with NiMoN as cathode and NiMoN@NiFeN as anode; (b) iR corrected LSV curves of NiMoN@NiFeN<sup>OER</sup>//NiMoN<sup>HER</sup> electrolyzer obtained in 1 M KOH with 0.5 M NaCl (Resistance: ~1.1 Ω) and 1 M KOH with seawater (Resistance: ~1.2 Ω) electrolytes at 25 °C and 60 °C; (c) Comparison between the amount of theoretical and collected gaseous products (O<sub>2</sub> and H<sub>2</sub>) of the NiMoN@NiFeN<sup>OER</sup>//NiMoN<sup>HER</sup> electrolyzer at 100 mA cm<sup>-2</sup> in 1 M KOH with 0.5 M NaCl at 25 °C; (d) Chronopotentiometry response of NiMoN@NiFeN<sup>OER</sup>//NiMoN<sup>HER</sup> electrolyzer at 100 and 500 mA cm<sup>-2</sup> in 1 M KOH with 0.5 M NaCl and 1 M KOH with seawater at 25 °C; (e) Schematic diagram illustrate the principle for power generation between the hot and cold sides of a thermoelectric device; (f) Real-time dynamics of current densities for the NiMoN@NiFeN<sup>OER</sup>//NiMoN<sup>HER</sup> electrolyzer in 1 M KOH with 0.5 M NaCl at 25 °C driven by a thermoelectric device when the temperature gradient (ΔT) between its hot and cold sides is 40, 50, 60, and 40 °C; Material characterization of NiMoN@NiFeN to identify the active sites for OER: (g, h) TEM images at different magnifications of NiMoN@NiFeN core-shell nanorods after OER; (i) HRTEM image, and (j) DF-STEM image with corresponding elemental mapping of the NiMoN@NiFeN after OER; High resolution XPS spectra of (k) Ni 2p and (l) Fe 2p of NiMoN@NiFeN recorded before and after OER; (m) *in situ* Raman spectra of the NiMoN@NiFeN with (at various potentials) and without OER (Reproduced with permission from Ref. [1]; Copyright 2019, Nature Publishing Group).

after OER could enhance the corrosion resistance by chloride anions in seawater.

Fabrication of MHCM-based catalysts (MHCM: Transition metal hexacyanometallate) could be selective for OER rather than CIER

for seawater electrolysis, whereas the poor conductivity of MHCM-based catalysts could hamper their OER performance; Therefore, constructing core-shell nanostructure with highly OER selective MHCM as shell and conductive basic cobalt carbonate

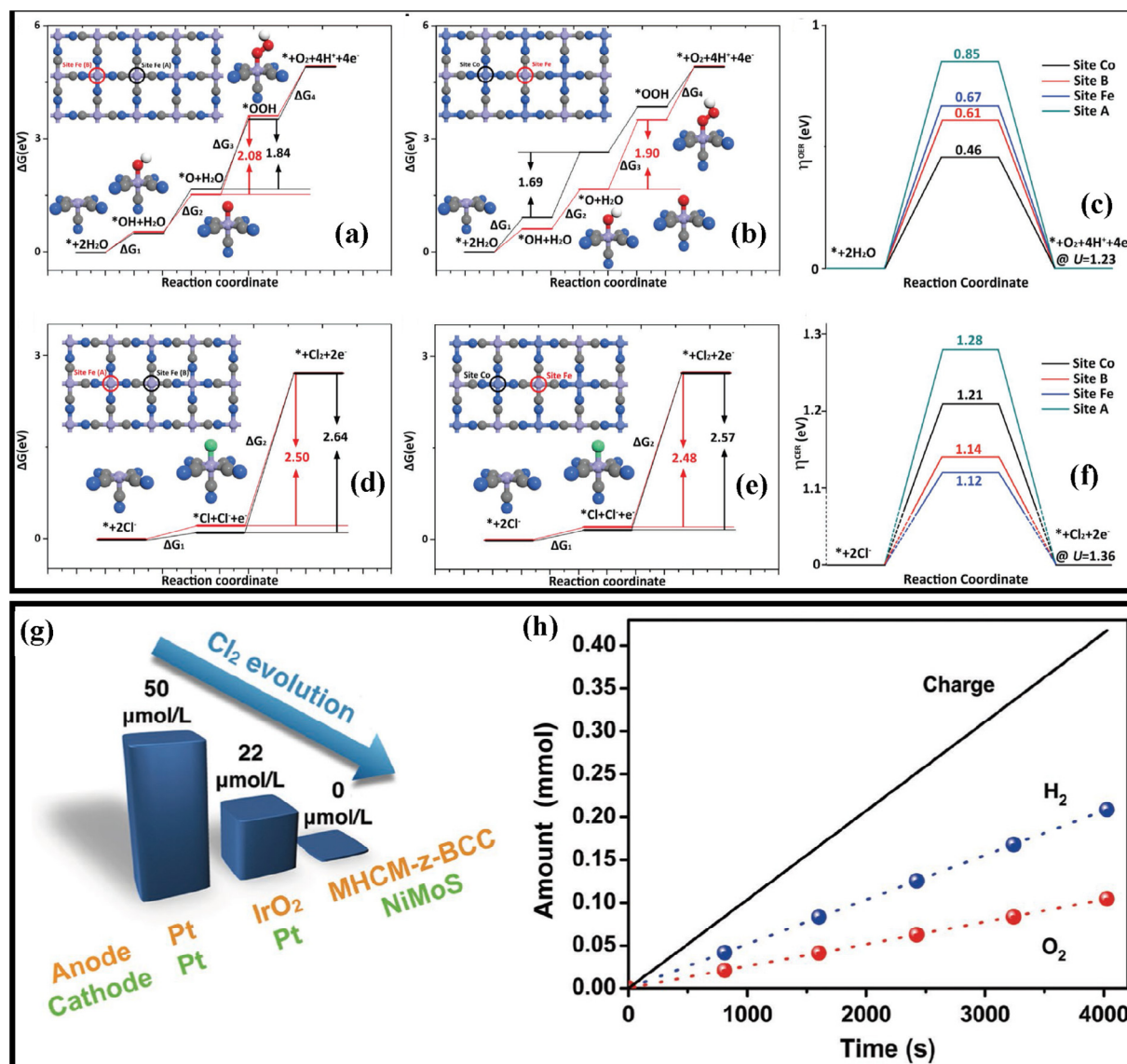


**Fig. 7.** (a–f) DFT calculation results for OER and ClER on metal hexacyanometallates: Schematic diagram depicts the Gibbs free energy changes through four elementary steps during the OER catalyzed by (a)  $\text{Fe}_4[\text{Fe}(\text{CN})_6]_3$  and (b)  $\text{Co}_2[\text{Fe}(\text{CN})_6]$ ; Schematic diagram depicts the Gibbs free energy changes through two elementary steps during the ClER catalyzed by (d)  $\text{Fe}_4[\text{Fe}(\text{CN})_6]_3$  and (e)  $\text{Co}_2[\text{Fe}(\text{CN})_6]$ ; The Gibbs energy diagrams of (c) OER and (f) ClER catalyzed by  $\text{Fe}_4[\text{Fe}(\text{CN})_6]_3$  and  $\text{Co}_2[\text{Fe}(\text{CN})_6]$  on different reaction sites; (g) The estimated amounts of  $\text{Cl}_2$  produced based on the o-tolidine method during the continuous electrolysis of MHCM-z-BCC<sup>OER</sup>/NiMoS<sup>HER</sup> (for 100 h), IrO<sub>2</sub><sup>OER</sup>/Pt<sup>HER</sup> (for 12 h), and Pt<sup>OER</sup>/Pt<sup>HER</sup> (for 12 h) at constant current density of 10 mA cm<sup>-2</sup> in neutral buffered seawater electrolyte; (h) Comparison between the amount of gaseous products collected and the recorded charges passed through the MHCM-z-BCC<sup>OER</sup>/NiMoS<sup>HER</sup> during seawater electrolysis (Red spheres: Amount of experimentally collected O<sub>2</sub>; Blue spheres: Amount of experimentally collected H<sub>2</sub>; Dotted lines: Theoretical amount of evolved gaseous products, which are calculated based on Faraday's law) (Reproduced with permission from Ref. [64]; Copyright 2018, Wiley-VCH Verlag GmbH & Co. KGaA, Weinheim).

as core could expose abundant active sites, enhance charge transfer process, and facilitate the gas evolution, and that could enhance the water oxidation performance. Shi Zhang Qiao and Bin Liu's group [64] have observed that MHCM-z-BCC<sup>OER</sup>/NiMoS<sup>HER</sup> electrolyzer exhibits high stability for overall water splitting in seawater electrolyte (MHCM: Transition metal hexacyanometalate; z-BCC: ZIF-67 on the basic cobalt carbonate surface). The NiMoS cathode was synthesized on pretreated carbon fiber cloth through a one-step biomolecule-assisted hydrothermal synthesis at 200 °C for 24 h, where L-cysteine has been used as the reducing agent and S source, while Na<sub>2</sub>MoO<sub>4</sub>·2H<sub>2</sub>O and NiSO<sub>4</sub>·6H<sub>2</sub>O had been used as Mo and Ni sources, respectively. The MHCM-z-BCC anode was prepared by the following steps: At first, pretreated carbon fiber cloth was obtained by oxygen plasma treatment (air; 500 mTorr) of carbon fiber cloth followed by immersion in piranha

solution (3:1 (v/v) ratio of H<sub>2</sub>SO<sub>4</sub> and H<sub>2</sub>O<sub>2</sub>) for 4 h at 85 °C, which could enhance the surface hydrophilicity; Later, BCC had been grown on pretreated carbon fiber cloth through a facile chemical bath deposition at 90 °C for 6 h; Then, z-BCC was prepared by soaking BCC into the solution containing 2-methylimidazole and cetyl trimethylammonium bromide for 30 min; Finally, MHCM-z-BCC was obtained by dipping z-BCC into the solution containing Ni<sub>4</sub>-Fe(CN)<sub>6</sub> and HOC(COONa)(CH<sub>2</sub>COONa)<sub>2</sub> for 4 h. The NiMoS cathode is composed of Ni-doped MoS<sub>x</sub>, and that could tune the electronic structure, and facilitate the charge transfer process, and that could enhance the HER performance. To better understand the reaction mechanisms, they have conducted DFT calculations to investigate the OER and ClER processes catalyzed by Prussian blue (PB) and its analog  $\text{Co}_2[\text{Fe}(\text{CN})_6]$  as the model MHCM catalysts (Fig. 7a–f); A well-known four-step mechanism has been employed to

determine the OER kinetics (Fig. 7a–c); Thermodynamic investigation suggested that the rate-determining step (RDS) for OER is the \*OOH intermediate formation on both Fe centers (Sites A and B) in pristine PB, and that cause a theoretical overpotential ( $\eta^{\text{OER}}$ ) of 0.61 to 0.85 V, whereas generation of metal–oxo intermediate turns out to be the rate-determining step for OER catalyzed by the Co centers in  $\text{Co}_2[\text{Fe}(\text{CN})_6]$ , and that cause the obviously diminished  $\eta^{\text{OER}}$  of 0.46 to 0.67 V; The four-step OER processes catalyzed by Pt (1 1 1) and  $\text{IrO}_2$  (1 1 0) have been investigated for comparison purpose, and their theoretical overpotentials have been calculated to be 0.37 and 0.64 V, respectively; Moreover, the CIER processes on the four catalysts have been investigated using the two-step Volmer–Heyrovsky mechanisms, and that proceed through  $\text{Cl}^-$  ions adsorption followed by the molecular  $\text{Cl}_2$  release; The RDS for CIER was the Heyrovsky reaction on all investigated model systems; The theoretical  $\eta^{\text{CIER}}$  for Pt and  $\text{IrO}_2$  are 0.19 and 0.34 V, respectively, and those have been lower compared to their corresponding  $\eta^{\text{OER}}$ , whereas the calculated  $\eta^{\text{CIER}}$  ranges from 1.12 to 1.28 V for both PB and its Co/Fe analog on different metal centers, and those have been obviously higher than that of  $\eta^{\text{OER}}$ ; The DFT studies suggested that in contrast to precious metal-based catalysts, the OER will be a more favored anodic process when compared to the CIER on the surface of PB and its analog; The computational studies shine light for the MHCM-based catalysts as highly selective potential OER electrocatalysts for seawater electrolysis, whereas the poor conductivity of MHCM-based catalysts could limit their OER performance; Therefore, constructing core-shell nanostructure with highly OER selective MHCM as shell and conductive basic cobalt carbonate as core could enhance the water oxidation performance. The MHCM-z-BCC anode possesses core-shell structure, where the crystalline basic cobalt carbonate (BCC) nano-needles as core was surrounded by a 20 nm thick transition metal hexacyanometallate (MHCM) shell; It contains Co, Fe, O, N, and C, where the Co and O are predominantly observed on the core, while the Fe, N, and C are predominantly observed on the shell, and the characteristic peak at  $2100\text{--}2200\text{ cm}^{-1}$  is observed from the Fourier transform infrared spectrum of MHCM-z-BCC suggesting the existence of CN-ligands possibly in the MHCM shell; The core BCC could enhance the charge transfer process, and the MHCM shell could afford active sites, while the nanostructure could expose abundant active sites and facilitate the gas evolution, and that could enhance the OER performance. For overall water splitting in seawater (buffered; pH ~7), MHCM-z-BCC<sup>OER</sup>//NiMoS<sup>HER</sup> electrolyzer exhibits ~90% retention under simulated solar irradiation for 100 h, which indicates its much high stability. To investigate the OER selectivity of the MHCM-z-BCC anode, the gaseous products have been collected over the anode during the electrolysis of MHCM-z-BCC<sup>OER</sup>//NiMoS<sup>HER</sup> electrolyzer at constant current, and the composition of the collected gaseous products have been analyzed using gas chromatography, which disclose that only  $\text{O}_2$  is detectable gas-phase products produced from the anode, while  $\text{Cl}_2$  is not detectable suggesting the OER selectivity of the MHCM-z-BCC anode; To further evaluate the presence of free chlorine in the electrolyte during long-term seawater electrolysis, o-tolidine tests have been conducted from the MHCM-z-BCC<sup>OER</sup>//NiMoS<sup>HER</sup>,  $\text{IrO}_2^{\text{OER}}/\text{Pt}^{\text{HER}}$ , and  $\text{Pt}^{\text{OER}}/\text{Pt}^{\text{HER}}$  electrolyzers, where the electrolyzers are operated at constant current density of  $10\text{ mA cm}^{-2}$  in neutral buffered seawater electrolyte; 50 and  $22\text{ }\mu\text{mol L}^{-1}$  of  $\text{Cl}_2$  have been determined from the  $\text{Pt}^{\text{OER}}/\text{Pt}^{\text{HER}}$ , and  $\text{IrO}_2^{\text{OER}}/\text{Pt}^{\text{HER}}$  electrolyzers, respectively after 12 h of continuous operation, whereas MHCM-z-BCC<sup>OER</sup>//NiMoS<sup>HER</sup> electrolyzer has not produced any traceable amount of  $\text{Cl}_2$  even after 100 h of continuous electrolysis (Fig. 7g); Moreover, the o-tolidine tests have been conducted for the three electrolyzers, where the electrolyzers are operated under constant applied voltage of 2.5 V, and they exhibited the similar trends; Faradaic efficiency of the

MHCM-z-BCC<sup>OER</sup>//NiMoS<sup>HER</sup> in buffered seawater has been determined through concurrently collecting the liberated  $\text{H}_2$  and  $\text{O}_2$  gaseous products over the cathode and anode, respectively, while both MHCM-z-BCC and NiMoS electrodes exhibit almost 100% Faradaic efficiency with a 2: 1 stoichiometric ratio of  $\text{H}_2$  and  $\text{O}_2$  (Fig. 7h); These results have been corroborated with the computational predictions, and that further confirmed the superior OER selectivity of the MHCM-z-BCC electrode in buffered seawater.

The fabrication of karst Ni foam could produce heterostructures, and modify the electronic structure, while it could *in situ* generate the polyatomic sulfate passivating layers during OER on anode, and that could enhance the activity and stability for overall water splitting in seawater. Thus, the karst Ni foam//karst Ni foam exhibits enhanced activity and stability for overall water splitting in seawater electrolyte [88]. Preparing nickel nitride and nickel sulfide with distinct interface could accelerate the dissociative adsorption of water molecules, serve as electrochemical active sites and function as bifunctional catalyst, and that could enhance the performance for overall water splitting. Thus, the NiNS catalyst can be used as bifunctional catalyst for overall water splitting in buffered seawater electrolyte [89]. The construction of dual layered anode having top LDH thin layer along with the underneath  $\text{NiS}_x$  thick layer could play a vital role for its long-term stability for OER against chloride corrosion, and the activation of this dual layered anode could form the polyatomic anions intercalated LDH layer along with the underneath sulfate-rich anodized  $\text{NiS}_x$  layer, and that could repel chloride anions and that could inhibit the corrosion against chloride anions when paired with high performance cathode during seawater electrolysis. Thus, the  $\text{NiFe-NiS}_x\text{-Ni}^{\#\text{OER}}/\text{Ni-NiO-Cr}_2\text{O}_3^{\text{HER}}$  electrolyzer ( $\text{NiFe-NiS}_x\text{-Ni}^{\#\text{OER}}$ : activated  $\text{NiFe-NiS}_x\text{-Ni}$  anode) exhibits substantially much high activity and stability for overall water splitting in alkaline simulated/real seawater electrolyte [66]. The fabrication of metal nitride anode with core-shell structure having NiFeN as shell could *in situ* form the OER active thin amorphous layers of NiFe oxide and NiFe oxy(hydroxide) during OER, where the *in situ* formed OER active layers could also enhance the corrosion resistance against chloride anions in seawater, while the core-shell structured anode could also tune the electronic structure, enhance the charge transfer process, expose abundant active sites, and facilitate gas evolution, and those could enhance the OER performance in sea water; The core-shell structured metal nitride anode in combination with nano array cathode could enhance the activity and stability for overall water splitting in seawater electrolyte. Thus, the  $\text{NiMoN@NiFeN}^{\text{OER}}/\text{NiMoN}^{\text{HER}}$  electrolyzer exhibits substantially much high activity and stability for overall water splitting in alkaline simulated/real seawater electrolyte [1]. Fabrication of MHCM-based catalysts (MHCM: Transition metal hexacyanometallate) could be selective for OER rather than CIER for seawater electrolysis, whereas the poor conductivity of MHCM-based catalysts could hamper their OER performance; Therefore, constructing core-shell nanostructure with highly OER selective MHCM as shell and conductive basic cobalt carbonate as core could expose abundant active sites, enhance charge transfer process, and facilitate the gas evolution, and that could enhance the water oxidation performance. Thus, the MHCM-z-BCC<sup>OER</sup>//NiMoS<sup>HER</sup> electrolyzer exhibits high stability for overall water splitting in seawater electrolyte (z-BCC: ZIF-67 on the basic cobalt carbonate surface) [64].

#### 4.2. Noble metal containing electrocatalysts for overall water splitting in sea water

Fabricating nanostructured NiFe LDH anode could modify the electronic structure, expose abundant active sites, enhance charge transfer process, and facilitate the gas evolution, and that could enhance the performance for OER; Therefore, constructing an

electrolyzer with OER active NiFe LDH as anode and Pt/C as cathode could enhance the performance for overall water splitting in simulated seawater electrolyte. Holger Dau and Peter Strasser's group [90] have observed that NiFe LDH<sup>OER</sup>//Pt/C<sup>HER</sup> electrolyzer exhibits considerably much high activity and stability for overall water splitting in alkaline simulated seawater electrolyte. The Pt/C cathode is composed of 46.7 wt% of Pt on Vulcan, while the NiFe LDH anode was obtained by a one-pot microwave-assisted solvothermal synthesis at 120 °C for 60 min followed by 160 °C for 30 min. The NiFe LDH anode possesses 3:1 atomic ratio of Ni and Fe; The XRD pattern of NiFe LDH is almost similar to hydroxalite with slightly higher interlayer distances; It exhibits the rhombohedral crystal structure of NiFe-layered double hydroxide having prismatic P3-R3 oxygen stacking (ABBCA); It possesses layered structure with layers comprising of Ni(II)O<sub>6</sub> and Fe(III)O<sub>6</sub> edge connected octahedrons, while the positive charge of the layers has been balanced by intercalated anions between the layers, deprotonated μ-oxo-bridges or other defects from an ideal crystal structure comprising boundary effects such as terminal coordinated hydroxides; The crystallite size of X<sub>S003</sub> is equal to 6 ± 1 nm by determining the (003) reflection peak using Scherrer equation, while the unit cell interlayer distance of *d*<sub>003</sub> is equal to 7.76 Å, and the metal – metal distance of *d*<sub>110</sub> is equal to 3.11 Å, and that has been corroborated with the metal – metal distance of the NiFe LDH reported in literature; Their TEM investigation revealed that the NiFe LDH possesses sheet structure, while it depicts very thin flakes, which appear to agglomerate in large bulk structures; Thus, it possesses active sites, and that could enhance its performance for OER. For overall water splitting in alkaline simulated seawater electrolyte, NiFe LDH<sup>OER</sup>//Pt/C<sup>HER</sup> electrolyzer exhibits substantially much high activity (~1.56 V at 25 mA cm<sup>-2</sup> in 0.1 M KOH with 0.5 M NaCl), while it exhibits significantly much high stability (Reasonable stability at 1.6 V for 100 h in 0.1 M KOH with 0.5 M NaCl). Moreover, chronoamperometric response of NiFe LDH<sup>OER</sup>//Pt/C<sup>HER</sup> electrolyzer at 1.6 V for >100 h in different KOH concentrations with and without 0.5 M NaCl have been recorded, where ~100 h of continuous electrolysis followed by ~10 min first break followed by ~1 h of electrolysis followed by ~1 h of second break followed by ~1 h of electrolysis are performed to investigate the recovery effect of the electrolyzer (Fig. 8a); The NiFe LDH<sup>OER</sup>//Pt/C<sup>HER</sup> electrolyzer exhibits a variation in operation due to the intermittent break during long-term electrolysis; The bar diagram provides the current density (*j*@1.6 V) of initial, while the bar diagram also depicts the percentage relative to the maximum initial current density (*j*<sub>final</sub>) of 50 h, 100 h, initial first recovery, after 1 h of first recovery, initial second recovery, and after 1 h of second recovery of NiFe LDH<sup>OER</sup>//Pt/C<sup>HER</sup> electrolyzer in different KOH concentrations with and without 0.5 M NaCl (Fig. 8b); The current density at initial first recovery (that is after ~100 h of continuous electrolysis followed by ~10 min first break) is higher than the current density after ~100 h of electrolysis for the NiFe LDH<sup>OER</sup>//Pt/C<sup>HER</sup> electrolyzer in 0.1 M KOH, 0.5 M KOH, and 1 M KOH suggesting the good recovery effect of NiFe LDH<sup>OER</sup>//Pt/C<sup>HER</sup> electrolyzer in NaCl-free electrolyte; On the other hand, the current density at initial first recovery is higher than the current density after ~100 h of electrolysis for the NiFe LDH<sup>OER</sup>//Pt/C<sup>HER</sup> electrolyzer in 0.5 M KOH with 0.5 M NaCl, and 1 M KOH with 0.5 M NaCl, whereas the current density at initial first recovery is lower than the current density at 100 h for the NiFe LDH<sup>OER</sup>//Pt/C<sup>HER</sup> electrolyzer in 0.1 M KOH with 0.5 M NaCl, and those suggested that good recovery effect could be achieved for the NiFe LDH<sup>OER</sup>//Pt/C<sup>HER</sup> electrolyzer by using the electrolyte with the concentration of OH<sup>-</sup> equal to or greater than the concentration of Cl<sup>-</sup>, whereas poor recovery effect could be achieved for the NiFe LDH<sup>OER</sup>//Pt/C<sup>HER</sup> electrolyzer by using the concentration of OH<sup>-</sup> lesser than the concentration of Cl<sup>-</sup>; Besides, the current density at initial second recovery (that

is after ~100 h of continuous electrolysis followed by ~10 min first break followed by ~1 h electrolysis followed by ~1 h second break) is neither much higher nor much lower than the current density after 1st recovery followed by ~1 h of electrolysis for the NiFe LDH<sup>OER</sup>//Pt/C<sup>HER</sup> electrolyzer in 0.1 M KOH, 0.5 M KOH, 1 M KOH, 0.5 M KOH with 0.5 M NaCl, and 1 M KOH with 0.5 M NaCl, and those suggested that the second recovery effect is less pronounced than first recovery effect, which could be possibly due to the short electrolysis duration (that is 1st recovery followed by ~1 h of electrolysis) during the second recovery effect. Moreover, sustainable-renewable energy resources such as solar energy possesses non-continuous cycle life due to its diurnal cycle, which could hinder the continuous generation of energy, and therefore, they have recorded the chronoamperometric response of NiFe LDH<sup>OER</sup>//Pt/C<sup>HER</sup> electrolyzer in 0.5 M KOH with 0.5 M NaCl for about 5 days with 20 h of day time at 1.6 V followed by 4 h of night time at open-circuit potential; A clear recovery has been observed after each diurnal cycle suggesting a good recovery effect for NiFe LDH<sup>OER</sup>//Pt/C<sup>HER</sup> electrolyzer, while this intermittent stability test for ~5 days is almost resemble the ~100 h of continuous stability test, which suggest that NiFe LDH<sup>OER</sup>//Pt/C<sup>HER</sup> electrolyzer could possibly be used in photovoltaic solar systems having diurnal cycle. Moreover, they have conducted material characterization to identify the OER active sites of NiFe LDH anode; The Ni and Fe K-edge XANES spectra of NiFe LDH (Fig. 8c) shift to higher energy position at applied potential in both 0.1 M KOH and 0.1 M KOH with 0.5 M NaCl, which indicate the partial oxidation of Ni and Fe, respectively, where the oxidation state of Ni and Fe are higher at +1.6 V versus RHE than at +1.0 V versus RHE in 0.1 M KOH, whereas the oxidation state of Ni and Fe are almost similar at +1.6 V versus RHE and +1.0 V versus RHE in 0.1 M KOH with 0.5 M NaCl; This could be due to the voltammetric Ni reduction peak potential, which has been located more anodic of +1.0 V versus RHE suggesting the relatively slow Ni reduction kinetics; The EXAFS spectra (Fig. 8d) could disclose structure of LDH, which could be almost similar to the structure of hydroxalite, while almost similar EXAFS spectra had been obtained at both metal K edges; The Fe atoms could be incorporated inside the LDH without any distinct separate Fe oxide phase; A smaller M–O1 distance has been expected for the Fe–O1 shell than that of Ni–O1 shell (peak 1 in the FT) because of the +3 oxidation state of Fe; Accordingly, the Ni–O1 distance (2.04–2.05 Å) has been larger than the Fe–O1 distance (2.00–2.01 Å); As shown in Fig. 8d, peak number 2 in the FT EXAFS plot can be ascribed to the edge-sharing μ-oxo bridged metal atoms; Therefore, the double distance has been observed, which is labelled as peak 6, while the peak number 5 has emerged as a consequence of M–O6–octahedra linked through one joint edge, but sitting in different planes with respect to the linearly joined edge-sharing octahedral; Peak 3 and peak 4 are ascribed to the two more oxygen shells in the EXAFS spectra, whereas the amplitude has been small and the uncertainty of the coordination number is large; The EXAFS spectra of NiFe LDH in 0.1 M KOH and 0.1 M KOH with 0.5 M NaCl are almost similar, whereas the coordination numbers exhibit considerable difference for NiFe LDH in 0.1 M KOH with 0.5 M NaCl; The NiFe LDH in 0.1 M KOH with 0.5 M NaCl attained a stable state at +1.0 V versus RHE after 15 min operation, while the state has not obviously altered at +1.6 V versus RHE; Thus, the NiFe LDH anode in NaCl containing higher ionic strength electrolyte could catalyze the molecular oxidation, and that could cause higher oxidation states with corresponding higher coordination number.

Selection of suitable catalyst for OER is vitally important to achieve high stability for seawater electrolysis; The noble Pt based electrocatalyst is highly active for HER; However, the noble Pt/C electrocatalyst is less active for OER than that of earth-abundant electrocatalysts such as NiFe based electrocatalysts [91,92], while

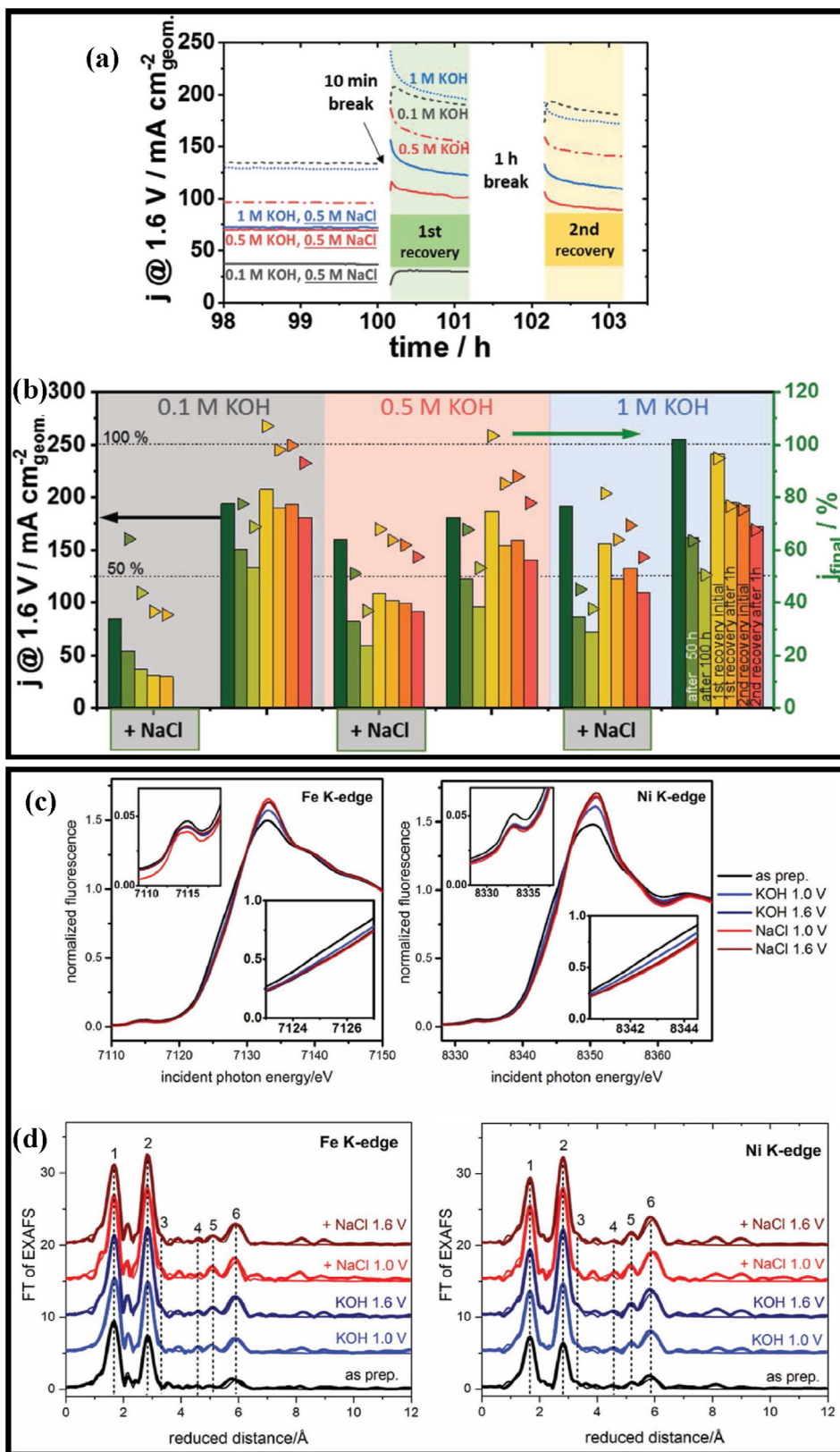


**Fig. 8.** (a) Chronoamperometric response of NiFe LDH<sup>ORR</sup>/Pt/C<sup>HER</sup> electrolyzer at 1.6 V for >100 h in different KOH concentrations with and without 0.5 M NaCl, where ~100 h of continuous electrolysis followed by ~10 min first break followed by ~1 h electrolysis followed by ~1 h second break followed by ~1 h electrolysis are performed to investigate the recovery effect of the electrolyzer; (b) The bar diagram provides the current density ( $j@1.6V$ ) of initial, while the bar diagram also provides the percentage relative to the maximum initial current density ( $j_{initial}$ ) of 50 h, 100 h, initial first recovery, after 1 h of first recovery, initial second recovery, and after 1 h of second recovery of NiFe LDH<sup>ORR</sup>/Pt/C<sup>HER</sup> electrolyzer in different KOH concentrations with and without 0.5 M NaCl; (c) XANES spectra at the Ni and the Fe K-edge of untreated NiFe LDH, NiFe LDH electrolysis at +1.0 V<sub>RHE</sub> in 0.1 M KOH, NiFe LDH electrolysis at +1.6 V<sub>RHE</sub> in 0.1 M KOH, NiFe LDH electrolysis at +1.0 V<sub>RHE</sub> in 0.1 M KOH with 0.5 M NaCl, and NiFe LDH electrolysis at +1.6 V<sub>RHE</sub> in 0.1 M KOH with 0.5 M NaCl; (d) EXAFS spectra at the Ni and the Fe K-edge of untreated NiFe LDH, NiFe LDH electrolysis at +1.0 V<sub>RHE</sub> in 0.1 M KOH, NiFe LDH electrolysis at +1.6 V<sub>RHE</sub> in 0.1 M KOH, NiFe LDH electrolysis at +1.0 V<sub>RHE</sub> in 0.1 M KOH with 0.5 M NaCl, and NiFe LDH electrolysis at +1.6 V<sub>RHE</sub> in 0.1 M KOH with 0.5 M NaCl, where quasi *in situ* freeze-quench approach is used (Reproduced with permission from Ref. [90]; Copyright 2018, Wiley-VCH Verlag GmbH & Co. KGaA, Weinheim).

morphology of the Pt electrocatalyst could significantly hamper its stability for HER possibly due to the poor gas evolution behavior such as high bubble adhesive force and slow release of gas bubbles during electrolysis [48]; Therefore, constructing electrolyzer with Pt/C as anode (OER) could hamper the stability for overall water splitting in sea water. Joshua M. Spurgeon's group [93] has observed that Pt/C<sup>OER</sup>//Pt/C<sup>HER(PEM)</sup> electrolyzer (PEM: Proton exchange membrane electrolyzer) exhibits much high activity, whereas it exhibits poor stability for overall water splitting in seawater electrolyte. For overall water splitting in seawater, Pt/C<sup>OER</sup>//Pt/C<sup>HER(PEM)</sup> electrolyzer exhibits much high activity (~1.51 V at 10 mA cm<sup>-2</sup>), whereas it exhibits poor stability (Obvious decay at 1.6 V for ~50 h).

Fabricating nanostructured NiFe LDH anode could modify the electronic structure, expose abundant active sites, enhance charge transfer process, and facilitate the gas evolution, and that could enhance the performance for OER; Therefore, constructing an electrolyzer with OER active NiFe LDH as anode and Pt/C as cathode could enhance the performance for overall water splitting in simulated seawater electrolyte. Thus, the NiFe LDH<sup>OER</sup>//Pt/C<sup>HER</sup> electrolyzer exhibits considerably much high activity and stability for overall water splitting in alkaline simulated seawater electrolyte [90]. Selection of suitable catalyst for OER is vitally important to achieve high stability for seawater electrolysis, while the morphology of the electrocatalyst could significantly hamper its stability possibly due to the poor gas evolution behavior. Thus, the Pt/C<sup>OER</sup>//Pt/C<sup>HER(PEM)</sup> electrolyzer (PEM: Proton exchange membrane electrolyzer) exhibits much high activity, whereas it exhibits poor stability for overall water splitting in seawater electrolyte [93].

## 5. Summary and outlook

Electrolysis of mostly abundant seawater is not only a promising approach to generate clean and ideal hydrogen energy, where it could also be an alternative for the grid-scale freshwater electrolysis, and that could eliminate the heavy strain on highly demanding fresh water. At first, the challenging issues for seawater electrolysis including competition of chlorine evolution reaction (CIER) with OER on the anode, need for the robust and efficient electrocatalysts to sustain against chloride corrosion, and the formation of precipitates on the electrode surface have been discussed in this review. Then, the recent advancement in terms of synthetic methodologies, chemical properties, DFT calculations, and catalytic performances of several nanostructured earth-abundant/precious-metal-containing electrocatalysts for HER and OER in seawater electrolyte have been provided in this review, where the discussion includes highly OER selective robust electrocatalysts such as transition metal hexacyanometallates based electrocatalyst, transition metal nitride, and LDH integrated with transition metal sulfide. Furthermore, the earth-abundant electrocatalysts including transition metal alloys, transition metal nitrides, transition metal oxides, transition metal doped metal oxides, transition metal phosphides, and transition metal integrated carbon nanotubes for HER in sea water have been discussed in this review (including  $\eta$  of  $\leq -200$  mV at  $-10$  mA cm<sup>-2</sup> for HER). Later, precious metal containing electrocatalysts including precious metal containing alloys, graphene supported precious metal containing alloy, precious metal based chalcogenide with cation vacancies, and heteroatom-doped carbon supported precious metal for HER in sea water have been reviewed. Furthermore, the earth-abundant electrocatalysts including transition metal alloys, transition metal based LDH, LDH integrated with transition metal sulfide, and transition metal nitride for OER in sea water have been discussed in this review (including  $\eta$  of  $\leq 300$  mV at  $\geq 100$  mA cm<sup>-2</sup> for OER). Moreover, the noble metal containing electrocatalysts

including noble metal containing alloys for OER in sea water have been reviewed. Then, the earth-abundant electrocatalysts including transition metal nitride/sulfide, transition metal oxides, LDH integrated with transition metal sulfide, and transition metal hexacyanometallates based electrocatalyst for overall water splitting in sea water have been discussed in this review (including high long term stability for  $\geq 600$  h for overall water splitting). Later, noble metal containing electrocatalysts for overall water splitting in sea water have been reviewed.

Even-though, it is still developing stage for the earth-abundant/precious-metal-containing electrocatalysts for seawater splitting to afford superior performance in practical applications, while the recent advancements in this area has also been very limited, and the essential factors governing the performance of earth-abundant/precious-metal-containing electrocatalysts for seawater splitting should be considered in future research:

1. Seawater splitting requires highly OER selective anode because CIER could compete with the OER, while electrocatalysts such as transition metal hexacyanometallates based electrocatalyst, transition metal nitride, and LDH integrated with transition metal sulfide could be used as highly OER selective electrocatalysts. However, highly OER selective electrocatalysts for seawater electrolysis are very limited. Hence, additional efforts are obviously needed by screening of electrocatalysts for highly OER selectivity using DFT calculations for seawater electrolysis.
2. Even-though, DFT calculations could be helpful to screen the electrocatalysts for highly OER selectivity, implementation of additional design strategies based on the reaction mechanism could be much helpful to achieve optimal OER performance especially for seawater electrolysis: Transition metal hexacyanometallates could be used as highly OER selective electrocatalysts, while achieving optimal OER performance could be hampered by their poor conductivity, and therefore, integrating conductive materials with transition metal hexacyanometallates could enhance their conductivity, and that could improve the OER performance. Therefore, in addition to the screening of electrocatalysts for highly OER selectivity using DFT calculations, implementation of additional design strategies could be much helpful to attain optimal OER performance especially for seawater electrolysis.
3. As seawater contains huge quantity of aggressive chloride anions, seawater electrolysis needs robust and efficient electrocatalysts to sustain against chloride corrosion, especially for the anode, while, strategies such as integration of transition metal hexacyanometallates with conductive materials, transition metal nitride with core-shell structure, and LDH as top layer with transition metal sulfide as underneath layer could afford robust stability for OER against chloride corrosion. However, electrocatalysts for OER with robust stability to sustain against chloride corrosion are very limited. Therefore, additional progresses are indeed necessary for fabricating the electrocatalysts for OER with robust stability by tailoring the morphologies, micro/nanostructures, compositions, and conductive matrices.
4. Fabricating of highly active electrocatalysts with robust stability especially from earth-abundant materials could significantly diminish the cost of the seawater electrolysis. NiFe based electrocatalysts could be considered as promising earth-abundant electrocatalysts especially for OER. Hence, additional efforts are obviously needed by synthesizing earth-abundant electrocatalysts with NiFe based components.
5. Fabrication of efficient electrocatalysts by integrating earth-abundant materials with noble materials could also diminish the cost by reducing the noble materials usage. Optimal catalytic performance could be achieved by integrating suitable earth-abundant materials with suitable noble materials: Alloy-

ing of Mo with Pt could enhance the HER performance for seawater electrolysis, while integration of conductive carbon with the electrocatalyst could further improve the performance. Therefore, additional progresses are obviously needed by fabricating efficient electrocatalysts by integrating suitable earth-abundant materials with suitable noble materials.

6. The formation of white insoluble precipitates such as  $Mg(OH)_2$  and  $Ca(OH)_2$  on the surface of the cathode/anode could be possible during electrolysis, which could partially diminish the activity possibly due to the blocking of some active sites. However, fabricating of electrocatalysts with robust stability could reduce the precipitate formation. Therefore, additional efforts are indeed necessary by fabricating electrocatalysts with robust stability to diminish the precipitate formation for seawater electrolysis.

### Credit Author Statement

**Jamesh Mohammed-Ibrahim:** Conceptualization, Data curation, Formal analysis, Investigation, Methodology, Project administration, Resources, Software, Validation, Visualization, Writing - original draft, and Writing - review & editing. **Harb Moussab:** Funding acquisition, and Supervision.

### Declaration of Competing Interest

The authors declare that they have no known competing financial interests or personal relationships that could have appeared to influence the work reported in this paper.

### Acknowledgement

This research was supported by the King Abdullah University of Science and Technology (KAUST).

### References

- [1] L. Yu, Q. Zhu, S. Song, B. McElhenny, D. Wang, C. Wu, Z. Qin, J. Bao, Y. Yu, S. Chen, Z. Ren, *Nat. Commun.* 10 (2019) 5106.
- [2] J. Luo, J.-H. Im, M.T. Mayer, M. Schreiber, M.K. Nazeeruddin, N.-G. Park, S.D. Tilley, H.J. Fan, M. Grätzel, *Science* 345 (2014) 1593–1596.
- [3] J.A. Turner, *Science* 305 (2004) 972–974.
- [4] M.I. Jamesh, M. Harb, *J. Energy Chem.* 56 (2021) 299–342.
- [5] M.-I. Jamesh, Y. Kuang, X. Sun, *ChemCatChem* 11 (2019) 1550–1575.
- [6] C.C.L. McCrory, S. Jung, I.M. Ferrer, S.M. Chatman, J.C. Peters, T.F. Jaramillo, *J. Am. Chem. Soc.* 137 (2015) 4347–4357.
- [7] M.I. Jamesh, *J. Power Sources* 333 (2016) 213–236.
- [8] M.-I. Jamesh, X. Sun, *J. Power Sources* 400 (2018) 31–68.
- [9] M.-I. Jamesh, X. Sun, *J. Energy Chem.* 34 (2019) 111–160.
- [10] M.I. Jamesh, *J. Power Sources* 448 (2020) 227375.
- [11] D. Zhou, P. Li, W. Xu, J. Sana, M.-I. Jamesh, W. Liu, Y. Kuang, X. Sun, *ChemNanoMat* (2020), <https://doi.org/10.1002/cnma.202000010>.
- [12] J. Qi, W. Zhang, R. Cao, *Adv. Energy Mater.* 8 (2018) 1701620.
- [13] X. Li, H. Lei, J. Liu, X. Zhao, S. Ding, Z. Zhang, X. Tao, W. Zhang, W. Wang, X. Zheng, R. Cao, *Angew. Chem. Int. Ed.* 57 (2018) 15070–15075.
- [14] Z. Gao, J. Qi, M. Chen, W. Zhang, R. Cao, *Electrochim. Acta* 224 (2017) 412–418.
- [15] Z. Liang, Z. Yang, J. Dang, J. Qi, H. Yuan, J. Gao, W. Zhang, H. Zheng, R. Cao, *Chem. -Eur. J.* 25 (2019) 621–626.
- [16] S. Shiva Kumar, V. Himabindu, *Mater. Sci. Energy Technol.* 2 (2019) 442–454.
- [17] T.A. Saleh, N.P. Shetti, M.M. Shanbhag, K. Raghava Reddy, T.M. Aminabhavi, *Mater. Sci. Energy Technol.* 3 (2020) 515–525.
- [18] J. Xie, X. Yang, Y. Xie, *Nanoscale* 12 (2020) 4283–4294.
- [19] J. Qi, J. Xie, Z. Wei, S. Lou, P. Hao, F. Lei, B. Tang, *Chem. Commun.* 56 (2020) 4575–4578.
- [20] J. Xie, Y. Guo, S. Lou, Z. Wei, P. Hao, F. Lei, B. Tang, *Chem. Commun.* 56 (2020) 4579–4582.
- [21] J. Xie, J. Qi, F. Lei, Y. Xie, *Chem. Commun.* (2020).
- [22] J. Xie, L. Gao, S. Cao, W. Liu, F. Lei, P. Hao, X. Xia, B. Tang, *J. Mater. Chem. A* 7 (2019) 13577–13584.
- [23] J. Xie, W. Liu, X. Zhang, Y. Guo, L. Gao, F. Lei, B. Tang, Y. Xie, *ACS Mater. Lett.* 1 (2019) 103–110.
- [24] J. Xie, S. Cao, L. Gao, F. Lei, P. Hao, B. Tang, *Chem. Commun.* 55 (2019) 9841–9844.
- [25] J. Bao, Z. Wang, J. Xie, L. Xu, F. Lei, M. Guan, Y. Zhao, Y. Huang, H. Li, *Chem. Commun.* 55 (2019) 3521–3524.
- [26] J. Xie, X. Zhang, Y. Xie, *ChemCatChem* 11 (2019) 4662–4670.
- [27] J. Xie, L. Gao, H. Jiang, X. Zhang, F. Lei, P. Hao, B. Tang, Y. Xie, *Cryst. Growth Des.* 19 (2019) 60–65.
- [28] J. Xie, J. Xin, R. Wang, X. Zhang, F. Lei, H. Qu, P. Hao, G. Cui, B. Tang, Y. Xie, *Nano Energy* 53 (2018) 74–82.
- [29] J. Xie, H. Qu, F. Lei, X. Peng, W. Liu, L. Gao, P. Hao, G. Cui, B. Tang, *J. Mater. Chem. A* 6 (2018) 16121–16129.
- [30] J. Xie, X. Zhang, H. Zhang, J. Zhang, S. Li, R. Wang, B. Pan, Y. Xie, *Adv. Mater.* 29 (2017) 1604765.
- [31] J. Xie, H. Qu, J. Xin, X. Zhang, G. Cui, X. Zhang, J. Bao, B. Tang, Y. Xie, *Nano Res.* 10 (2017) 1178–1188.
- [32] J. Xie, Y. Xie, *Chem. -Eur. J.* 22 (2016) 3588–3598.
- [33] J. Xie, Y. Xie, *ChemCatChem* 7 (2015) 2568–2580.
- [34] J. Xie, S. Li, X. Zhang, J. Zhang, R. Wang, H. Zhang, B. Pan, Y. Xie, *Chem. Sci.* 5 (2014) 4615–4620.
- [35] J. Xie, J. Zhang, S. Li, F. Grote, X. Zhang, H. Zhang, R. Wang, Y. Lei, B. Pan, Y. Xie, *J. Am. Chem. Soc.* 135 (2013) 17881–17888.
- [36] J. Xie, H. Zhang, S. Li, R. Wang, X. Sun, M. Zhou, J. Zhou, X.W. Lou, Y. Xie, *Adv. Mater.* 25 (2013) 5807–5813.
- [37] Y. Liu, X. Liang, L. Gu, Y. Zhang, G.-D. Li, X. Zou, J.-S. Chen, *Nat. Commun.* 9 (2018) 2609.
- [38] L. Yu, H. Zhou, J. Sun, F. Qin, F. Yu, J. Bao, Y. Yu, S. Chen, Z. Ren, *Energy Environ. Sci.* 10 (2017) 1820–1827.
- [39] X. Teng, J. Wang, L. Ji, Y. Lv, Z. Chen, *Nanoscale* 10 (2018) 9276–9285.
- [40] J. Shen, M. Wang, L. Zhao, P. Zhang, J. Jiang, J. Liu, *J. Power Sources* 389 (2018) 160–168.
- [41] H. Zhou, F. Yu, Q. Zhu, J. Sun, F. Qin, L. Yu, J. Bao, Y. Yu, S. Chen, Z. Ren, *Energy Environ. Sci.* 11 (2018) 2858–2864.
- [42] C. Xiao, Y. Li, X. Lu, C. Zhao, *Adv. Funct. Mater.* 26 (2016) 3515–3523.
- [43] J. Jiang, F. Sun, S. Zhou, W. Hu, H. Zhang, J. Dong, Z. Jiang, J. Zhao, J. Li, W. Yan, M. Wang, *Nat. Commun.* 9 (2018) 2885.
- [44] M. Tong, L. Wang, P. Yu, C. Tian, X. Liu, W. Zhou, H. Fu, *ACS Sustainable Chem. Eng.* 6 (2018) 2474–2481.
- [45] R. Zhang, X. Wang, S. Yu, T. Wen, X. Zhu, F. Yang, X. Sun, X. Wang, W. Hu, *Adv. Mater.* 29 (2017) 1605502.
- [46] J. Hou, Y. Sun, Y. Wu, S. Cao, L. Sun, *Adv. Funct. Mater.* 28 (2018) 1704447.
- [47] L. Wu, Z. Pu, Z. Tu, I.S. Amiinu, S. Liu, P. Wang, S. Mu, *Chem. Eng. J.* 327 (2017) 705–712.
- [48] Y. Li, H. Zhang, T. Xu, Z. Lu, X. Wu, P. Wan, X. Sun, L. Jiang, *Adv. Funct. Mater.* 25 (2015) 1737–1744.
- [49] J.K. Nørskov, T. Bligaard, J. Rossmeisl, C.H. Christensen, *Nat. Chem.* 1 (2009) 37.
- [50] M. Harb, J.-M. Basset, *J. Phys. Chem. C* 124 (2020) 2472–2480.
- [51] M. Harb, G. Jeantelot, J.-M. Basset, *J. Phys. Chem. C* 123 (2019) 28210–28218.
- [52] M. Harb, L. Cavallo, *ACS Omega* 3 (2018) 18117–18123.
- [53] M. Harb, L. Cavallo, *ACS Omega* 1 (2016) 1041–1048.
- [54] M. Harb, *J. Phys. Chem. C* 119 (2015) 4565–4572.
- [55] M. Harb, L. Cavallo, J.-M. Basset, *J. Phys. Chem. C* 118 (2014) 20784–20790.
- [56] G. Zhou, Z. Guo, Y. Shan, S. Wu, J. Zhang, K. Yan, L. Liu, P.K. Chu, X. Wu, *Nano Energy* 55 (2019) 42–48.
- [57] Q. Xiang, F. Li, W. Chen, Y. Ma, Y. Wu, X. Gu, Y. Qin, P. Tao, C. Song, W. Shang, H. Zhu, T. Deng, J. Wu, *ACS Energy Lett.* 3 (2018) 2357–2365.
- [58] D. Zhou, Z. Cai, Y. Bi, W. Tian, M. Luo, Q. Zhang, Q. Xie, J. Wang, Y. Li, Y. Kuang, X. Duan, M. Bajdich, S. Siahrostami, X. Sun, *Nano Res.* 11 (2018) 1358–1368.
- [59] A. Wu, Y. Xie, H. Ma, C. Tian, Y. Gu, H. Yan, X. Zhang, G. Yang, H. Fu, *Nano Energy* 44 (2018) 353–363.
- [60] Y. Gu, S. Chen, J. Ren, Y.A. Jia, C. Chen, S. Komarneni, D. Yang, X. Yao, *ACS Nano* 12 (2018) 245–253.
- [61] Y. Shen, Y. Zhou, D. Wang, X. Wu, J. Li, J. Xi, *Adv. Energy Mater.* 8 (2018) 1701759.
- [62] K. Qu, Y. Zheng, X. Zhang, K. Davey, S. Dai, S.Z. Qiao, *ACS Nano* 11 (2017) 7293–7300.
- [63] F. Dionigi, T. Reier, Z. Pawolek, M. Gliech, P. Strasser, *ChemSusChem* 9 (2016) 962–972.
- [64] S.-H. Hsu, J. Miao, L. Zhang, J. Gao, H. Wang, H. Tao, S.-F. Hung, A. Vasileff, S.Z. Qiao, B. Liu, *Adv. Mater.* 30 (2018) 1707261.
- [65] (CRC Handbook of Chemistry and Physics, 96th ed. (Ed.: D. R. Lide), CRC Press, New York, 2015).
- [66] Y. Kuang, L.J. Kenney, Y. Meng, W.-H. Hung, Y. Liu, J.E. Huang, R. Prasanna, P. Li, Y. Li, L. Wang, M.-C. Lin, M.D. McGehee, X. Sun, H. Dai, *Proc. Natl. Acad. Sci.* 116 (2019) 6624–6629.
- [67] X. Lu, J. Pan, E. Lovell, T.H. Tan, Y.H. Ng, R. Amal, *Energy Environ. Sci.* 11 (2018) 1898–1910.
- [68] Q. Lv, J. Han, X. Tan, W. Wang, L. Cao, B. Dong, *ACS Appl. Energy Mater.* 2 (2019) 3910–3917.
- [69] F. Cheng, X. Feng, X. Chen, W. Lin, J. Rong, W. Yang, *Electrochim. Acta* 251 (2017) 336–343.
- [70] Y. Huang, L. Hu, R. Liu, Y. Hu, T. Xiong, W. Qiu, M.S. Balogun, A. Pan, Y. Tong, *Appl. Catal. B* 251 (2019) 181–194.
- [71] M. Sarno, E. Ponticorvo, D. Scarpa, *Electrochem. Commun.* 111 (2020) 106647.
- [72] M. Jamesh, T.S.N. Sankara Narayanan, P.K. Chu, *Mater. Chem. Phys.* 138 (2013) 565–572.
- [73] M.I. Jamesh, P. Li, M.M.M. Bilek, R.L. Boxman, D.R. McKenzie, P.K. Chu, *Corros. Sci.* 97 (2015) 126–138.
- [74] M.I. Jamesh, G. Wu, Y. Zhao, D.R. McKenzie, M.M.M. Bilek, P.K. Chu, *Corros. Sci.* 91 (2015) 160–184.

- [75] M. Jamesh, S. Kumar, T.S.N. Sankara Narayanan, *Corros. Sci.* 53 (2011) 645–654.
- [76] X. Huang, S. Chang, W.S.V. Lee, J. Ding, J.M. Xue, *J. Mater. Chem. A* 5 (2017) 18176–18182.
- [77] H. Jin, X. Liu, A. Vasileff, Y. Jiao, Y. Zhao, Y. Zheng, S.-Z. Qiao, *ACS Nano* 12 (2018) 12761–12769.
- [78] J. Zheng, Y. Zhao, H. Xi, C. Li, *RSC Adv.* 8 (2018) 9423–9429.
- [79] H. Li, Q. Tang, B. He, P. Yang, *J. Mater. Chem. A* 4 (2016) 6513–6520.
- [80] Y. Zhang, P. Li, X. Yang, W. Fa, S. Ge, *J. Alloy. Compd.* 732 (2018) 248–256.
- [81] M. Gong, W. Zhou, M.J. Kenney, R. Kapusta, S. Cowley, Y. Wu, B. Lu, M.-C. Lin, D.-Y. Wang, J. Yang, B.-J. Hwang, H. Dai, *Angew. Chem.* 127 (2015) 12157–12161.
- [82] S. Gao, G.-D. Li, Y. Liu, H. Chen, L.-L. Feng, Y. Wang, M. Yang, D. Wang, S. Wang, X. Zou, *Nanoscale* 7 (2015) 2306–2316.
- [83] J. Zheng, *Appl. Surf. Sci.* 413 (2017) 72–82.
- [84] J. Zheng, *Appl. Surf. Sci.* 413 (2017) 360–365.
- [85] X. Niu, Q. Tang, B. He, P. Yang, *Electrochim. Acta* 208 (2016) 180–187.
- [86] Y. Liu, X. Hu, B. Huang, Z. Xie, *ACS Sustainable Chem. Eng.* 7 (2019) 18835–18843.
- [87] J. Zheng, *Electrochim. Acta* 247 (2017) 381–391.
- [88] X. Gao, Y. Chen, T. Sun, J. Huang, W. Zhang, Q. Wang, R. Cao, *Energy Environ. Sci.* 13 (2020) 174–182.
- [89] Y. Zhao, B. Jin, A. Vasileff, Y. Jiao, S.-Z. Qiao, *J. Mater. Chem. A* 7 (2019) 8117–8121.
- [90] S. Dresch, F. Dionigi, S. Loos, J. Ferreira de Araujo, C. Spöri, M. Gliech, H. Dau, P. Strasser, *Adv. Energy Mater.* 8 (2018) 1800338.
- [91] Z. Daojin, C. Zhao, L. Xiaodong, T. Weiliang, B. Yongmin, J. Yin, H. Nana, G. Tengfei, Z. Qian, K. Yun, P. Junqing, S. Xiaoming, D. Xue, *Adv. Energy Mater.* 8 (2018) 1701905.
- [92] L. Qian, Z. Lu, T. Xu, X. Wu, Y. Tian, Y. Li, Z. Huo, X. Sun, X. Duan, *Adv. Energy Mater.* 5 (2015) 1500245.
- [93] S. Kumari, R. Turner White, B. Kumar, J.M. Spurgeon, *Energy Environ. Sci.* 9 (2016) 1725–1733.